On the Development of Compact Electronic Neutron and Gamma Sources

By Allan Xi Chen

A dissertation submitted in partial satisfaction of the

requirements for the degree of

Doctor of Philosophy

in

Engineering — Mechanical Engineering

in the

Graduate Division

of the

University of California, Berkeley

Committee in charge:

Professor Ralph Greif, Co-Chair

Professor Samuel S. Mao, Co-Chair

Professor Chris Dames

Professor Ka-Ngo Leung

Fall 2013

On the Development of Compact Electronic Neutron and Gamma Sources

Abstract

On the Development of Compact Electronic Gamma and Neutron Sources

by

Allan Xi Chen

Doctor of Philosophy in Engineering —

Mechanical Engineering

University of California, Berkeley

Professor Ralph Greif, Co-Chair

Professor Samuel S. Mao, Co-Chair

The development of compact electronic gamma and neutron sources utilizing several deuteron-induced nuclear reactions on low-Z compounds are presented in this study. These systems feature a compact high current density RF inductive discharge plasma source to provide the ion current necessary for a high yield gamma or neutron source. The first part of this project studied an electronic gamma source that utilized low-energy (d,nγ) nuclear reactions to generate mono-energetic gamma rays (0.5 to 1.5 MeV) having energies similar to existing radiological sources used in the field (e.g. ^{60}Co, ^{137}Cs, ^{192}Ir). The source incorporates a novel compact pyroelectric crystal powering system that produces the high voltage needed by thermal cycling the crystal in the room temperature range. Experiments were carried out and an analysis was performed to determine the gamma source performance requirements to provide equivalent or improved functionality for the user community, while being less susceptible to malevolent use.

The second part of this project studied the next generation of compact high flux electronic neutron generators that utilized the deuteron-deuteron (D-D) reaction to produce 2.45 MeV neutrons. The maximum flux level for a 120 keV – 1 ampere D^+ beam bombarding titanium is expected to approach 10^{11} n cm^{-2} s^{-1}, which is close to the levels available in research reactors and large accelerator facilities. Analysis and experiments with the neutron generators show promise for utilization in traditional applications that require reactor neutrons such as the ^{39}Ar/^{40}Ar geochronology dating technique and boron-neutron-capture therapy (BNCT).

Acknowledgements

I would like to thank Dr. Arlyn Antolak and Professor Ka-Ngo Leung for giving me the opportunity to come to Sandia National Laboratories to develop and conduct research on the gamma source. It was a great experience for me and I'm thankful for their advice throughout the years. I want to also thank the technical team, Thomas Raber, Dan Morse, and Ken Stewart for their technical help throughout the project. I want to thank my managers at Sandia, Dr. John Goldsmith, Dr. Alf Morales, Dr. Craig Tewell, and Dr. Jim Lund. I want to thank other staff at Sandia, Dr. Bernice Mills, Toff Garcia, Albert Sandoval, Dr. Kristin Hertz, Dr. Don Cowgill, Dr. Sudeep Mitra, Aaron Nowack, John Walter, for their advice and expertise. Finally, I would also like to thank the secretarial staff, Jacqueline Reardon, Jennifer Bamberger, and Kristi Duenas for administrative help in making my day better at Sandia.

I want to thank Professor Paul Renne and Professor Ka-Ngo Leung for giving me the opportunity to develop the high flux neutron generator (HFNG) at UC Berkeley. It was a really good experience for me and I thank him and his team for their help and advice. In particular, I would like to thank Tim Becker and William Cassata for their helpful discussion of the HFNG. I especially want to thank Glenn Jones for his continued contribution to the design and fabrication of major components for the HFNG as well as technical help and advice for mechanical design in general. I also want to thank Andrew Rogers for his great help in managing the project and Karl van Bibber of the nuclear engineering department for his effort in getting the lab space available to install the HFNG. I want to thank the graduate students Cory Waltz, Leo Kirsch, Austin Lo, and Madicken Munk for their continuing work on getting the HFNG up and running. Lastly, I want to thank Dr. Lee Bernstein, Dr. Richard Firestone, and Dr. Jay James for their continued support an interest in the HFNG.

Finally, I want to thank Professor Ralph Greif, Professor Samuel Mao, and Professor Chris Dames for serving in my dissertation committee. In addition, I want to thank Professor Costas Grigoropoulos and Professor Jasmina Vujic for serving in my qualifying examination committee. I want to thank my family for all of their love and support throughout the course of my life. Thank you.

To my entire family and friends

Table of Contents

List of Figures v

List of Tables ix

1. INTRODUCTION 1

I. Radiological Gamma Source Replacement 1
II. Reactor Neutron Source Replacement 3

2. ACCELERATOR DRIVEN NUCLEAR REACTIONS 5

I. Gamma Producing Reactions 5
II. Neutron Producing Reactions 10
III. Neutron to Gamma Converter 13

3. RF DRIVEN EXTERNAL ANTENNA PLASMA ION SOURCE 15

I. Modes of Operation 15
II. E x B Mass Filter 20
III. d-^{6}Li Beam Loaded Target 21

4. COMPACT PYROELECTRIC DRIVEN ACCELERATOR 22

I. Pyroelectric effect 23
II. Material properties 24
III. Pyroelectric crystal accelerator design 27
IV. Pulsing techniques to achieve high gamma flux 37

5. HIGH-FLUX NEUTRON GENERATOR 45

I. Applications 45
I. Neutron Flux Profile 46
II. Thermal Analysis of the Beam Loaded Target 48
III. Neutron Moderator 53
IV. Radiological Material Activation 59
V. Neutron Source Calibration 60

6. APPLICATIONS OF ELECTRONIC NEUTRON SOURCES FOR OIL WELL-LOGGING 62

I. Compensated Neutron Porosity Well-Logging (CNL) 62
II. Computational Model 63
III. Simulation Results [65] 65
IV. Neutron Detector Technologies for Nuclear Logging Tools 66

7. CONCLUSION 68

8. FUTURE WORK 70

9. REFERENCES 71

10. APPENDIX 77

List of Figures

Figure 1.1: (Top) Gamma Sources Spectrum (a) Co-60 Gamma Knife (b) Cs-137 Well Logging Source (c) Ir-192 Radiography Source. 2

Figure 1.2: OSU Triga Mark III Research Reactor [5] 3

Figure 1.3: Aeriel view of the SNS at ORNL (left). Schematic layout of the SNS facility (right). 4

Figure 2.1: The Clinac iX Linear accelerator produces bremsstrahlung gammas for cancer treatment. 5

Figure 2.2: Total cross sections for 6Li(d,γ)7Be and 9Be(d,γ)10B [15] 6

Figure 2.3: Stopping power of Various Li and Be compounds. All Li compounds contain 95% enriched Li-6 except for LiTaO3, which contains natural abundance Li. 7

Figure 2.4: Gamma yield per coulomb of incident deuteron ion charge as a function of beam energy. 8

Figure 2.5: a) Photo of Sandia particle accelerator and b) schematic of accelerator experimental arrangement. 9

Figure 2.6: Measured gamma spectrum for various beam energies from 200 keV to 400 keV. 9

Figure 2.7: Neutron production cross-section for D-D, D-T, and T-T reactions. 10

Figure 2.8: Stopping power as a function of energy for D-D, D-T, and T-T reaction in titanium. 11

Figure 2.9: Neutron yields for the D-D, D-T, T-T reactions per Coulomb of incident deuteron charge as a function of energy. 12

Figure 2.10: Neutron spectrum for the different neutron sources. 12

Figure 2.11: The transmission faction of gammas and neutrons through various thicknesses of polyethylene (P) and borated polyethylene (BP) material. 13

Figure 2.12: Schematic for the neutron converter experiment. 14

Figure 2.13: Gamma spectrums of measurements with neutron shielding and without neutron shielding. 14

Figure 3.1: (a) Schematic of the RF ion source with an integrated Wien filter. (b) Ion source mounted onto the vacuum chamber. (c) Inductively coupled RF source operating with multi-cusp field lines visible. 16

Figure 3.2: RF plasma discharge in capacitive mode (left). Inductive mode (right). 16

Figure 3.3: Measurement of the ion current as a function of the extraction voltage and RF power..... 17

Figure 3.4: Ion source schematic 18

Figure 3.5: Mass spectrometer measurements of the hydrogen ion beam species. 19

Figure 3.6: Calculated deflections for 1 kV extraction of D+ (left) and D- (right) using the E x B filter..... 20

Figure 3.7: Mass spectrometer measurement of the hydrogen and lithium species. 21

Figure 4.1: a) Commercially available x-ray source based on accelerating electrons to ~35 kV with a pyroelectric crystal. b) Prototype neutron source based on accelerating deuterium ions to ~90 kV with a pyroelectric crystal..... 22

Figure 4.2: LiTaO3 resistivity and pyroelectric coefficient as a function of temperature..... 25

Figure 4.3: 3D schematic showing the main components of the pyroelectric gamma source. 27

Figure 4.4: a) Schematic showing the design of the dielectric fluid immersion-type accelerator. b) FEM analysis of the electric potential for the dielectric fluid immersion-type accelerator. 29

Figure 4.5: Schematic of the heating/cooling system for the dielectric fluid immersion-type accelerator. 30

Figure 4.6: Crystal voltage as a function of temperature for different ion beam currents..... 32

Figure 4.7: Inlet fluid temperature as a function of time. Blue and green curves represent different experimental runs. 33

Figure 4.8: Electron energy spectrum measured using a silicon surface barrier detector for two different heating cycles. 33

Figure 4.9: Computed voltage as a function of temperature..... 34

Figure 4.10: a) Photo of a high voltage heating/cooling module. b) Crystal heating rate as a function of time. 35

Figure 4.11: Schematic showing the main components of the high voltage heating/cooling module..... 35

Figure 4.12: a) LiTaO3 crystal with copper conductive plate attached to one end. b) High voltage electrical breakdown along surface of crystal. 36

Figure 4.13: Measured X-ray energy spectrum from a single 3 cm diameter x 3 cm long LiTaO3 pyroelectric crystal that was cooled from ~20C to 0C. 37

Figure 4.14: Photos of a stacked high voltage acceleration system. The 28 mm arc distance indicates a stacked voltage of > 60 kV is achieved by the four modules. 38

Figure 4.15: Schematic showing a stacked pyroelectric crystal accelerator using quartz lamp heating. 39

Figure 4.16: Photo of the stacked quartz lamp heated pyroelectric crystal accelerator. 39

Figure 4.17: Temperature at the base of the crystal as a function of time. Numbers 1-4 represents crystals from left to right. 40

Figure 4.18: Schematic of the mechanical shutter system combined with an RF plasma ion source. 41

Figure 4.19: Photos showing the mechanical shutter hardware. 43

Figure 4.20: a) Analytical solution of the beam profile for the current geometry of extraction and ion source apertures. b) Oscilloscope trace of the beam profile measured with a Faraday cup during the operation of the shutter. 44

Figure 5.1: Inductive plasma discharge from the BGC-HFNG 45

Figure 5.2: Section views of the BGC-HFNG target modeled with MCNP5 (left). Actual target (right). 47

Figure 5.3: Neutron flux distribution of the BGC-HFNG in the sample slot area is shown on the left. Line out plots of the x-axis (blue) and y-axis (black) are shown on the right. 48

Figure 5.4: Nucleate Boiling superheat as a function of pressure and heat flux. Dashed line indicates heat flux of 1300 W/cm^2 51

Figure 5.5: Minimum operating parameters for different power levels. 52

Figure 5.6: Target surface temperature as a function of pressure. 52

Figure 5.7: Thermal neutron moderator geometry used in MCNP model. 54

Figure 5.8: Neutron flux computational results from MCNP. 55

Figure 5.9: BNCT moderator design for a previous HFNG 56

Figure 5.10: Epithermal neutron moderator design for an axial-type D-D HFNG. 57

Figure 5.11: Neutron energy spectrum at the treatment window. (left) current results, (right) previous results. 58

Figure 5.12: Calibration experiments using gold foil and nickel activation to determine absolute yield of the HFNG. 60

Figure 5.13: Gold activation calibration using D2O moderator. Gold foil is attached to the back of the moderator. 61

Figure 6.1: Compensated porosity neutron logging tool. 62

Figure 6.2: Magnified section of the CNL tool and borehole model used in MCNP. [65] 64

Figure 6.3: MCNP results of sandstone and limestone formations using different neutron sources with 108 particle histories used in all cases. 65

List of Tables

Table 1.1: Radiological Source Specifications. 1

Table 4.1: Electronic and thermal properties of LiTaO3. 25

Table 4.2: Electrical Characteristics of Tested Pyroelectric Crystals (red) our results, (black) other results. HPGe refers to high-purity germanium detector and PIPS(Si) refers to passivated implanted planar (silicon) detector. 37

Table 4.3: Summary of the acceleration chamber pressure measurements for the "beam-on" and "beam-off" shutter positions for a 1-mm diameter ion source aperture. 44

Table 5.1: Moderating power and moderating ratio of common low-Z neutron moderator materials 54

Table 5.2: Measured neutron count rates from light and heavy water moderators using a 32 mCi AmBe isotropic neutron source. Units are in counts per second measured by the MCA. 55

Table 5.3: MCNP5 results of the new epithermal moderator design. 58

Table 5.4: List of accountable radionuclides in accordance with the IAEA Basic Safety Standards 59

1. Introduction

I. Radiological Gamma Source Replacement

After more than a century since the discovery of gamma rays and eighty years after the discovery of the neutron, these particles provide a vital tool in a wide range of applications across many different industries. Due to their high penetrability compared to the lower energy x-ray radiation, gamma rays and neutrons are used in a broad range of applications for oil exploration, tumor treatment, geochronology and radiography. In many industrial applications (e.g. oil-well logging), gamma yields on the order of 1E10 γ/s and neutron yields > 1E7 n/s are desired to produce enough signal over a reasonable amount of time [1] [2]. This requirement can be easily satisfied with small gamma and neutron emitting radioactive sources such as ^{60}Co, ^{137}Cs, ^{192}Ir, and Am-Be [2]. The first three are mono-energetic gamma sources that emit photons in the range of 0.3 – 1.3 MeV (Figure 1.1) and the last is a neutron source emitting with a broad energy spectrum from 0 to 10MeV. Due to their high activity, a very small amount of the radioactive isotope is enough to generate Curie level yields (Table 1.1).

Table 1.1: Radiological Source Specifications.

Source	Specific Activity [Ci/g]	Half-life [years]	Average Gamma Energy [MeV]	Average Neutron Energy [MeV]
Co-60	4.18E+13	5.27	1.25	--
Cs-137	3.20E+12	30.2	0.662	--
Ir-192	3.41E+14	0.2	0.37	--
Am-Be	6.85E+06	432.7	--	4

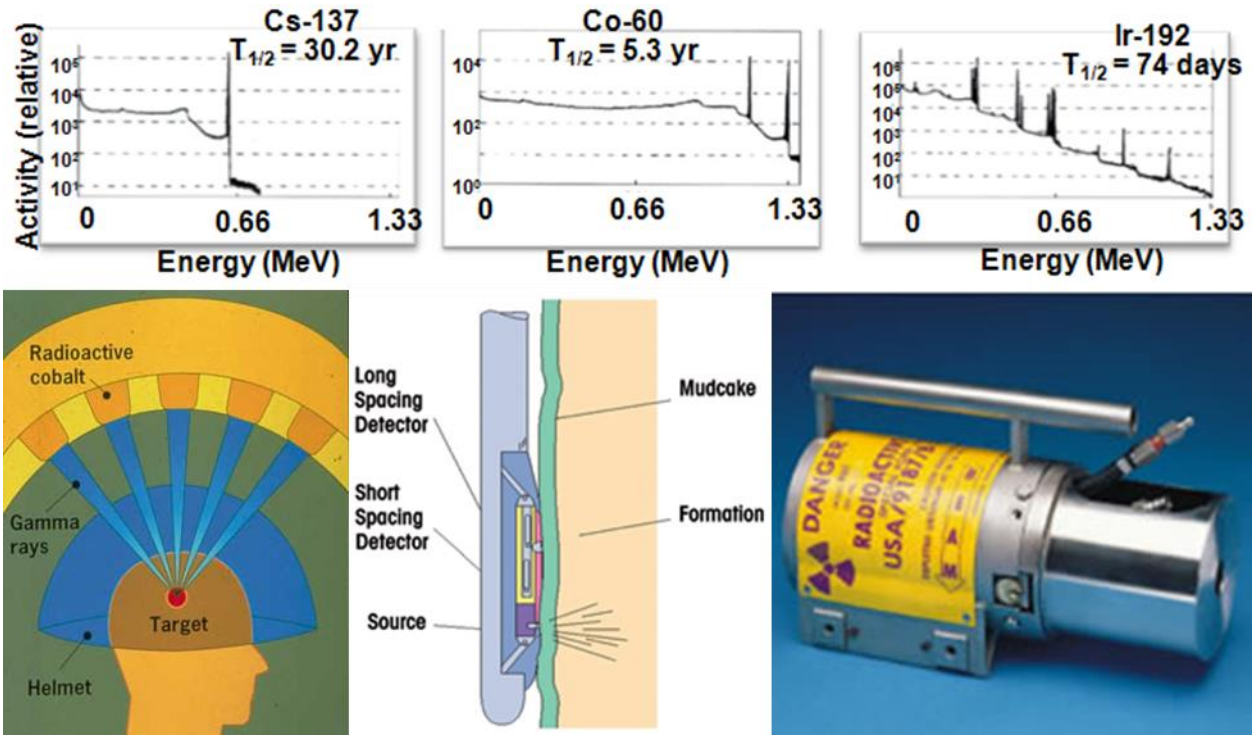

Figure 1.1: (Top) Gamma Sources Spectrum (a) Co-60 Gamma Knife (b) Cs-137 Well Logging Source (c) Ir-192 Radiography Source.

Until the last decade, there has been a lack of motivation in the user community to develop possible replacements for radiological sources. However, in the aftermath of the September 11, 2011 attacks, concerns over national security and nuclear proliferation both domestically and internationally has fueled renewed interest in research and development for a safer alternative to using radioactive materials. In 2006, the National Research Council [3] identified the sources in table 1 as "high-risk" targets for use in unconventional weapons due to their relatively long half-life, prevalence across industries, and ease of acquisition. At the conclusion of the report, they made the following two important recommendations regarding replacement source technologies:

> *"…the U.S. government should adopt policies that provide incentives (market, regulatory, or certification) to facilitate the introduction of replacements and reduce the attractiveness and availability of high-risk radionuclide sources."*

However, they have also warned that "replacement of some radionuclide radiation sources with alternatives should be implemented with caution, ensuring that the essential functions that the radionuclide radiation sources perform are preserved." Following these two recommendations of the report, development of alternative replacement technologies for both gamma- and neutron-emitting sources were explored; experiments were also performed to evaluate and analyze their functions in several important applications.

II. Reactor Neutron Source Replacement

For applications that use neutron sources, the range of neutron fluxes required varies greatly depending on the application. In oil well logging and associated particle imaging applications, a source emitting 10^7 n/s of fast neutrons is sufficient. On the other hand, geochronology applications demand neutron fluxes that are greater than 10^{10} n/cm^2/s of total neutron flux to complete the experiments in a reasonable time scale [4]. Traditionally, the highest flux of neutrons can only be found inside a nuclear reactor [5]. As a result, applications that require very high neutron fluxes (>1E11 n/cm^2) such as neutron radiography, geochronology, and tumor treatment can only be accomplished using reactor neutrons.

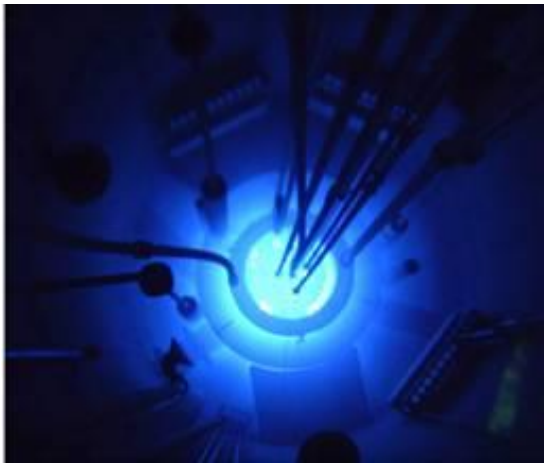

Figure 1.2: OSU Triga Mark III Research Reactor [5]

In the last few decades, there has been a general anti-nuclear sentiment in the U.S. as a result of several alarming incidents involving the operation of nuclear reactors, such as the Three Mile Island accident in 1979 [6], Chernobyl disaster in 1986 [7], and the Fukushima Daiichi disaster in 2011 [8]. Germany, in wake of the Fukushima incident, had announced plans to shut down all nuclear reactors by 2022 [9]. Aside from direct economic setback to the nuclear power industry itself, the general anti-nuclear sentiment also has the ricocheting effect on users that require reactor neutrons because they must begin to find alternative replacements.

Just as there are several accelerator-type methods to produce gammas, high neutron yields can also be produced by accelerators. Currently, the highest yield neutron sources produced in an accelerator facility uses the process known as spallation, where proton beams are accelerated to ~1 GeV energies and bombard a high-Z material to produce neutrons [10]. The Spallation Neutron Source (Figure 1.3) operating in Oak Ridge National Laboratories is the highest yield spallation neutron source in world, producing > 1E16 n/s in a short pulse [11]. Despite the high neutron yields that can be achieved with these facilities, there are several drawbacks that should be considered: (1) the size and infrastructure required by these facilities are on the same order of magnitude as a typical nuclear reactor; (2) the neutron energies produced spans the range from 0 up to 1 GeV. In many applications, neutron energies under 3 MeV are required. For

geochronology, neutron energies above 3 MeV produce undesirable reactions that could jeopardize the quality of the experiment [4]. For tumor treatment using boron-neutron-capture-therapy (BNCT), only neutrons in the range of 0.4 – 20 keV are desired, all other energy neutrons will contribute to unwanted radiation dose to the patient [12] [13]. Therefore, it is more appropriate to provide neutrons with energies as close to the requirement as possible.

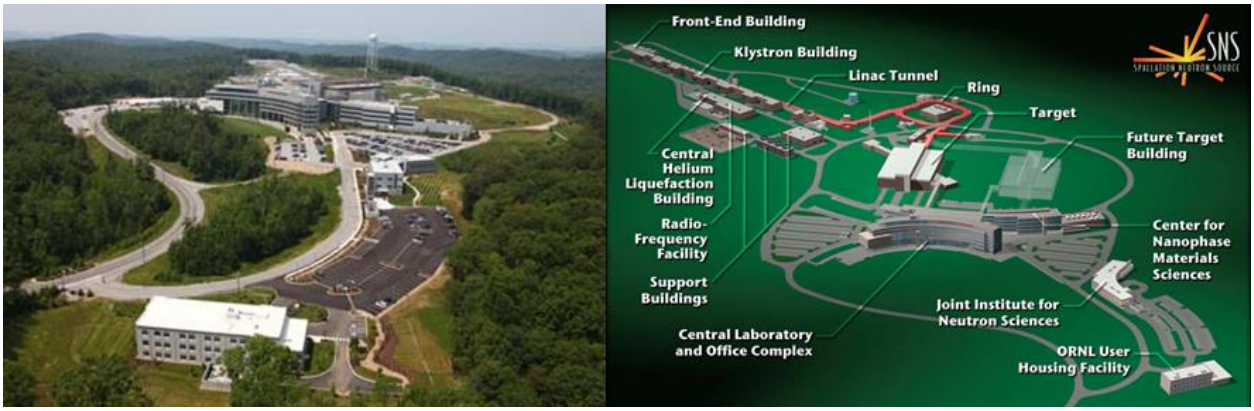

Figure 1.3: Aeriel view of the SNS at ORNL (left). Schematic layout of the SNS facility (right).

2. Accelerator Driven Nuclear Reactions

I. Gamma Producing Reactions

As a possible candidate for replacing radiological gamma sources, one could use an electron linear accelerator (linac) to produce bremsstrahlung radiation having energies up to the maximum (endpoint) energy of the accelerated electrons (Figure 2.1) [14]. Linacs operating at several megavolts are commercially available, but their size and power requirements often render them impractical for many applications. The gammas produced by linacs are not mono-energetic and the average energy of the generated bremsstrahlung spectrum occurs at approximately 1/3 of the endpoint energy. As a result, to achieve ~1 MeV energy gamma-rays (characteristic of radiological sources), a linac needs to operate with at least 3 MeV endpoint energy.

Figure 2.1: The Clinac iX Linear accelerator produces bremsstrahlung gammas for cancer treatment.

An alternative way to produce high-energy mono-energetic gammas is by using nuclear reactions. To replace ^{60}Co, ^{137}Cs, or ^{192}Ir radiological sources, gamma energies in the range of 0.4 to 1.4 MeV are of interest and we have identified that both ^{6}Li(d,n)^{7}Be and ^{9}Be(d,n)^{10}B reactions can produce gammas in this energy range [15]. The d-^{6}Li reaction produces two gamma rays at 430 and 478 keV with approximately equal probability due to the mirror reactions between ^{6}Li(d,n)^{7}Be and ^{6}Li(d,p)^{7}Li [16]. Thus, in most applications of interest the bimodal gamma emissions should be treated as a single energy emission with twice the yield. The ^{9}Be(d,nγ)^{10}B reaction produces five gamma-rays at 410 keV, 718 keV, 1.03 MeV, 1.44 MeV, and 2.87 MeV with the 718 keV gammas having the highest production cross section [15] [17]. There are two main advantages in using nuclear reaction induced gammas for radiological source replacement: (1) the gamma rays produced are mono-energetic and their energies match very closely to the radioactive gamma sources and (2) the required reaction energy can be low for producing high intensity radiation and allowing a more compact acceleration system to be used.

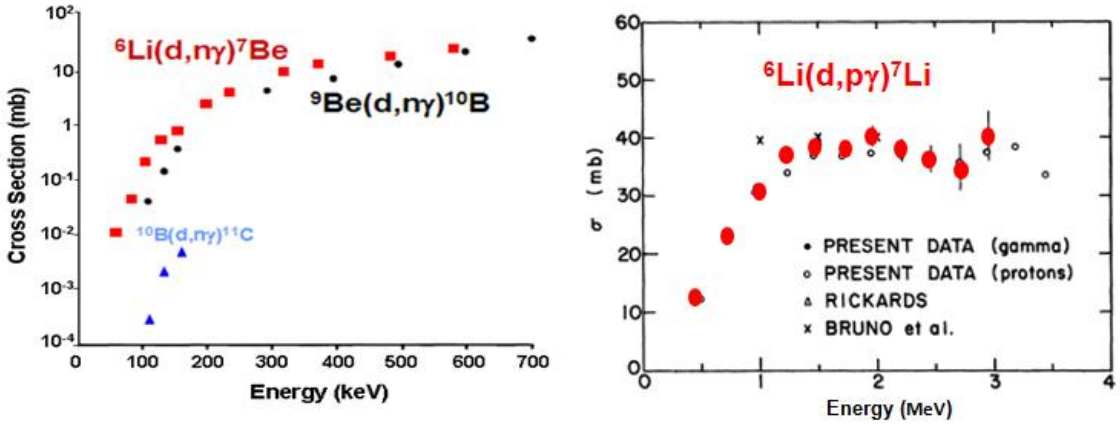

Figure 2.2: Total cross sections for 6Li(d,γ)7Be and 9Be(d,γ)10B [15]

The thick target yield for these two reactions was previously measured using a particle accelerator. The ^{6}Li(d,n)^{7}Be reaction cross-section was measured using a deuterium ion beam to bombard on 99.3% enriched ^{6}LiF; similarly, the ^{9}Be(d,n)^{10}B cross-section was measured for deuterium on BeO [15]. Using the published reaction cross-sections (Figure 2.2), one can calculate the gamma yield of deuterons on other lithium or beryllium compounds using a generalized yield function:

$$Y(E_{max}) = \frac{N_A \rho}{eM} \beta \sum_{n=1}^{3} f_n \int_0^{E_{max}/n} \frac{\sigma(E)}{(dE/dx)_n} dE \tag{1.1}$$

$$\left(\frac{dE}{dx}\right)_n = \left(\frac{dE}{dx}\right)_{n,electronic} + \left(\frac{dE}{dx}\right)_{n,nuclear} \tag{1.2}$$

where N_A is Avogadro's constant, e is the electronic charge, M is the molar mass of the target compound, ρ is the target material density, β is the stoichiometric fraction of ^{6}Li or Be in the compound, σ(E) is the energy dependent total cross-section, E_{max} is the incident deuteron energy which is equivalent to the acceleration potential, dE/dx is the total stopping power of deuterons in the target compound, and f_n is the fraction of deuteron ion species. The electronic and nuclear stopping powers of deuterons in the target materials have been calculated using the ion transport code SRIM for deuteron bombardment on the target compounds of interest (Figure 2.3) [18]. From the calculations, we found that the nuclear stopping power contribution was significantly smaller than the electronic contribution and the results become especially prominent at high incident deuteron energies. This can be explained by considering the primary mechanism of interaction between the incident deuteron and the nucleus, which is simply Coulomb repulsion. At high incident energies, the deuteron has less time to interact with the nucleus amid the sea of electrons. Therefore, the total stopping power can be approximated by the electronic stopping power alone:

$$\left(\frac{dE}{dx}\right)_n \approx \left(\frac{dE}{dx}\right)_{n,electronic} \tag{1.3}$$

For a purely monoatomic deuteron beam (Eq. 2.1), the components n=2 and n=3 are neglected because $f_{n\neq1} = 0$. For molecular ions bombarding a solid target ($f_2, f_3 \neq 0$), the maximum energy is 1/k times E_{max} of the monoatomic case where k is the number of nucleons in the molecular ion. Therefore, D_2^+ and D_3^+ ions can only react at 1/2 and 1/3 of the acceleration potential. This will dramatically reduce the gamma yield due to the lower reaction energy.

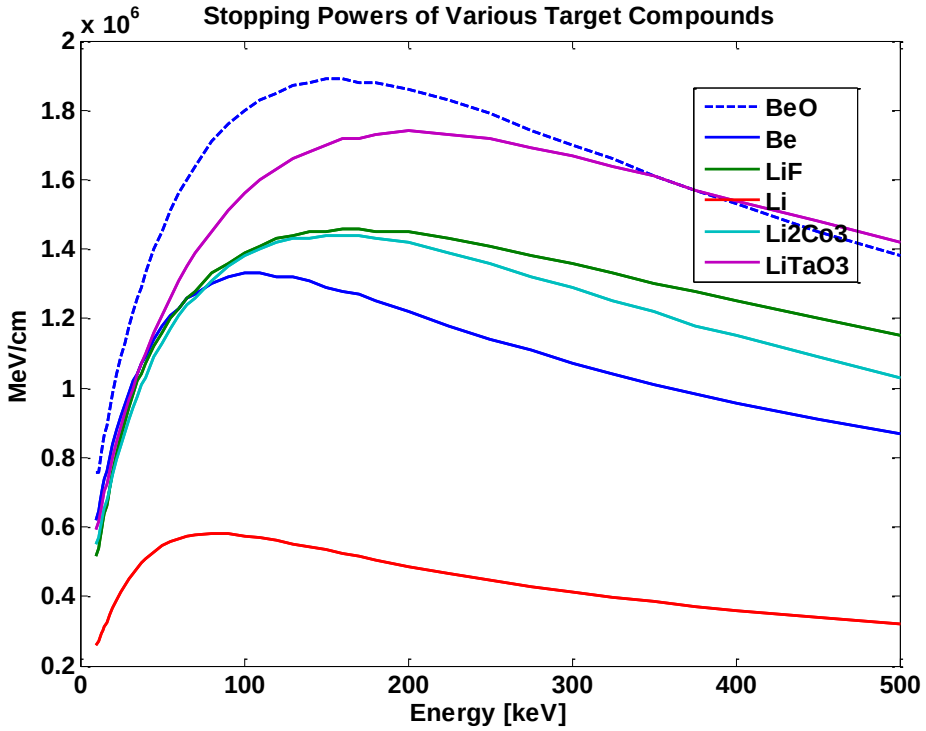

Figure 2.3: Stopping power of Various Li and Be compounds. All Li compounds contain 95% enriched Li-6 except for LiTaO3, which contains natural abundance Li.

Figure 2.4 shows a plot of the yield (gammas/second) per ampere of deuteron beam current as a function of the deuteron beam energy from 100 keV up to 500 keV. The gamma yield of the ^{9}Be(d,nγ)^{10}B reaction is approximately a factor of 8 lower than the yield from the ^{6}Li(d,γ)^{7}Be pure ^{6}Li target reaction. As the atomic mass of the lithium compound increases, the corresponding gamma production cross-section decreases. This is mainly due to the fact that the deuterons have a lower probability to interact with the ^{6}Li atom in a compound compared to a pure metal. Comparing the d-Be with the d-$LiTaO_3$ reactions, we saw about an order of magnitude lower yield because of the low natural abundance of ^{6}Li (7.5%). If we were to enrich the $LiTaO_3$ target to the same level as the other compounds, the yield will be similar to the d-^{9}Be case. (In later discussions of the gamma source powering system, we will see why the d-$LiTaO_3$

reaction is important). Since the yields for all of the reactions are increasing logarithmically with beam energy, the curves indicate that operating at the highest practical beam energy will result in the highest power efficiency. However, the slope of the yield curves starts to decrease at approximately 300 keV and remains fairly constant at the higher incident energies. Furthermore, operating the system at high energies becomes more problematic and is often limited by engineering constraints such as high voltage arcing. Considering the tradeoff between higher power efficiency and difficulty of voltage holding, we believe that 300 keV is an optimal acceleration potential for the above gamma producing reactions.

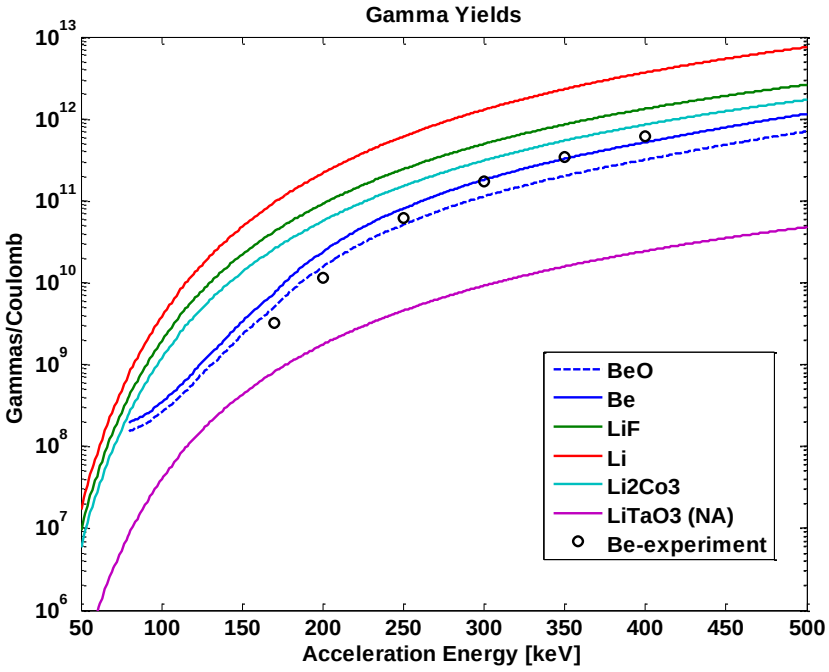

Figure 2.4: Gamma yield per coulomb of incident deuteron ion charge as a function of beam energy.

The present gamma source used the d-^{9}Be reaction because beryllium is more readily obtained commercially compared to lithium-6 for the target material. A Van de Graff ion accelerator at Sandia National Laboratories (Figure 2.5a) was used to produce deuteron beams with energies up to 700 keV and currents up to 10 μA to bombard a thick beryllium target producing gamma rays. Figure 2.5b shows the schematic of the experimental configuration. A 0.010" thick Be target was installed in the analysis chamber and the generated gammas were detected with a 5"x 5" NaI detector. The detector efficiency for the experimental configuration taking into account the solid angle of the detector from the target was 1.5% for the 718 keV gamma rays. The measured gamma spectra acquired at various beam energies are plotted in Figure 2.6. The four lowest energy gammas can be seen for deuterium beam energies above 250 keV, while only the 718 keV gamma ray can be distinguished above background at lower beam energies. The theoretical yield derived from the cross-section calculations is consistent with the measured values.

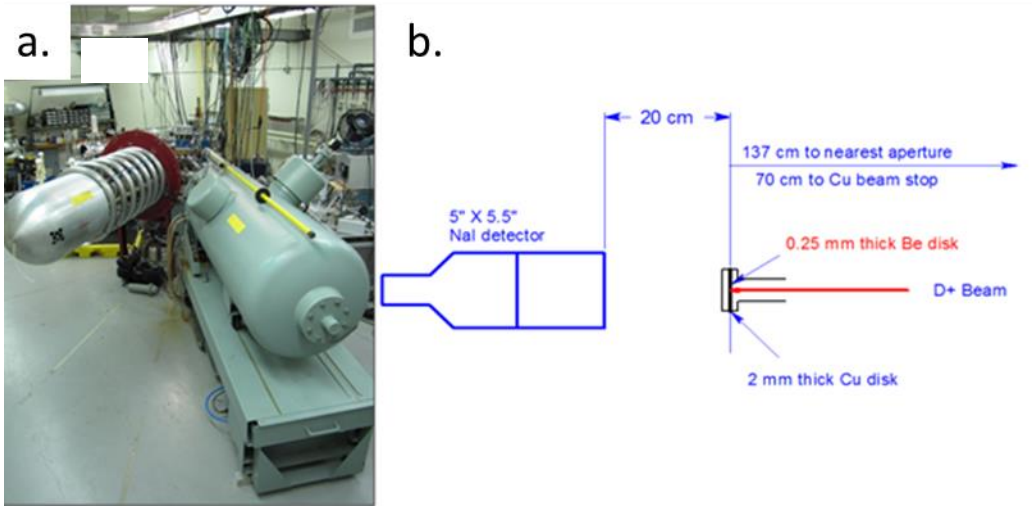

Figure 2.5: a) Photo of Sandia particle accelerator and b) schematic of accelerator experimental arrangement.

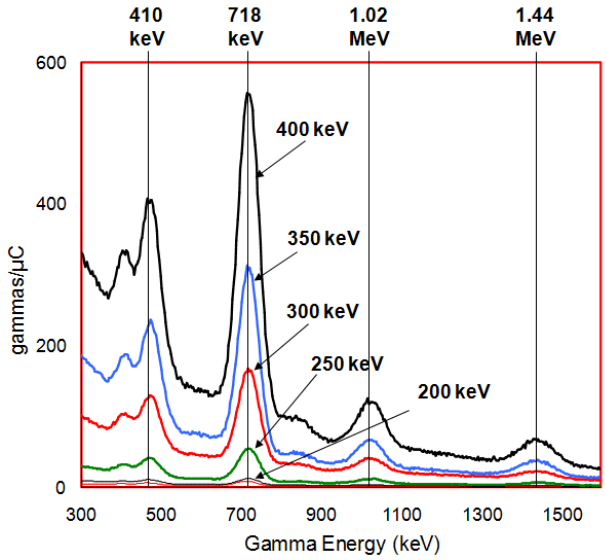

Figure 2.6: Measured gamma spectrum for various beam energies from 200 keV to 400 keV.

II. Neutron Producing Reactions

When we consider the d-Be and d-^{6}Li reactions for gamma production, they are obviously neutron producing as well. Coombe *et. Al.* measured the neutron energy spectrum of the d-Be reaction and determined that it spans the range from 0 – 4.5 MeV with a peak at ~3.5 MeV [19]. Mandeville *et. Al.* measured the neutron energy spectrum for d-^{6}Li reactions and found a bimodal peak of 0.8MeV and 3.4 MeV which corresponds to the (d,nα) and (d,n) reactions respectively [20]. Because both reactions require a solid target preloaded with ^{6}Li or Be, there are potential issues with target sputtering and high current beam damage which leads to lower target lifetime.

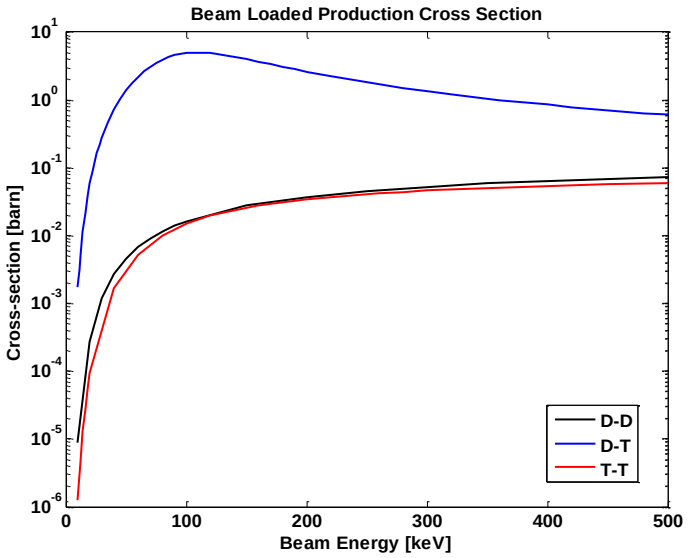

Figure 2.7: Neutron production cross-section for D-D, D-T, and T-T reactions.

More widely used neutron production reactions are the beam loaded target reactions involving deuterons (D) and tritons (T), which are the so-called D-D, D-T, and T-T reactions.

D-D: $$^{2}_{1}H + ^{2}_{1}H \longrightarrow ^{3}_{2}He + ^{1}_{0}n + 3.27MeV \quad (1.4)$$

D-T: $$^{2}_{1}H + ^{3}_{1}H \longrightarrow ^{4}_{2}He + ^{1}_{0}n + 17.6MeV \quad (1.5)$$

T-T: $$^{3}_{1}H + ^{3}_{1}H \longrightarrow ^{4}_{2}He + 2(^{1}_{0}n) + 11.3MeV \quad (1.6)$$

Because the reaction is beam loaded, deuterium and tritium are continuously replenished as the ion beam bombards a metal backing target substrate. The substrate is usually titanium or scandium because they readily form deuterides and tritides when impinged upon by a deuteron or

triton beam. Furthermore, the cross-sections of all three reactions (D-D, D-T, T-T) are much higher than the d-^{6}Li and d-^{9}Be reactions (Figure 2.7). The stopping power of deuterons and tritons in TiD_2 and TiT_2 is also shown in Figure 2.8. For purely monoatomic beams, the maximum yields are calculated and shown in Figure 2.9.

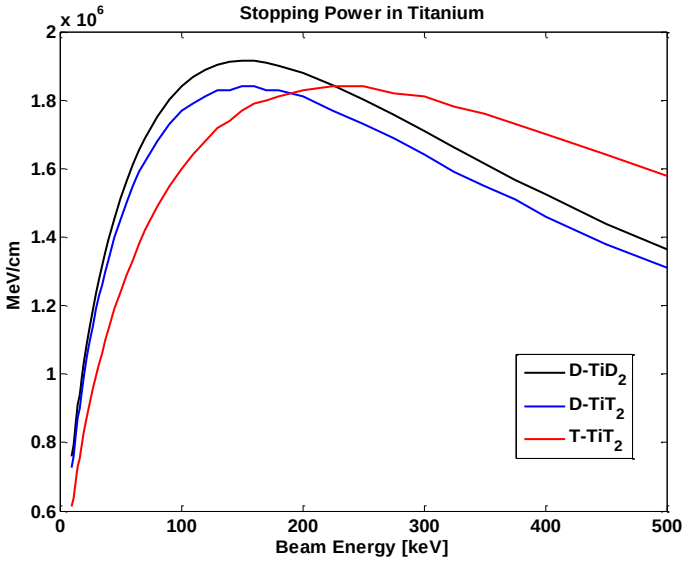

Figure 2.8: Stopping power as a function of energy for D-D, D-T, and T-T reaction in titanium.

Comparing the yields per coulomb of incident ion charge, the beam loaded neutron yields using D-T is about two orders of magnitude higher than D-D and T-T, and about three orders higher than the d-^{6}Li compounds, four-orders higher than d-^{9}Be yields and about five-orders higher than d-$LiTaO_3$. In terms of achieving high yields, D-T is the obvious choice. Because tritium is a beta emitter with a 12.32 year half-life, neutron generators that use tritium must be operated as a sealed source [21]. Without continuous pumping of the vacuum chamber, it becomes very difficult to operate a high yield D-T source due to voltage breakdown issues. On the other hand, a D-D source can be operated with less safety restrictions because such a system contains absolutely no radioactive materials.

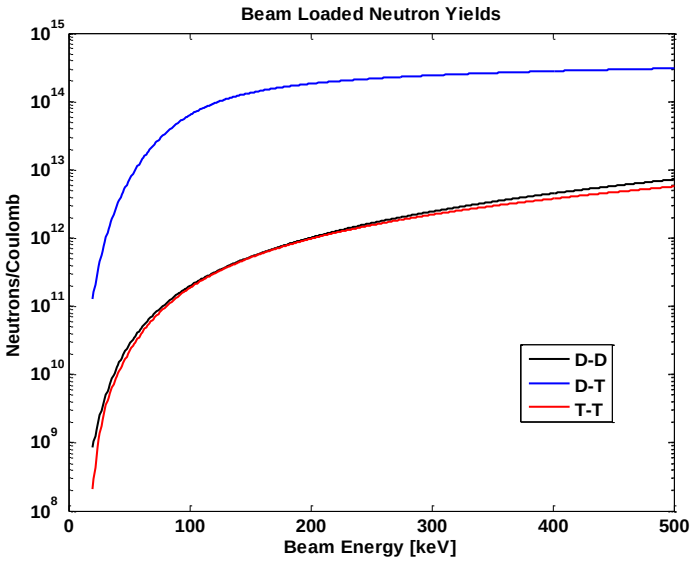

Figure 2.9: Neutron yields for the D-D, D-T, T-T reactions per Coulomb of incident deuteron charge as a function of energy.

Comparing the neutron energy spectra (Figure 2.10), the T-T reaction has an average energy of ~4.7 MeV and its shape matches most closely with that of the Am-Be source (average energy of ~4.1 MeV). This could be advantageous for oil well logging applications that have extensive data archives based on using Am-Be. Because of these spectral similarities, a direct replacement with a T-T source can be done more directly and easily compared with using D-D and D-T sources [22]. On the other hand, the 2.45 MeV D-D neutron source energy is easier to thermalize in the formation and, consequently, becomes more sensitive to changes in hydrogen content.

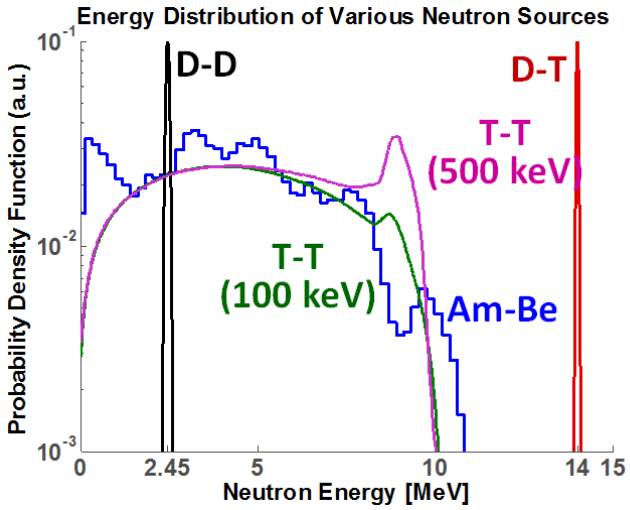

Figure 2.10: Neutron spectrum for the different neutron sources.

III. Neutron to Gamma Converter

The $^{9}Be(d,n\gamma)^{10}B$ and $^{6}Li(d,\gamma)^{7}Be$ reactions produce both neutrons and gammas. For some applications, such as oil well logging, the extraneous neutrons can be useful for simultaneous logging of the porosity. For medical applications, such as cancer treatment, the extra neutrons can add unwanted radiation dosage to the patient. It is possible to design a neutron converter around the gamma source device composed of borated polyethylene (BP). The neutrons generated by the nuclear reaction are slowed by the hydrogen in the polyethylene and then interact with boron in the BP to produce 480 keV gammas via the neutron capture reaction, $^{10}B(n,\alpha\gamma)^{7}Li$. From the perspective of the gamma source, this is very advantageous. In addition to filtering out the unwanted neutrons, the gamma yield is also increased at the same time. It is well known that the $^{10}B(n,\alpha)^{7}Li$ has a much higher cross-section for thermal neutrons compared to fast neutrons, so optimization of the boron mass fraction in BP is needed to provide the maximum neutron conversion while minimizing the overall neutron converter size.

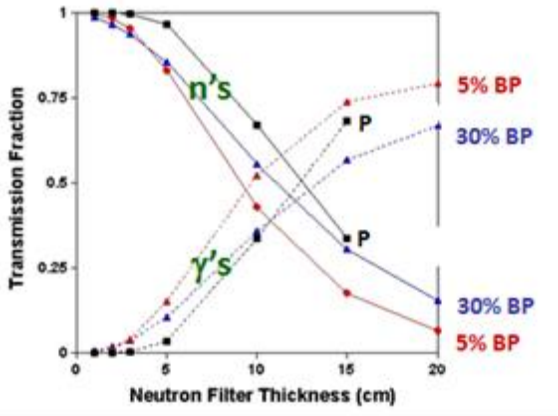

Figure 2.11: The transmission faction of gammas and neutrons through various thicknesses of polyethylene (P) and borated polyethylene (BP) material.

To develop a preliminary design of the neutron converter, MCNPX [23] was used to model the neutron and gamma distributions across slabs of varying compositions and thicknesses (Figure 2.11). Three compositions consisting of 100%, 95%, and 70% polyethylene with complementary percentages of boron are modeled with unit neutron flux and zero gamma flux from one boundary. The neutron and gamma fluxes at various positions (thicknesses) of the slabs are calculated. Based on this simplified shielding model, the 5% BP has the highest neutron conversion performance at thicknesses above 3 cm. However, for thicknesses below 3 cm, 30% BP is the better performer. The modeling results indicate that an optimal neutron converter would consist of layers of polyethylene and BP.

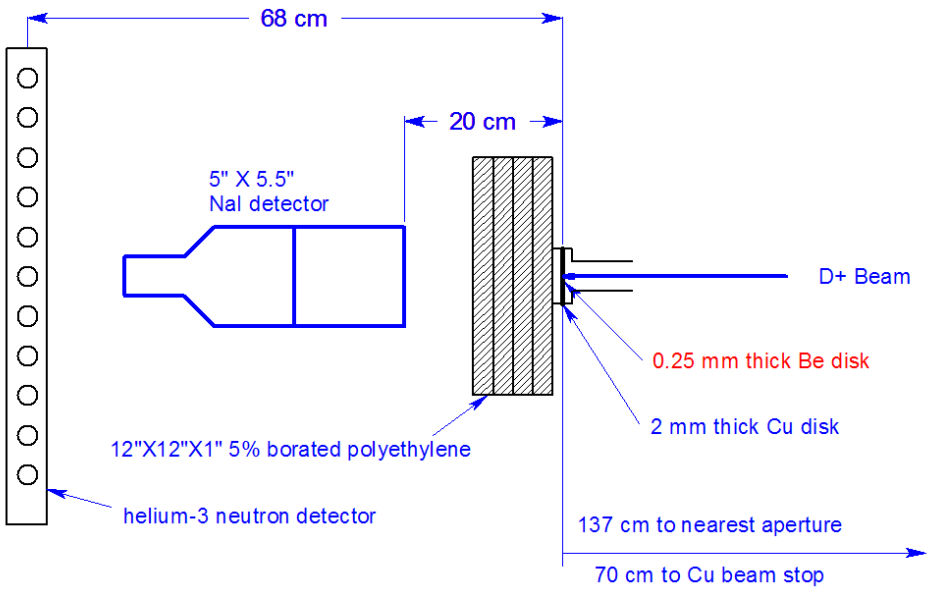

Figure 2.12: Schematic for the neutron converter experiment.

To verify the neutron conversion concept with the Monte-Carlo modeling results, an experiment was conducted on the Sandia particle accelerator to measure the neutron and gamma transmission through 4" of 5% BP. The gammas were measured using a NaI detector and the neutrons were measured with a ^{3}He neutron detector array (Figure 2.12). As seen in Figure 2.13, the 5% BP shielding attenuates the 410, 718, and 1030 keV gammas in addition to converting neutrons to gammas. These results show that the neutron converter was not successful at converting gammas to neutrons because the 480 keV peak remains unchanged after putting on 4" of 5% BP. The reason may be that the gammas generated from the boron capture reaction become attenuated to very low levels before exiting the BP into the detector.

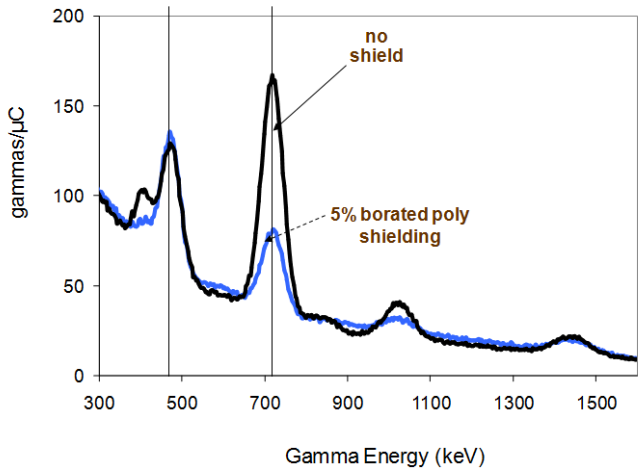

Figure 2.13: Gamma spectrums of measurements with neutron shielding and without neutron shielding.

3. RF Driven External Antenna Plasma Ion Source

I. Modes of Operation

In the present study, an RF driven external antenna plasma discharge ion source [24] was used to produce the ion beams for the reactions discussed in the previous section. The antenna is the spiral-wound planar type which couples 13.56MHz RF power through a quartz dielectric window at the back of the source.

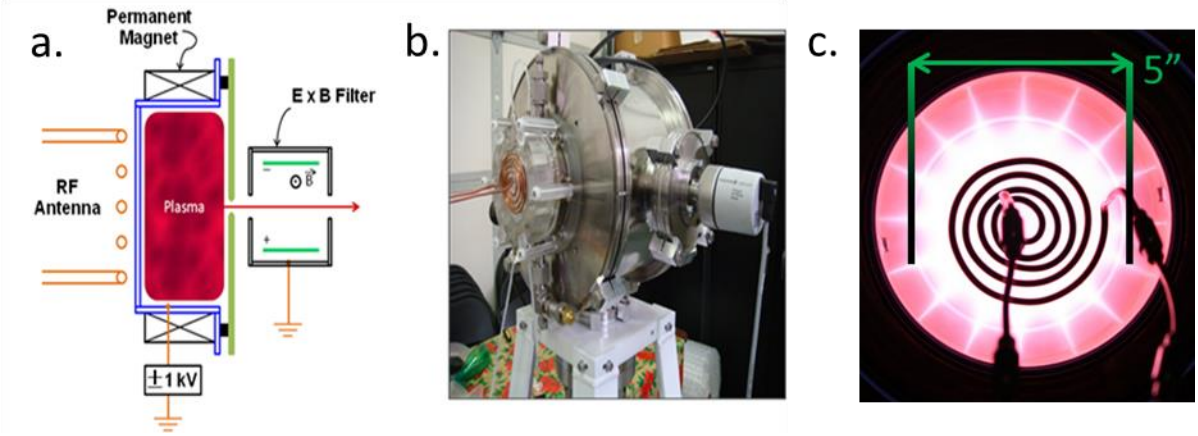

Figure 3.1a shows a schematic of the basic construction of the source. There are three major advantages to using an RF ion source: (1) it allows independent control of the beam current by changing the ion source extraction parameters, (2) the beam quality can be optimized through the use of a ExB or magnetic filter to screen out molecular ions and electrons [25] and (3) a circular array of Nd-Fe-B magnets can be placed around the chamber for better plasma confinement to increase the plasma density (Figure 3.1c).

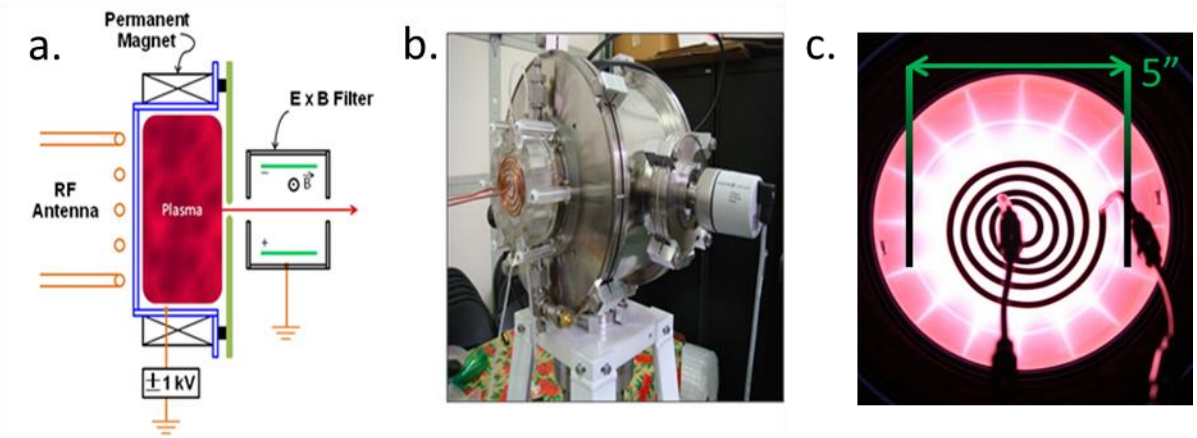

Figure 3.1: (a) Schematic of the RF ion source with an integrated Wien filter. (b) Ion source mounted onto the vacuum chamber. (c) Inductively coupled RF source operating with multi-cusp field lines visible.

There are two basic modes of operation for an RF driven plasma source, capacitive and inductive. The capacitive mode for deuterium plasma is characterized by a dim high pressure (> 300 mTorr) discharge in which the plasma is driven primarily by the voltage drop across the antenna coil and the bulk plasma (Figure 3.2). In contrast, the inductive mode operation can be easily seen with a bright red discharge (for hydrogen) that can be sustained at lower pressures (< 30 mTorr) by an induced electric field within the plasma, which is driven by the current in the antenna coils. The induced electric field is generated by the changing magnetic flux generated by current flowing through the RF coil. In most cases, one would like to operate in the inductive mode because the plasma density is at least an order of magnitude higher than in the capacitive mode [26].

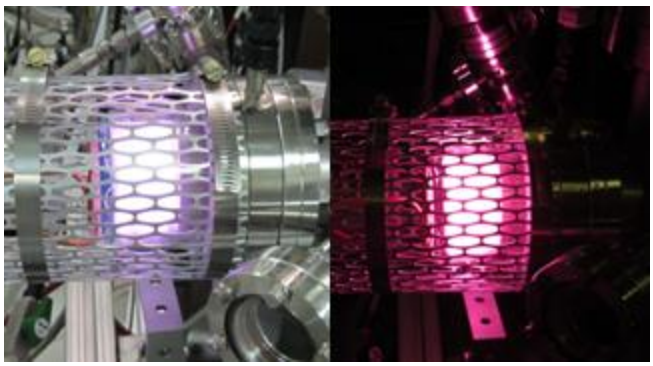

Figure 3.2: RF plasma discharge in capacitive mode (left). Inductive mode (right).

a. Capacitive Discharge

At the plasma boundaries, the extractable current density from a plasma source is given as:

$$j_s = 0.6 n_i q \sqrt{\frac{k_B T_e}{M}} \tag{3.1}$$

where j_s, n_i, k_B, T_e are the saturated ion current density (A/m^2), plasma density (m^{-3}), Boltzmann constant (1.38E-23 J/K), and electron temperature (K), respectively. The saturated ion current is linearly proportional to the plasma density which is itself proportional to the input RF power. For capacitive coupling, the plasma can be maintained at very low RF power (Figure 3.3). Pressure readings of the system showed that the accelerator chamber pressure can be maintained in the 1E-5 Torr range while the ion source chamber is operating in the 1E-2 Torr range. Ceramic standoffs are used to separate the grounded extraction electrode from the ion source with a gap distance of approximately 0.6 cm. Deuterons are extracted by applying a low positive extraction voltage (<5 kV) on the source using low RF power (5-20 W) through a 1 mm aperture. The available ion current depends on several parameters including extraction voltage, gap distance, beam diameter, RF power, plasma density, and the ion temperature [27].

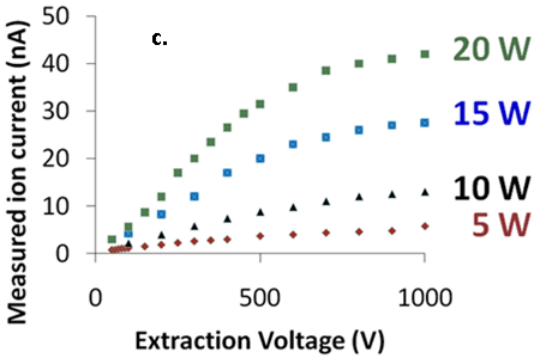

Figure 3.3: Measurement of the ion current as a function of the extraction voltage and RF power.

b. Inductive Discharge

In order to operate stably in the inductive mode, a minimum RF power and pressure must be maintained [28]. Experimentally, we found this level to be ~500W forward power with approximately 10% reflected at 1E-2 Torr in a 5" dia. x 2" length chamber. For reasons that were not well understood, the plasma ignition power and pressure were always greater than the minimum operating power and pressure when using a new (uncoated) dielectric window. Over the lifetime of the ion source operation, the quartz window became increasingly coated with copper from sputtering of the grounded plasma electrode (and/or the metal chamber). It was found that after operating for approximately 40 hours, the ignition power could be reduced to the level of the minimum operating power.

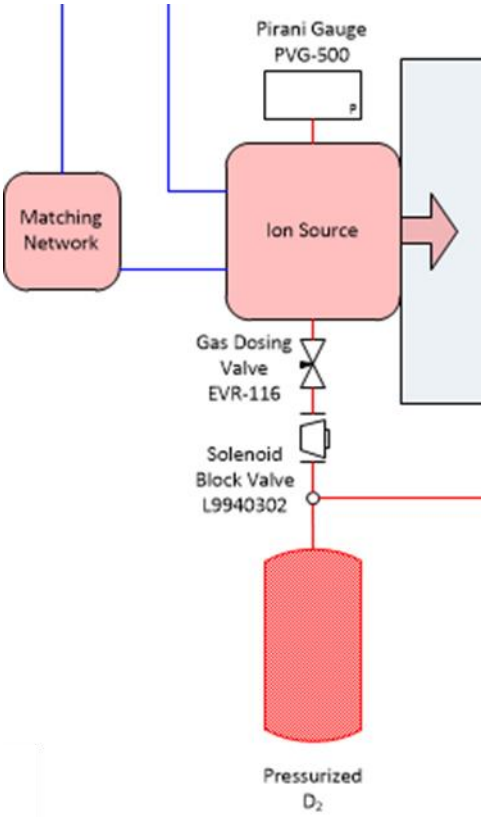

Figure 3.4: Ion source schematic

Based on these observations, we normally used an electromagnetic isolation valve (solenoid block valve) between the needling valve (gas dosing valve) and the ion source as a convenient plasma igniter (Figure 3.4). The typical ion source startup procedure involved setting the needling valve at the desired operating pressure and then closing the isolation valve. Since the ion source vacuum is continuously evacuated through the extraction aperture, the source pressure settles quickly to the high vacuum ultimate pressure. On the other side of the isolation valve, the pressure continues to build up to the line pressure, which we typically set to about zero psig for safety. The RF power is then turned on but will not ignite plasma due to the lack of gas in the ion source. Ignition is achieved almost instantaneously when the isolation valve is opened, which releases a small volume of high density gas into the system, causing the ion source pressure to spike up very quickly. This initial spike in pressure allows the plasma to be ignited in the capacitive mode (high pressure). Shortly after the opening, the pressure settled to the desired low pressure and operated in the inductive mode. This simple design allowed easy control of the capacitive-to-inductive mode transition.

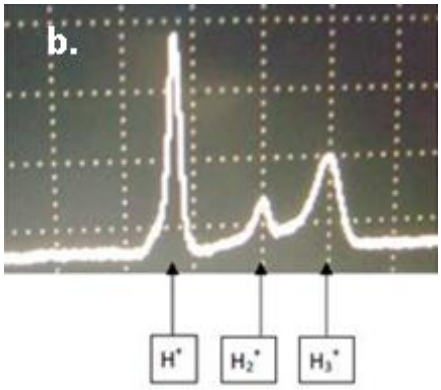

Figure 3.5: Mass spectrometer measurements of the hydrogen ion beam species.

Mass spectrometer measurements of the hydrogen species fractions in the RF discharge ion source show a high fraction of atomic compared to molecular ions (Figure 3.5). As discussed in section 2, a monatomic beam is ideal for the accelerator driven reactions because the full energy per nucleon can contribute to the reaction. During operation of the ion source, a 13.56 MHz RF field is coupled to a quartz chamber that is continuously filled with deuterium gas regulated to a pressure of 1E-2 – 5E-2 Torr using a needling valve. The ion source and acceleration regions are separated by a 1mm diameter aperture to enhance differential pumping of the acceleration chamber. The pumping helps to maintain sufficient gas pressure in the ion source for plasma operation and, simultaneously, preserve the high vacuum in the acceleration chamber necessary to minimize unwanted arc discharges.

For most inductive discharge ion sources, the available ion current is high enough so that the current density is limited by the space-charge repulsion in the extraction region; the current density limit can be approximately described by the Child-Langmuir equation according to

$$j_c = \frac{4\varepsilon_0 V^{3/2}}{9d^2}\sqrt{\frac{2q}{M}} \tag{3.2}$$

where j_c, ε_0, V, d, q, m are the ion current density (A/m^2), free space permittivity (F/m), extraction voltage (V), extraction gap distance (m), charge of ion (C), and mass of ion (kg), respectively. There are three possible modes for extracting from a plasma source: (1) $j_c < j_s$ (diverging beam), (2) $j_c = j_s$ (parallel beam), and (3) $j_c > j_s$ (converging beam). For applications requiring high ion beam currents, it would be advantageous to operate with a diverging beam (Mode 1) in order to lower the power density on the target. However, for applications that require a focused ion beam (e.g. associated particle imaging), it would be advantageous to operate in mode 3 to lower the ion beam spot size on target. A parallel beam with low emittance is extracted in mode 2, which is desirable for injection into subsequent ion optics elements in complex accelerators.

II. E x B Mass Filter

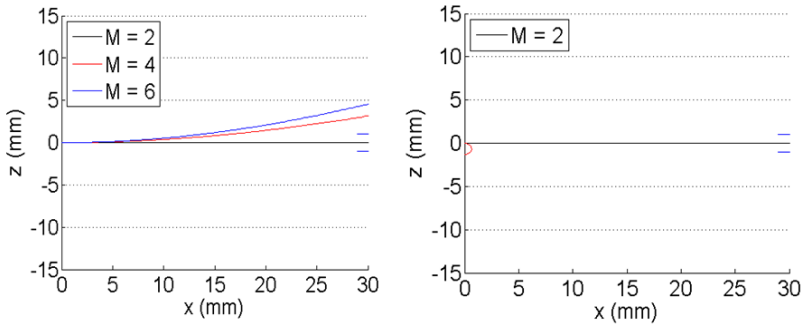

Figure 3.6: Calculated deflections for 1 kV extraction of D+ (left) and D- (right) using the E x B filter.

An E x B Wien filter allows only particles with a certain mass-to-charge ratio (m/q) to pass through undisturbed while deflecting all other particles (Figure 3.6). The kinematics of the particles traveling in the E x B field are governed by

$$x(t) = v_0 t - \frac{1-\sqrt{\beta}}{\beta\omega_0} v_0 sin(\beta\omega_0 t) \tag{3.3}$$

$$z(t) = \frac{1-\sqrt{\beta}}{\beta\omega_0} v_0 [1 - cos(\beta\omega_0 t)] \tag{3.4}$$

$$\beta = \frac{m}{m_0} \tag{3.5}$$

$$v_0 = \sqrt{\frac{2qV_a}{m_0}} \tag{3.6}$$

$$\omega_0 = \frac{qB}{m_0} \tag{3.7}$$

where x(t) is the time parameterized axial (off-axis) distance of ion particle from the extraction and β is the ratio of the particle mass to the undisturbed ion mass (m_o). For an undisturbed ion, β = 1 and t = 0 for all time. The particle velocity, v_o, is given by the extraction energy V_a, w_o is the

cyclotron frequency (Hz) of the undisturbed particle, and B is the magnetic field (gauss). The electric field, E, needed to maintain the undisturbed ion path is given by

$$E = Bv_0 \tag{3.8}$$

Thus, for any given magnetic field strength, there is a unique electric field strength that will allow the ion of interest to pass through the E x B field region undisturbed while all other ions with different m/q ratio will be deflected according to the above kinematic equations. For example, if only the deuterium ions (mass 2) are allowed to pass through the E x B field undisturbed, all other species including molecular ions and electrons are deflected as seen in Figure 3.6 for 1 kV extraction of D^+ (positive ion source) or D^- (negative ion source) ions.

III. d-^{6}Li Beam Loaded Target

Recall that the ^{6}Li(d,γ)^{7}Be reaction can potentially produce four times the gamma yield of ^{9}Be(d,γ)^{10}B. However, a major drawback is the greater difficulty of obtaining a stable enriched ^{6}Li target compared to a beryllium target. One solution is to use beam loading from a mixed Li^+ and D^+ ion source to simultaneously deposit lithium atoms onto a target substrate and hit them with high energy deuterons to generate the reaction. This is very similar to the operation of a typical D-D neutron generator except now there is a heterogeneous mixture of D and Li species rather than a single ion species. Success in demonstrating this technique lies in the high vapor pressure of lithium at relatively low temperatures [29]. At ~500^{o}C, the vapor pressure of lithium is comparable to the gas pressure inside the plasma. This temperature can be easily achieved by resistive heating of small lithium dispensers. The out-gassed lithium atoms are then ionized by the RF discharge and mixed uniformly with the hydrogen plasma. Mass spectrometry results indicate the viability of this technique (Figure 3.7). The three peaks of hydrogen as well as the additional lithium peak are clearly visible.

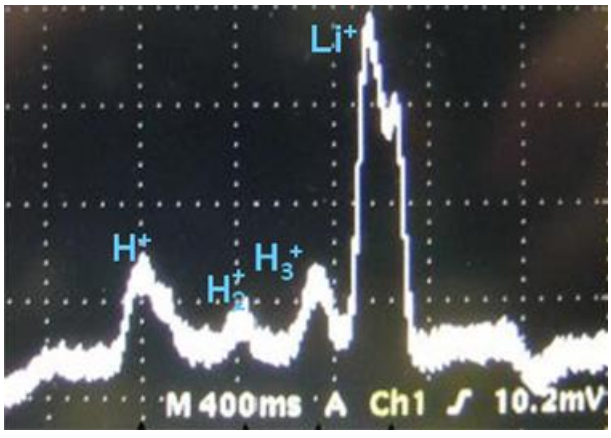

Figure 3.7: Mass spectrometer measurement of the hydrogen and lithium species.

4. Compact pyroelectric driven accelerator

As discussed in section 2, the d-^{9}Be reaction requires accelerating deuterons to approximately 300 keV for optimal gamma yields. Pyroelectric crystal accelerators have previously been demonstrated for bremsstrahlung x-ray and neutron production at lower voltages (maximum ~100 keV). For example, a commercial x-ray generator shown in Figure 4.1a emits x-rays with maximum energy of 35 keV [30]. In recent years, several groups have been developing neutron generators using pyroelectric accelerators based on the D-D reactions [31] [32] [33] [34]. Neutron production has been demonstrated with single 1-cm thick pyroelectric crystals producing voltages up to 100 keV and yields of approximately 10^3 n/s (Figure 4.1b). In a pulsed neutron source, neutron yields of up to 10^{10} n/s have been achieved in a sub-microsecond pulse [35].

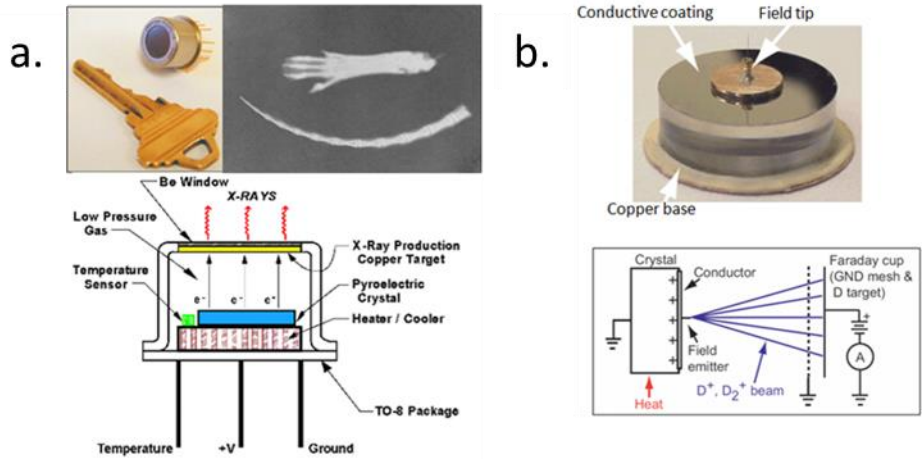

Figure 4.1: a) Commercially available x-ray source based on accelerating electrons to ~35 kV with a pyroelectric crystal. b) Prototype neutron source based on accelerating deuterium ions to ~90 kV with a pyroelectric crystal.

I. Pyroelectric effect

When a pyroelectric material is cooled below the Curie temperature (T_c), the pyroelectric effect can cause a large spontaneous polarization (P) to develop along the polar axis of the crystal that is a function of the bulk crystal temperature [36]. Further, it was determined that for $T/T_c \leq 0.5$, the variation in P with temperature is approximately linear. Therefore, the following two relations hold

$$P = \frac{dP}{dT}(T) \qquad T \leq T_{curie} \tag{4.1}$$

$$dP \cong \gamma dT \qquad T/T_c \leq 0.5 \tag{4.2}$$

The change in polarization with temperature creates an electric field (E) and voltage difference between the two polar faces of the crystal through a relation involving the charge density (D) becomes

$$dD = \gamma dT + \varepsilon dE - (E\sigma + j_i)dt \tag{4.3}$$

where γ is the pyroelectric coefficient (C/m^2/K), ε is the dielectric permittivity, σ is the electrical conductance of the crystal, and j_i is the ion current density impinging on the crystal. The negative term in equation 4.3 defines the time scale for finite resisitive losses through the crystal and external charge impinging onto the crystal. The voltage (V) across the crystal can be determined by integrating the electric field along the length, L.

$$V(x,y) = \int_0^L E(x,y,z)dz \tag{4.4}$$

Assuming the loss $E\sigma dt$ is negligible (a fairly good assumption for our application) compared to γdT and εdE and there are no external charges introduced on to the crystal (no ion-beam bombardment), then equation 4.3 can be simplified to

$$dE = (\gamma/\varepsilon)dT \tag{4.5}$$

This expression can be used to define a figure-of-merit for the pyroelectric crystal accelerator in terms of the γ/ε ratio. It should be noted that the above expressions also assumes negligible stray capacitance such that $\varepsilon = \varepsilon_{crystal}$. As will be discussed in the upcoming sections, this assumption is generally true for a short and medium length ($L \leq 3\ cm$) crystal, but is not accurate for a long crystal ($L \geq 10\ cm$). For the case where resistance of the crystal is non-negligible, or an ion beam is impinging on the system, the pyroelectric equation becomes

$$\frac{dE}{dt} = \frac{\gamma}{\varepsilon}\frac{dT}{dt} - \frac{1}{\varepsilon}(\sigma E + j_i) \tag{4.6}$$

From equation 4.6, two observations can be made: (1) if the temperature is held constant, any electric field present in the crystal will eventually decay to zero; (2) for a finite, constant rate of heating or constant ion current on the system, the electric field eventually reaches a steady state maximum value given by

$$E_{max} = \frac{1}{\sigma}\left(\gamma\frac{dT}{dt} - j_i\right) \qquad \frac{dT}{dt}, j_i = const \tag{4.7}$$

The present gamma source uses an external ion source providing full control of j_i, so that the ion current becomes a parameter that is independent of the crystal voltage. Previous pyroelectric crystal-based approaches have coupled the ion source to the crystal. For example, micro-tips have been attached to the high voltage polar face of a crystal to generate ions via field ionization and field desorption [31]. The disadvantages of this approach are that field ionization/desorption inherently requires high gas pressure which enhances voltage breakdowns and neutralization of the pyroelectric charge. In addition, the ion beam quality (ratio of monatomic ions to molecular ions) cannot be determined during operation. As was discussed earlier, molecular ions contribute little to gamma production and consequently waste pyroelectric charge that provides the high voltage and causes high variance in the gamma yield.

II. Material properties

A survey into the literature of pyroelectric materials shows that lithium tantalate ($LiTaO_3$) is the most promising candidate for use in a high voltage accelerator application due to its high pyroelectric coefficient, low dielectric constant, high Curie temperature, and high resistivity. The resistivity has been calculated (Figure 4.2) based on experimental results from previous researchers who attempted to measure the bulk and surface currents of $LiTaO_3$ at temperatures ranging from 0°C to 160°C [37]. The following fitting equations had been used to summarize the data

$$log_{10}(\rho) = 4.6\left(\frac{1000}{T}\right) - 0.573 \qquad T \geq 100℃ \tag{4.8}$$

$$log_{10}(\rho) = -1.349\left(\frac{1000}{T}\right)^2 + 9.879\left(\frac{1000}{T}\right) - 5.07 \qquad T \in (0,100)℃ \tag{4.9}$$

For temperatures near the Curie temperature, the resistivity rapidly decreases with temperature. In the lower temperature range, there appears to be a maximum in the resistivity ~7°C. Based on

the previously derived results, this is the best range of temperatures to operate the pyroelectric accelerator because intrinsic resistive loss inside the crystal is at a minimum.

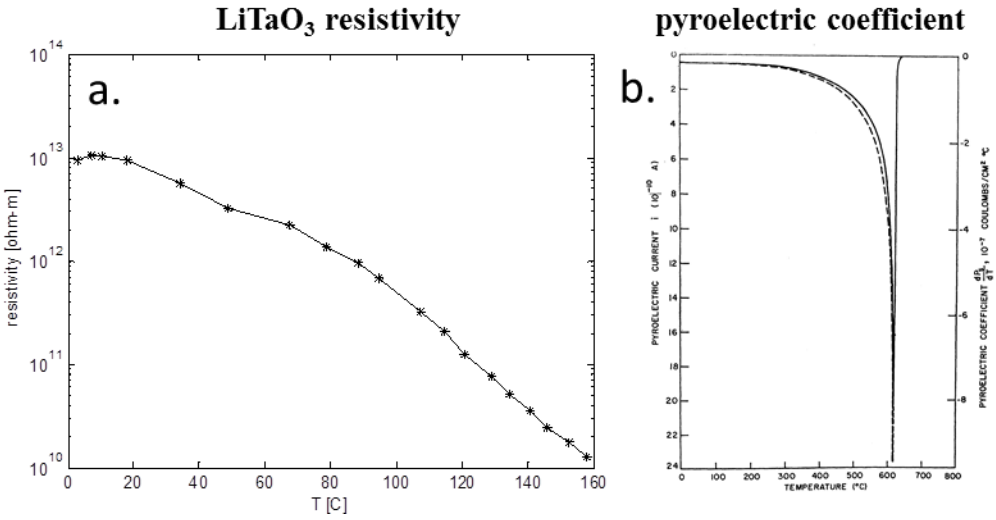

Figure 4.2: LiTaO3 resistivity and pyroelectric coefficient as a function of temperature.

Lithium tantalate also has one of the highest pyroelectric coefficients at room temperature (Figure 4.2). Data from several sources indicate that the pyroelectric coefficient lies in the range of 1.9E-4 to 2.3E-4 C m^{-2} K^{-1} [31] [32] [35] [38]. It is interesting to note that the pyroelectric coefficient increases with increasing temperature up to the Curie temperature, which is approximately 618°C for $LiTaO_3$. Above the Curie temperature, the pyroelectric effect no longer exists.

At room temperature, the dielectric permittivity $LiTaO_3$ crystal is relatively constant at ~$45\varepsilon_0$. At high temperatures (> 450°C), the dielectric permittivity obeys a Curie-Weiss law in which the Curie-Weiss temperature equals the Curie temperature:

$$\varepsilon^{-1} = -0.72 \cdot 10^5 (T - T_c) \qquad 450℃ < T < 618℃ \tag{4.10}$$

Detailed list of the properties at room temperature for $LiTaO_3$ is shown in Table 4.1.

Table 4.1: Electronic and thermal properties of LiTaO3.

	symbol	value @25C	unit	Ref
pyroelectric coefficient	γ	1.90E-04	C m^{-2} K^{-1}	[31] [32] [35] [38]
dielectric permittivity	ε	3.98E-10	F m^{-1}	[35]
electrical conductivity	σ	1.00E-13	Ω m	[37]
density	ρ	7.46E+03	kg m^{-3}	[39] [40]
thermal conductivity	k	4.00E+00	W $m^{-1}K^{-1}$	[40]

specific heat	c_p	2.51E+02	J łkg^{-1}K^{-1}	[36] [40]
thermal diffusivity	α	2.14E-06	m^2 s^{-1}	computed
linear expansion coefficient	β	7.40E-05	K^{-1}	[40]

III. Pyroelectric crystal accelerator design

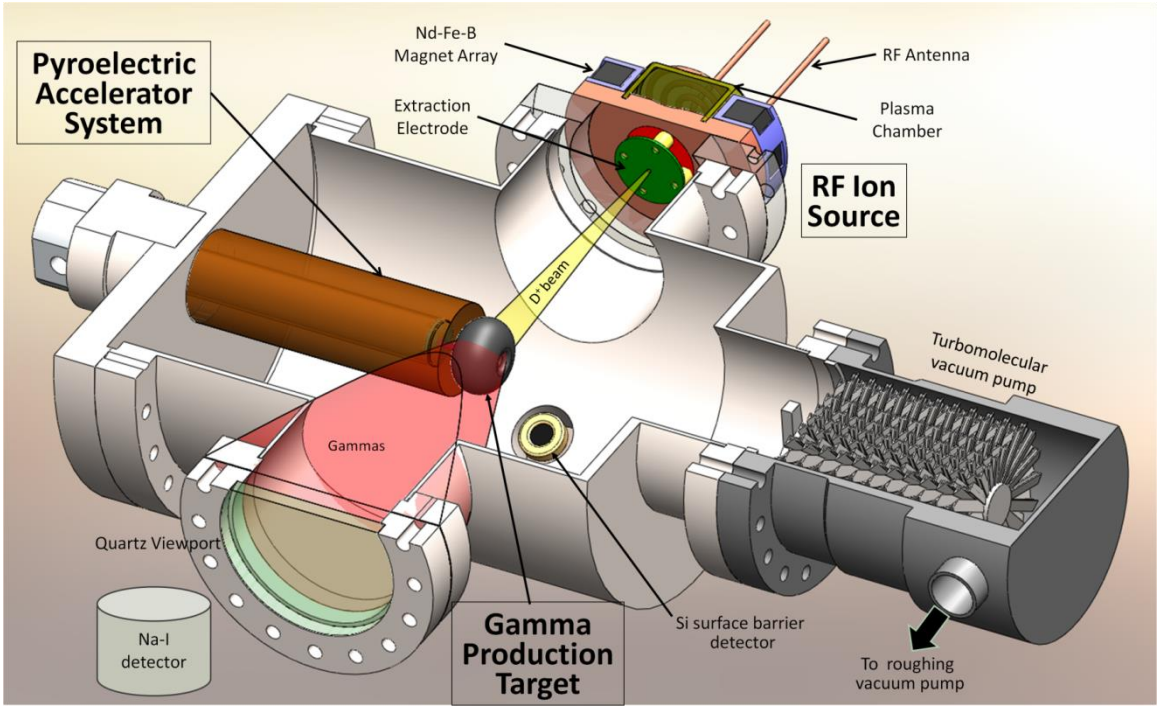

Figure 4.3: 3D schematic showing the main components of the pyroelectric gamma source.

Peltier thermoelectric devices are commonly used to heat and cool the pyroelectric crystal from the bottom polar surface in order to generate the necessary voltages [30]. While these devices provide precise temperature control, the use of conduction type heating is only practical for short (small L) crystals. Based on equation 4.4, longer crystals produce higher voltages for the same amount of temperature change but they are much more difficult to heat/cool efficiently and uniformly. Therefore, the length of the pyroelectric crystal has significant effect on its operational performance. Assuming the bottom face of the crystal can be controlled precisely such that the rate of temperature increase is constant (ψ), the temperature profile across the polar axis of the crystal is given by the 1-D transient heat conduction equation with a time dependent Dirichlet boundary at $z = 0$ and an insulating boundary at $z = L$ can be expressed as

$$\frac{\partial}{\partial z}T(z,t) = \alpha\frac{\partial^2 T(z,t)}{\partial z^2} \qquad T(0,t) = \Psi t \qquad (4.11)$$

$$\frac{\partial}{\partial z}T(L,t) = 0 \qquad (4.12)$$

where α is the thermal diffusivity. The thermal penetration depth is given approximately as

$$\delta = \sqrt{8\alpha t} \tag{4.13}$$

In the case that the thermal penetration depth is greater than the length of the crystal, the temperature profile inside the crystal reaches steady state equilibrium with respect to the bottom boundary, given by a quadratic function in z

$$T(z,t) = -\frac{\Psi}{\alpha}\left(z - \frac{1}{2}z^2\right) + \Psi t \tag{4.14}$$

From equation 4.14, it can be shown that for the same heating rate, the maximum thermal gradient occurs at the bottom surface in the steady state and scales with L while the temperature difference between top and bottom of the crystal scales with L^2. This has important implications for the thermal stress on the crystal because cracking has been observed due to high thermal gradients [41].

$$S_{thermal} = E_Y \beta |T(L,t) - T(0,t)| \tag{4.15}$$

$$S_{thermal} = E_Y \beta \frac{A}{\alpha}\left(L - \frac{1}{2}L^2\right) \tag{4.16}$$

In these equations, E_Y is the Young's Modulus of the material and β is the linear thermal expansion coefficient. Short crystals can be heated/cooled easily but cannot generate very high voltages. Therefore, it is important to optimize the crystal length given the constraints on the accelerator system. In the upcoming sections, we discuss and characterize the different length crystals in terms of their voltage generating performance.

a. **Long crystals (L = 10 cm)**

In preliminary tests for the long crystals, we use a long geometry crystal (1 cm dia. x 10 cm length) with uniform heating and cooling provided by continuous flow of a dielectric fluid (Fluorinert™ FC-70 [42]) around the entire crystal. The crystal is housed in a polytherimide (Ultem-1000) tube as shown in Figure 4.4a.

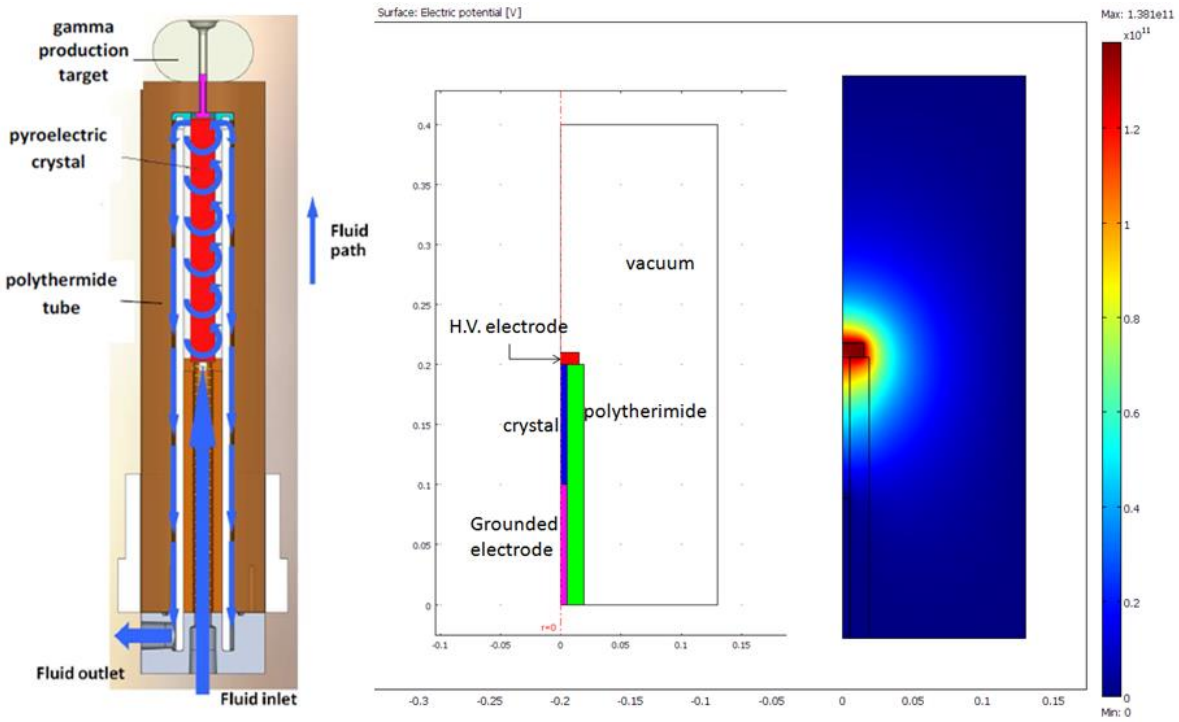

Figure 4.4: a) Schematic showing the design of the dielectric fluid immersion-type accelerator. b) FEM analysis of the electric potential for the dielectric fluid immersion-type accelerator.

Operation of the dielectric fluid immersion accelerator system is shown in the schematic of Figure 4.5. A hot reservoir of dielectric fluid is pumped into the Ultem tube with a volumetric flow rate of approximately 1 L/min to heat the crystal and generate high voltage for gamma production. One end of the crystal polar face is grounded via a metal spring structure connected to the vacuum chamber, while the other end is electrically connected to a sealing screw which protrudes out to vacuum and allows attachment of the beryllium target. The entire accelerator system is flanged inside the 10" vacuum chamber through an Ultra-Torr® adapter.

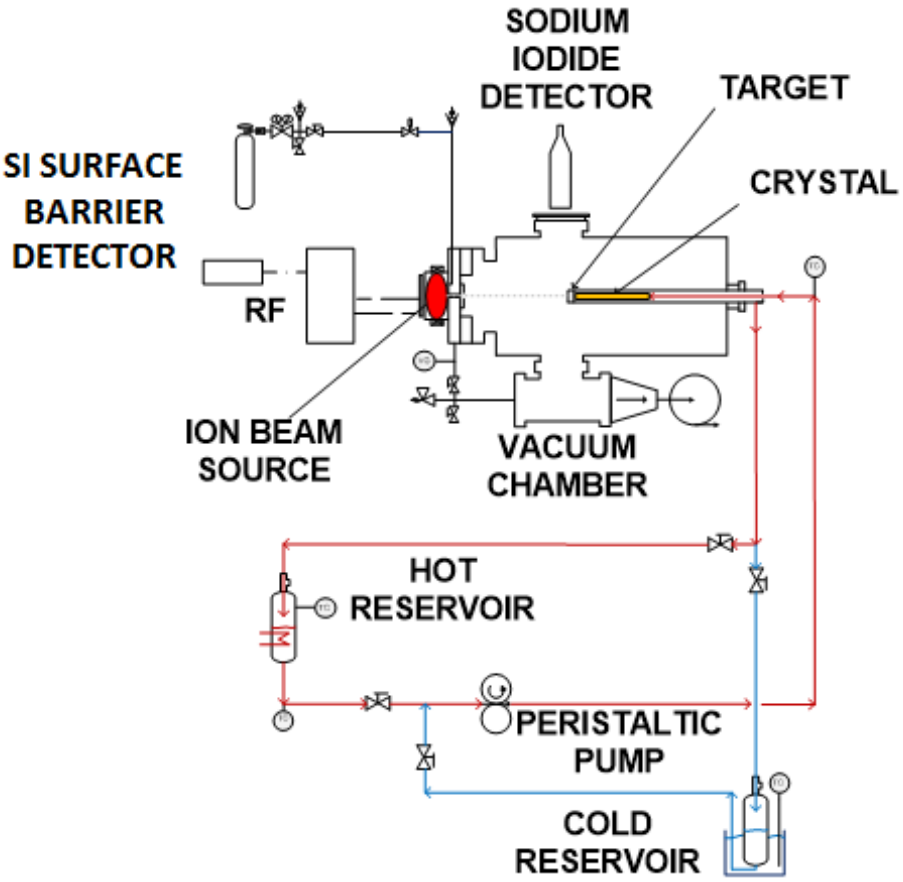

Figure 4.5: Schematic of the heating/cooling system for the dielectric fluid immersion-type accelerator.

Initially, the 1 cm diameter x 10 cm long $LiTaO_3$ crystal was tested because equation 4.4 predicts that approximately one mega-volt could be obtained with only a 21°C temperature change. A long crystal also reduces the electric field gradient across the crystal, providing better voltage holding and operational stability. However, a finite element electrostatics model (Figure 4.4b) of the pyroelectric accelerator system housed in the vacuum chamber shows that the total capacitance is ~7.2 pF. This value is much larger than the 0.4 pF of the isolated crystal itself, which means that the total capacitance is dominated by stray capacitance rather than the crystal capacitance. In this case, the simplified form of equation 4.4 no longer holds and a more comprehensive model that describes the pyroelectric crystal and chamber system is needed.

If the crystal can be treated as a lumped thermal capacitance (Biot number < 0.1), then the spatial temperature variation is negligible and the voltage and charge density across the polar face of the crystal are constant. The charge on the entire crystal polar face, with area A, is described by

$$C_{total}dV = \gamma AdT - (\sigma V + I_{ion})dt \tag{4.17}$$

$$C_{total}\frac{dV}{dT} = \gamma A - \left(\frac{dT}{dt}\right)^{-1}(\sigma V + I_{ion}) \tag{4.18}$$

where C_{total} is the total (crystal + stray) capacitance of the system, I_{ion} is the total ion current impinging on the crystal. Equation 4.18 provides a convenient method to calculate the voltage knowing the temperature profile of the crystal. The approximate transient temperature profile of the crystal was obtained by the following analysis, where the long crystal was modeled as a lumped capacitance problem with a convective boundary.

Based on the properties of the crystal and dielectric fluid, the Reynolds number of the flow was calculated to be 820, which indicates a laminar flow for the purpose of evaluating the convection coefficient (calculated to be ~40 W m^{-2} K^{-1}). The Biot number was calculated to be 0.024 which was consistent with the lumped capacitance assumption. Assuming the dielectric fluid is injected at a constant temperature, temperature of the crystal is then given by

$$\dot{T} = \frac{hA_s}{mc_p}\left(T_{fluid} - T\right) \tag{4.19}$$

where A_s, m, c_p, and T_{fluid} *are* the crystal surface area (m^2), mass (kg), specific heat capacity (J/kg/K), and fluid temperature (K) respectively. The quantity (mc_p/hA_s) is the thermal time constant of the crystal, τ_t, and is approximately 110 seconds for the present geometry. Combining equations 4.18 and 4.19 gives a differential equation of the voltage with respect to temperature as

$$\frac{dV}{dT} = \frac{\gamma A}{C_{total}} - \frac{\tau_t}{C_{total}}\left(\frac{\sigma V + I_{ion}}{T_{fluid} - T}\right) \tag{4.20}$$

Because of the empirical nature of the resistivity, equation is nonlinear and must be solved by integration from the initial to final temperature of interest. For a convectively heated system, the steady state final temperature will be equal to T_{fluid}. In the simple case of low resistive loss and low ion beam current, the voltage can be simplified to

$$\frac{V(T) - V_0}{T - T_0} = \frac{\gamma A}{C_{total}} \tag{4.21}$$

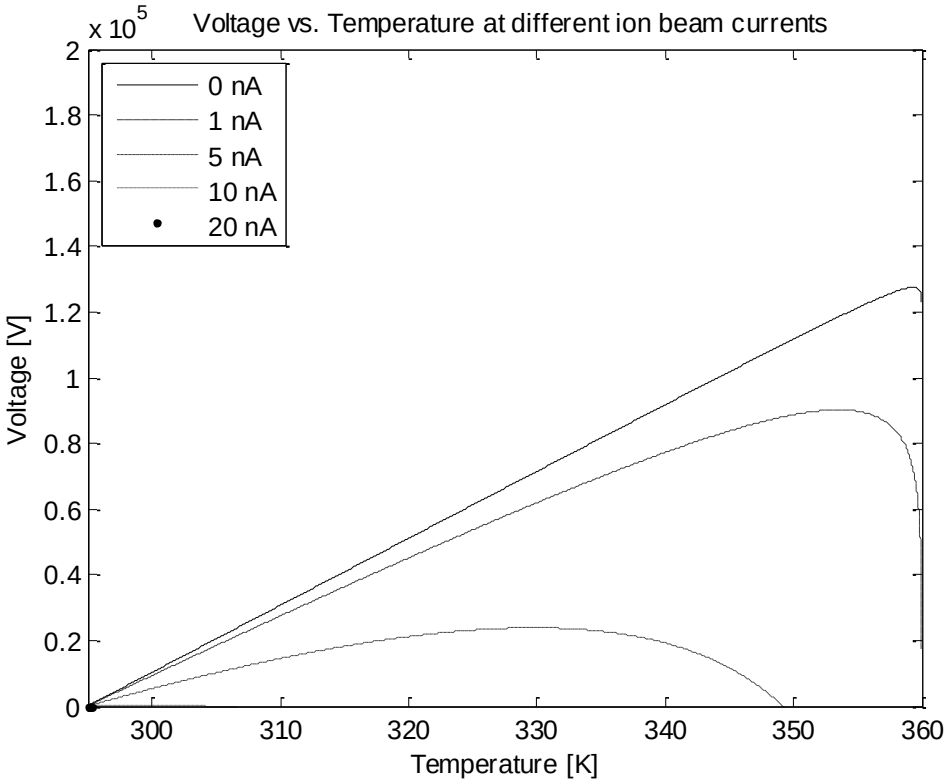

Figure 4.6: Crystal voltage as a function of temperature for different ion beam currents.

If the ion beam impinging on the crystal is non-negligible, equation 4.20 must be solved to find the voltage. Figure 4.6 shows a plot of the crystal voltage versus the temperature of the crystal at different ion beam currents**.** At very low ion beam currents, the voltage increases linearly with temperature until $T_{crystal}$ and T_{fluid} are approximately equal, at which point the heat transfer into the crystal is negligible, and this result is consistent with equation 4.21. As the ion beam current is increased, charge neutralization increases and the maximum achievable voltage during the heating phase is decreased. As the ion beam current is further increased, the crystal can no longer develop any charge because the rate of charge generation is less than the ion beam current.

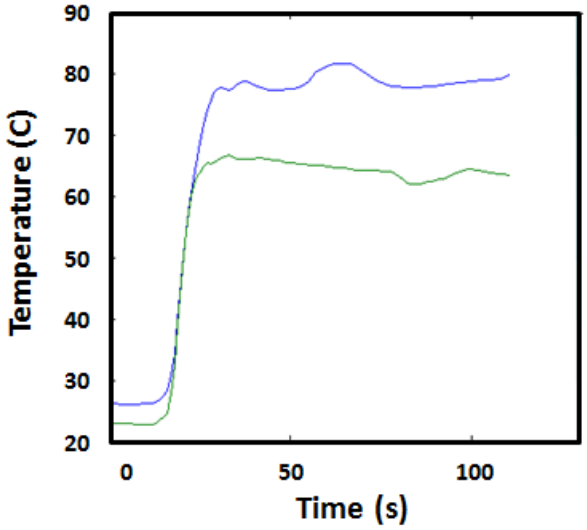

Figure 4.7: Inlet fluid temperature as a function of time. Blue and green curves represent different experimental runs.

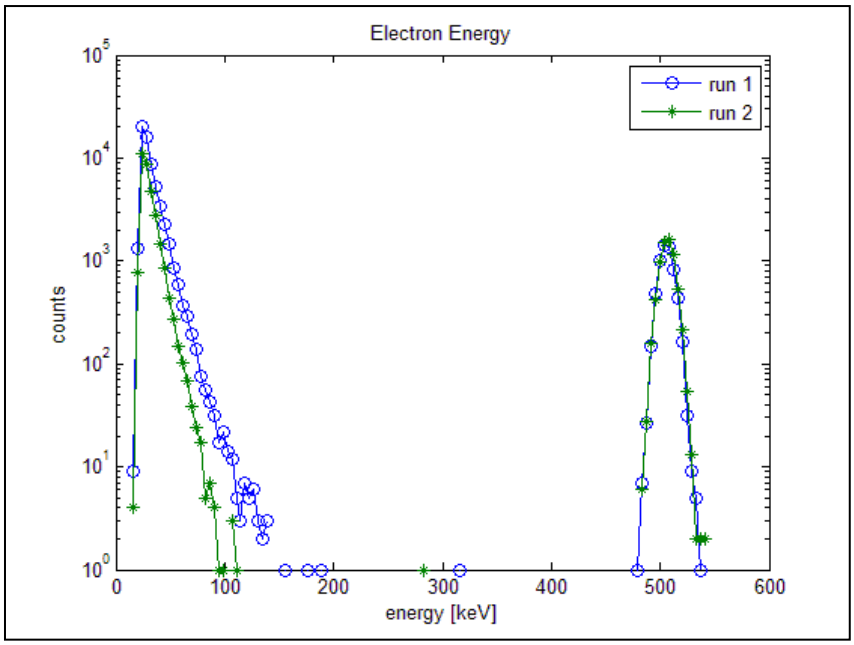

Figure 4.8: Electron energy spectrum measured using a silicon surface barrier detector for two different heating cycles.

Experiments were performed to validate the crystal voltage equation for the condition of no ion beam current (Eqn. 4.20). The fluid temperature was monitored with thermocouples placed in the fluid reservoirs and at the grounded end of the pyroelectric crystal. A LabVIEW™ [43] program is used to control the flow rate and reservoir temperature. The T_{fluid} parameter is determined by the thermocouple closest to the crystal. After starting the flow, it was observed

that approximately 10 seconds was needed for the fluid temperature to reach the steady state hot fluid temperature (Figure 4.7). This time delay implies that the thermal time constant of the fluid pumping system is much lower than the time constant of the crystal (around 110 seconds). This time constant was expected since the crystal housing structure is composed mainly of a very low thermal conductivity plastic and the fluid tubing is composed of silicone, which also has a low thermal conductivity. Thus, the effect of heat leakage to the pumping system can be neglected.

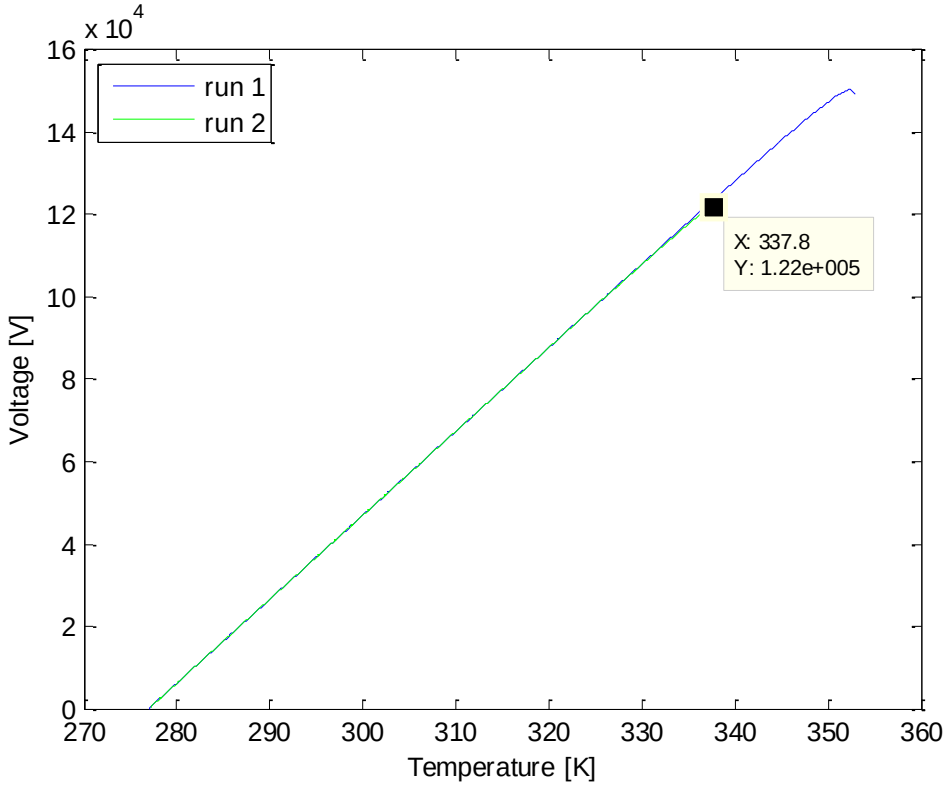

Figure 4.9: Computed voltage as a function of temperature.

A silicon surface barrier detector was used to measure the field emission electron energies corresponding to the crystal voltage during the heating phase. Figure 4.8 shows the energy spectrum obtained from the detector. Trial one (blue) corresponds to a fluid temperature of 353^{o}K, while trial two (green) corresponds to a fluid temperature of 338^{o}K. The maximum voltages predicted by the crystal voltage model (Figure 4.9) are 150kV and 122kV, respectively, given the experimental parameters. The measured electron energy spectrum did not show a clear peak that lied beyond the noise level, which is about 30 - 40 keV for the surface barrier detector. However, the evidence does confirm the generation of high energy electrons from the crystal surface as the background spectrum shows no electron population above ~40keV. It is possible that the measured crystal voltage fell short of the theoretical maximum due to some type of leakage current.

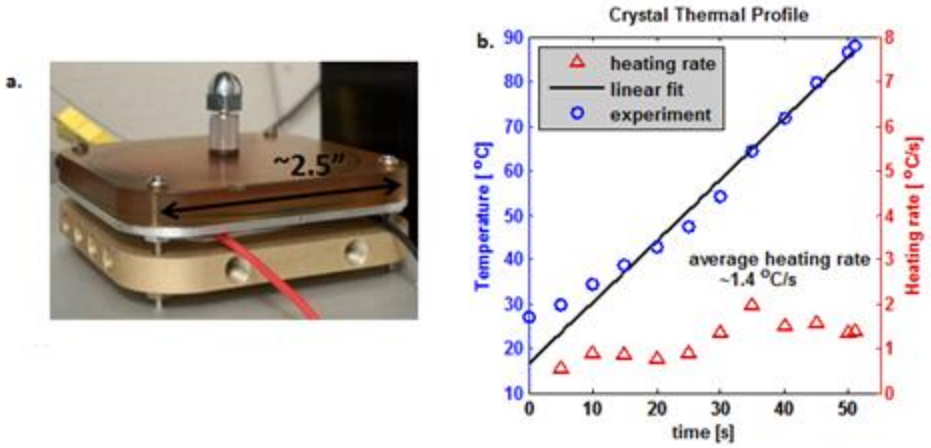

Figure 4.10: a) Photo of a high voltage heating/cooling module. b) Crystal heating rate as a function of time.

b. Short crystals (L = 0.1 cm)

In contrast to long crystals which require convective fluid flow around the entire crystal, uniform and fast heating/cooling can be accomplished with thin crystals using thermoelectric modules. For example, one millimeter thick crystals have at least an order of magnitude higher heating rate compared to the 10 cm long crystal without sacrificing temperature uniformity. The latter effect results in higher yields and more stable operation. A novel high voltage heating/cooling module was designed and fabricated to accommodate a thin 50 mm diameter x 1 mm long (thick) crystal (Figure 4.10a and Figure 4.11). The bottom of the crystal was precisely controlled to with an average heating rate of 1.4°C/s from 27°C to 89°C before discharge breakdown occurred. Based on equation 4.5, the electric field across the crystal was 22 kV/mm.

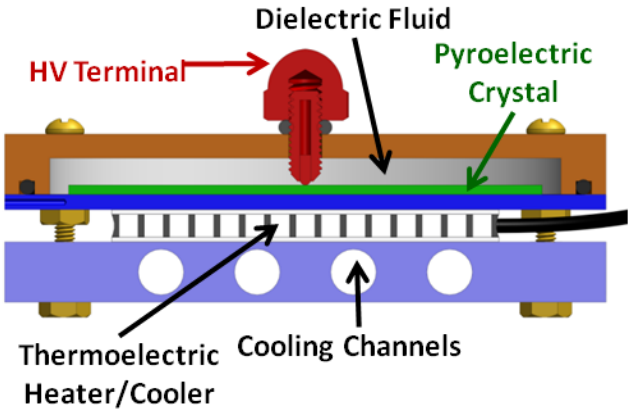

Figure 4.11: Schematic showing the main components of the high voltage heating/cooling module.

The experimental limit in $LiTaO_3$ crystals due to the coercive field of 22 kV/mm [44] was demonstrated in this module. In normal operations, the crystals would be charged up by heating (cooling) the dielectric fluid to produce more conservative electric fields of ~15 kV/mm [45]. The dielectric fluid was chosen for its high boiling point which helps to reduce vapor formation during heating. Vaporization was also suppressed in this modular design because the fluid was contained in a closed volume with only a small (~0.1mL) air pocket. At the onset of bubble formation, the system is pressurized which suppresses the vapor pressure. The capacitance of a single crystal module was measured to be ~1 nF. Table 4.2 summarizes the electrical characteristics of the three different sized crystals that were tested. Notice that for the 1 mm long crystal, the sustained electric field is 3 times higher than the 10 mm long crystal and over 5 times higher than the 30 mm long crystal.

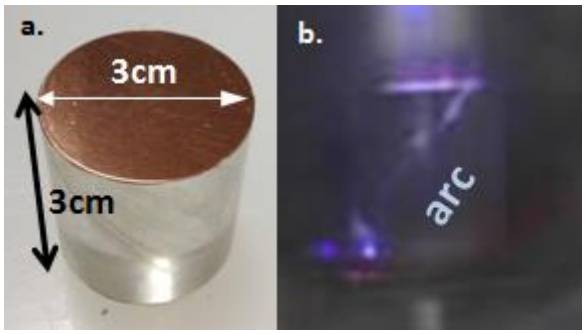

Figure 4.12: a) LiTaO3 crystal with copper conductive plate attached to one end. b) High voltage electrical breakdown along surface of crystal.

c. Medium length crystals (1 cm ≤ L ≤ 3 cm)

Because it was not possible to generate very high voltages with the thin crystals, slightly longer single crystals (1 – 3 cm length) were studied for producing higher voltages. Initial testing of these crystals was performed with the entire crystal in vacuum to provide high voltage standoff. Heating and cooling was achieved using thermoelectric modules attached to the base of the crystal (Figure 4.12a). Preliminary results using both 30 mm dia. x 10 mm thick and 30 mm dia. x 30 mm thick crystals show that the voltages of 75kV and 125kV could be measured using a silicon surface barrier detector. For this configuration, it was found that electrical breakdown between the two polar faces in vacuum was an issue (Figure 4.12b). In order to reduce the likelihood of breakdown, the 30 mm length crystal was immersed in a Fluorinert bath similar to the thin crystal in the high voltage module. The high voltage end was exposed to vacuum to allow generation of bremsstrahlung x-rays and the end-point of the x-rays will indicate the high voltage achieved by the crystal. Using a HPGe detector, the highest voltage obtained was ~180kV by cooling the crystal with an ice bath from ambient 20^{o}C to approximately 0^{o}C (Figure 4.13). Although it was difficult to obtain any measurable gammas from the d-^{9}Be reaction at 180 kV, the neutron yields at this beam energy is quite significant (Figure 2.9).

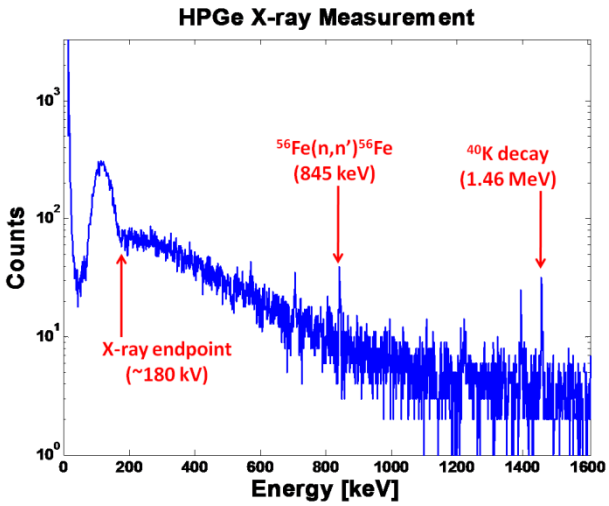

Figure 4.13: Measured X-ray energy spectrum from a single 3 cm diameter x 3 cm long LiTaO3 pyroelectric crystal that was cooled from ~20C to 0C.

Table 4.2: Electrical Characteristics of Tested Pyroelectric Crystals (red) our results, (black) other results. HPGe refers to high-purity germanium detector and PIPS(Si) refers to passivated implanted planar (silicon) detector.

Thickness (cm)	E-field (MV/m)	ΔT (K)	Method of Heating	Method of Measurement
0.1	22	45	Thermoelectric	Surface field meter
0.2	18.5	38	Thermoelectric	HPGe
0.4	9-9.75	18 – 20	Infrared Laser	HPGe
1	7.3 – 10.5	15 – 22	Thermoelectric	PIPS (Si), HPGe
3	4.2 – 6	8.6 – 12.3	Thermoelectric	PIPS (Si), HPGe
10	1-3	2 – 6	Fluid quench	Surface field meter

IV. Pulsing techniques to achieve high gamma flux

a. Pulse stacking of individual modules

As discussed earlier, the pyroelectric crystal powering system needs to operate at >300 kV to generate high gamma yield. However, as the voltage increases above 100 kV, field emission and

corona losses become increasingly larger [35]. Because the pyroelectric powering system is a charge limited device, the voltage will stop increasing when the charge generation rate equals the charge loss rate which puts an upper bound on the highest obtainable voltage. One way to overcome this barrier is to operate the crystals in pulsed mode by stacking the crystals into a series configuration that minimizes the charge loss (operational duration of no more than a few microseconds). Figure 4.14 shows stacking four 1 mm thick crystal modules that initially are each charged to a voltage of ~15 kV. At the high voltage terminal, the arc distance in air-to-ground (~2.8 cm) confirmed that a final stacked voltage of greater than 60 kV was achieved.

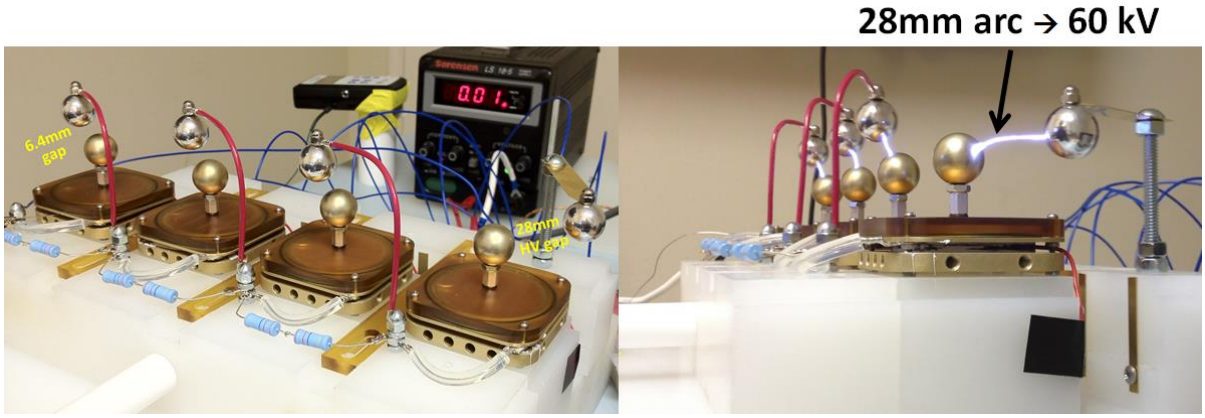

Figure 4.14: Photos of a stacked high voltage acceleration system. The 28 mm arc distance indicates a stacked voltage of > 60 kV is achieved by the four modules.

Currently, the thin crystals are heated by thermoelectric heaters which are attached directly to the crystals. To attain at least 300 kV for high gamma production, a system of twenty pyroelectric crystal modules would be stacked in a mounting device that also isolates the thermoelectric heater power from the high voltage. During the charging phase, all of the crystals are grounded on the bottom through a network of resistors. However, during the discharge phase, the crystals are floated to high voltage. As a result, the thermoelectric heaters (which draw power from a grounded circuit) must be well isolated from the crystals. The voltage isolation of the alumina plate and epoxy seal on the thermoelectric devices are limited to voltages < 50kV and, thus, become problematic at higher voltage. One solution is to use quartz lamp radiative heating with the stacked pyroelectric system due to better voltage isolation during operation (Figure 4.15) [46]. Because radiative heating is a non-contact method of heat transfer, the quartz lamps can be placed far away from the crystals, simplifying the complexities of voltage isolation. Using the same geometric setup as the stacked thermoelectrically heated system above, the crystals were stacked and heated from 27^{o}C to 80^{o}C using four quartz lamps. Voltage stacking was again demonstrated for this configuration (Figure 4.16).

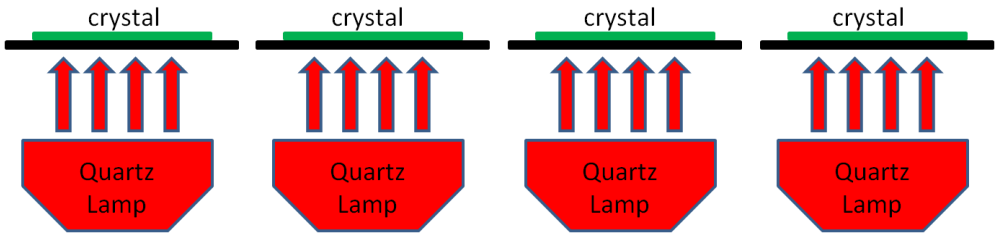

Figure 4.15: Schematic showing a stacked pyroelectric crystal accelerator using quartz lamp heating.

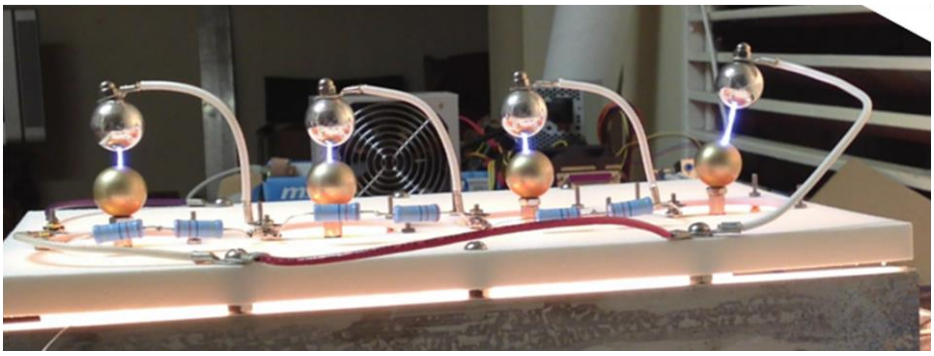

Figure 4.16: Photo of the stacked quartz lamp heated pyroelectric crystal accelerator.

Because of the non-optimal configuration of the quartz lamps, the four crystals were not uniformly heated (Figure 4.17). Measurement of the temperature at the base of each crystal indicates a maximum temperature difference of ~10^{o}C between the outer (modules 1 and 4) and inner crystals (modules 2 and 3). Based on the properties of the crystals, this corresponds to approximately 5 kV voltage difference. To mitigate this effect, better control of the quartz lamp power to each quartz lamp or a more optimized design of the lamp heating configuration would need to be developed.

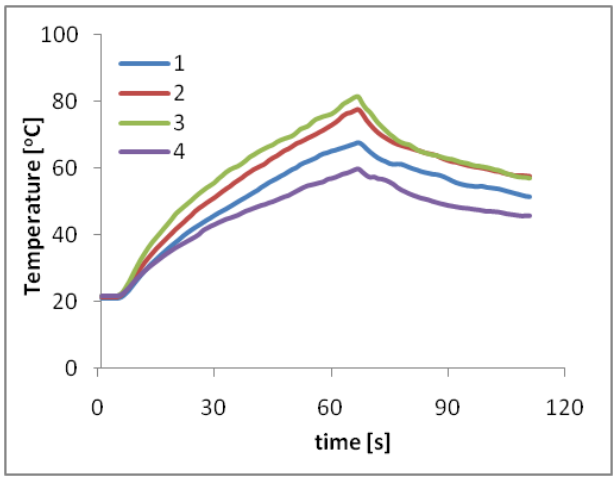

Figure 4.17: Temperature at the base of the crystal as a function of time. Numbers 1-4 represents crystals from left to right.

b. Fast mechanical shutter

When compared to operating in continuous wave (cw) mode, pulsed ion beams have the advantages of requiring lower power consumption and producing higher beam intensity. The usual way to produce pulsed beams is to electrostatically or magnetically sweep the ion beam across an aperture. Another approach uses electronic pulsing of the ion beam with extraction grid voltage. The latter method has the advantage of producing very short pulses with relatively fast (millisecond) rise and decay times [47]. In the case of RF- or microwave-driven plasma ion sources, it is common to pulse the generator while keeping the extraction grid voltage constant producing a pulses with sharp rise and decay times [48]. A drawback of all these pulsing techniques is maintaining vacuum isolation between the analysis chamber (at high vacuum) and the ion source (which operates at higher pressures). For example, the pressure in RF-driven plasma sources must be maintained at roughly 1E-2 Torr for optimal source operation, but the acceleration chamber needs to be in the less than 1E-4 Torr range for maximum voltage standoff. Pyroelectric crystal-powered accelerators have been limited due to voltage breakdown across a vacuum gap [35] [38] [49] and, in addition, high vacuum is needed to avoid neutralizing negative ion beams [50]. As a result, conventional methods require a high amount of differential pumping in order to maintain the pressure difference in the main chamber since the ion source is directly connected to the chamber through the extraction aperture. An alternative approach using a mechanical shutter was explored to maintain vacuum isolation without differential pumping [51]. The requirements for the gamma source were to 1) produce pulses with characteristic time scales on the order of milliseconds and 2) maintain sufficient pressure difference between the ion source and main acceleration chamber.

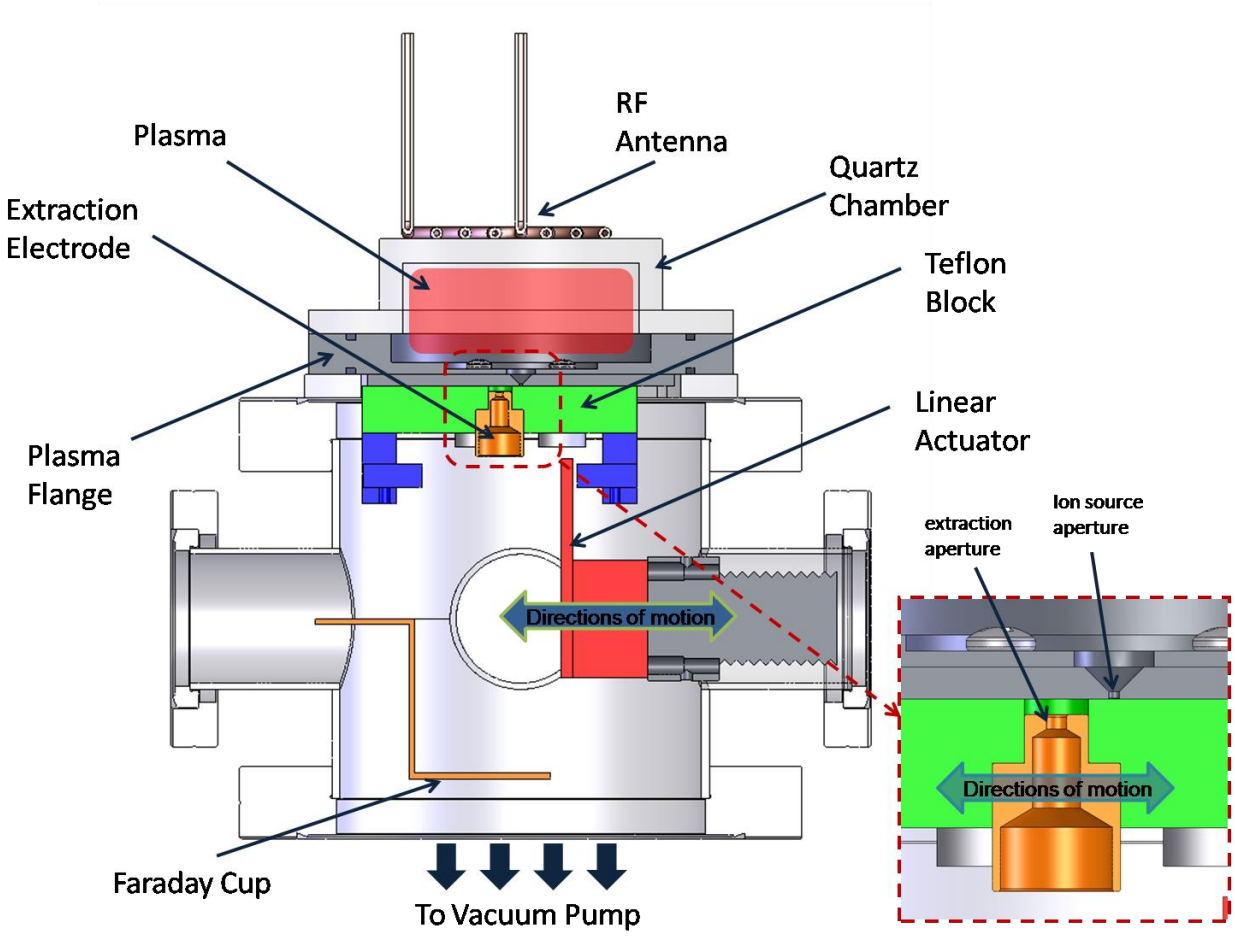

Figure 4.18: Schematic of the mechanical shutter system combined with an RF plasma ion source.

A schematic of the mechanical shutter is shown in Figure 4.18. Typically, the extraction electrodes are isolated from the ion source via insulating standoffs, but the shutter is designed to have the beam extraction electrode attached to a Teflon block that is pressed tightly against the ion source. The extraction assembly moves as an entire unit during ion beam pulse operation. At the "beam-off" position, the extraction aperture is slightly misaligned with the ion source aperture, preventing the extraction of ions. At the "beam-on" position, the extraction assembly is moved normal to the ion beam direction causing the extraction aperture and ion source aperture to become aligned momentarily so that ions can come out of the ion source. Further movement of the extraction assembly causes the extraction aperture to again become misaligned with the ion source aperture, which prevents ions from being extracted as before. Because the Teflon block is tightly pressed against the ion source flange, a vacuum seal is made between the ion source and acceleration chamber in the "beam-off" positions.

By controlling the motion of the extraction assembly, one has direct control of the temporal profile of the ion beam. Assuming a uniform plasma density across the ion source aperture and

the ion beam motion is normal to the aperture; the beam intensity during the pulse is related to the amount of overlap between the extraction aperture and the ion source aperture. Mathematically, the beam intensity, *I(x),* as a function of the extraction aperture position, *x,* is given by

$$I(x) = Re\left\{R_1^2\left[\frac{\pi}{2} - sin^{-1}\xi - \xi\sqrt{1-\xi^2}\right] + R_2^2\left[\frac{\pi}{2} + sin^{-1}\zeta + \zeta\sqrt{1-\zeta^2}\right]\right\} \quad (4.22)$$

$$\xi = \frac{R_1^2 - R_2^2 + x^2}{|2xR_1|}\zeta = \frac{R_1^2 - R_2^2 - x^2}{|2xR_2|} \quad (4.23)$$

WhereR_1 is the radius of the extraction aperture (1 mm in the present system) and $R_2$is the radius of the ion source aperture (= 0.5 mm). Note that$R_1 \geq R_2$ and the extraction aperture position, *x,* must be known as a function of time in order to map the beam profile in time.

The photo of the shutter system in Figure 4.19 shows a simple pneumatic actuator that is used to provide the linear motion of the extraction assembly for the beam pulsing operation. The actuator is a UHV compatible Huntington® Pneumatic Linear Positioner [52] controlled with a 4-way solenoid valve. The rapid flow of pressurized air either into or out of the actuator cylinders provides the fast motion of the extraction assembly. The maximum speed of the extraction assembly is limited by the maximum flow rate of the pressurized air. Using a high speed camera, it was determined that the actuator speed, *dx/dt,* is approximately constant at *1 m/s* during the pulse. Figure 4.20a shows that the beam pulse profile computed from Eqn. 3.22 has a characteristic time scale in the millisecond range and sub-millisecond pulsing time scales are possible.

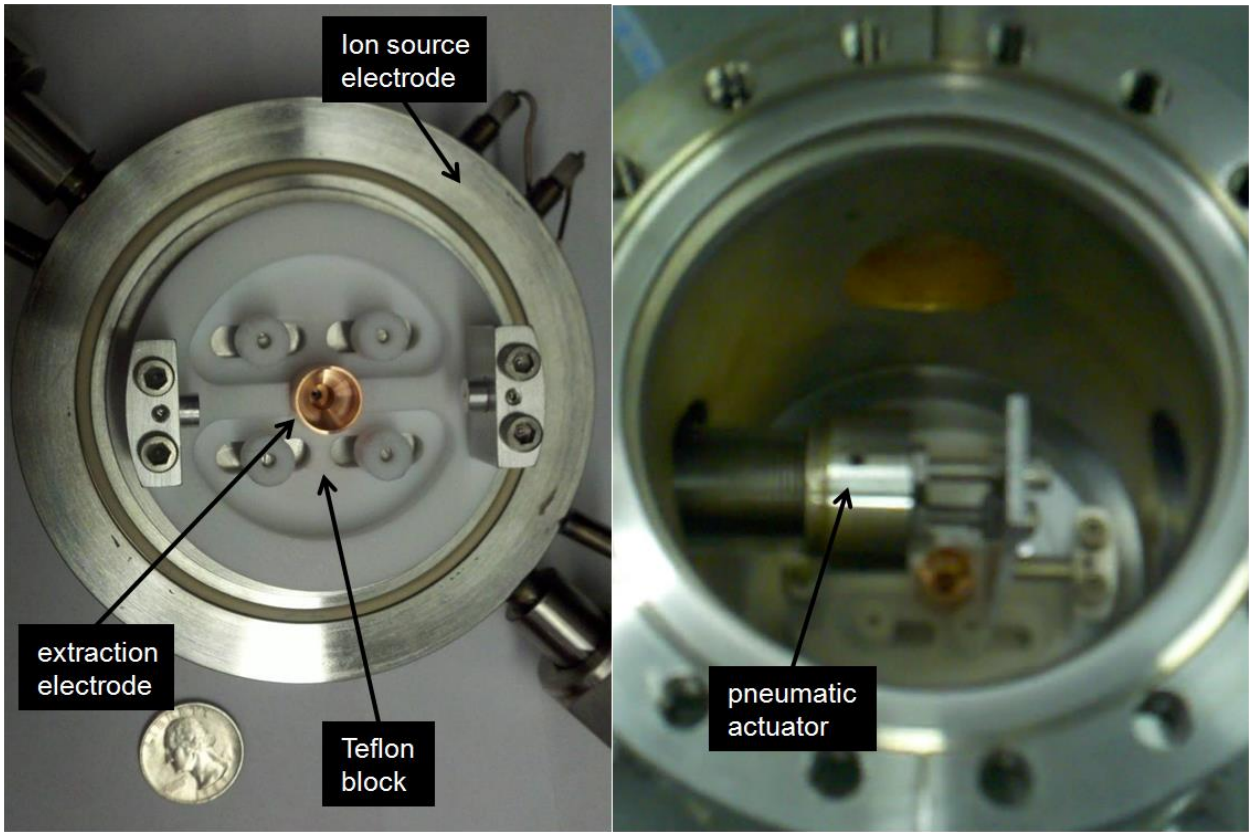

Figure 4.19: Photos showing the mechanical shutter hardware.

The shutter was tested by operating an RF-driven hydrogen plasma ion source in inductive coupled mode and recording the beam pulse profile of the extracted ions with a Faraday cup. After purging the system with hydrogen gas, the base pressure equilibrated around 6.0E-8 Torr using a 300 L/s Pfeiffer turbo-molecular pump [53]. With the extraction assembly in the closed position and ion source pressure of 1E-2 Torr, the pressure in the main acceleration chamber increased slightly to 6.1E-8 Torr. Because of the slow response time of the cold cathode vacuum gauge, it was not possible to measure the instantaneous pressure of the "beam-on" position during the pulse. Instead, the "beam-on" position was measured by manually moving the extraction assembly to the aligned position with the ion source aperture. At steady state, the pressure was 3.05E-7 Torr, which is an order of magnitude higher than in the closed position (see Table 4.3). The ion beam profile was measured using a Faraday cup placed approximately 10 cm away from the extraction electrode. The ion source potential was raised to +1 kV while the extraction electrode was maintained at ground potential. The temporal profile of the ion beam pulse was measured with a digital oscilloscope. From the beam profile trace, the FWHM of the beam was determined to be approximately 1.5 ms (Figure 4.20b). The rise and decay time of the beam pulse was approximately 1 ms, which is consistent with the analytical solution. There is some asymmetry in the flat-top portion of the measured beam profile caused most likely by variations in the local electric field at the extraction area.

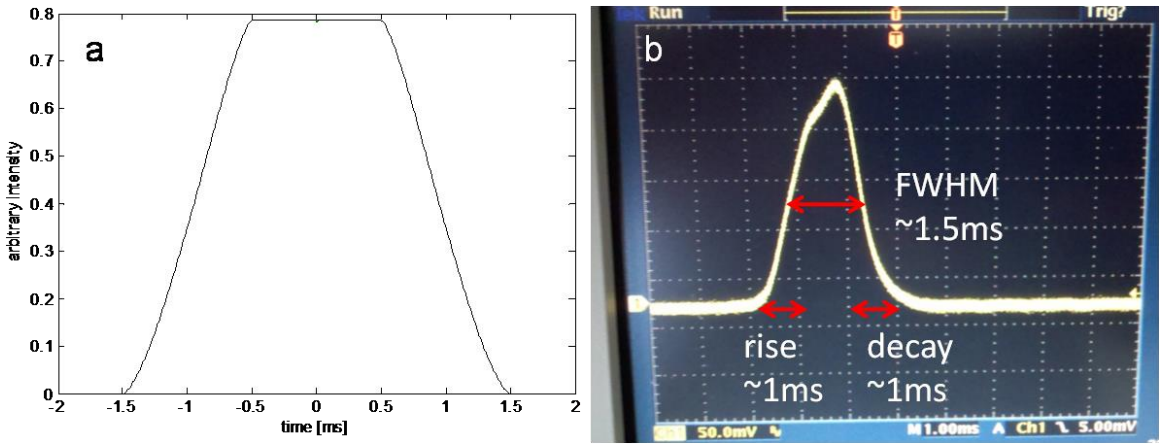

Figure 4.20: a) Analytical solution of the beam profile for the current geometry of extraction and ion source apertures. b) Oscilloscope trace of the beam profile measured with a Faraday cup during the operation of the shutter.

The data indicate that the shutter can produce ion beams with characteristic rise, decay and flat-top pulse widths on the order of 1 ms while maintaining excellent vacuum isolation between the ion source and the acceleration chamber. For applications requiring microsecond pulse-width beams, an electromagnetic actuator mechanism could boost the shutter speed and produce shorter pulses. To increase the beam current, multi-hole (beamlet) extraction can be implemented in the shutter for extracting high current pulsed beams (e.g., up to 0.5A could be extracted from a single ion source using approximately 100 beam apertures).

Table 4.3: Summary of the acceleration chamber pressure measurements for the "beam-on" and "beam-off" shutter positions for a 1-mm diameter ion source aperture.

Ion source pressure	1.00E-2 Torr
Base pressure	6.00E-8 Torr
"Beam-off" pressure	6.08E-8 Torr
"Beam-on" pressure	3.05E-7 Torr

The pulsed beam profile can be tailored for different applications by changing the shape/sizes of the extraction and ion source apertures. To achieve faster rise and decay times, one can replace the extraction aperture hole with a thin slit to produce a "flat-top" beam. During the rise and fall of the pulse, the shape of the beam produced by the translational shutter is not completely round as in the case of electric or magnetic beam sweeping systems. The effect of the asymmetric spatial beam profile for beam matching into secondary accelerators (such as linacs) would require further study. However, this will not produce any adverse issues in applications where the beam is not required to be injected into a secondary acceleration system.

5. High-Flux Neutron Generator

Development of high flux neutron generators (HFNG) aims to provide reactor level neutron fluxes in a compact system. Large-area-source neutron generators are currently being developed at Sandia National Laboratories (SNL-HFNG) and the Berkeley Geochronology Center (BGC-HFNG) for utilizing both fast and thermal neutron flux. These systems are designed to produce ~1000 times the yield of current commercial D-D neutron generators by pushing the heat flux limits on the target to maximize "neutrons per watt" of input electrical energy. For the first time, these HFNG systems will make practical a new alternative for applications requiring reactor level fluxes and uniformity, ultimately reducing the dependence on reactors.

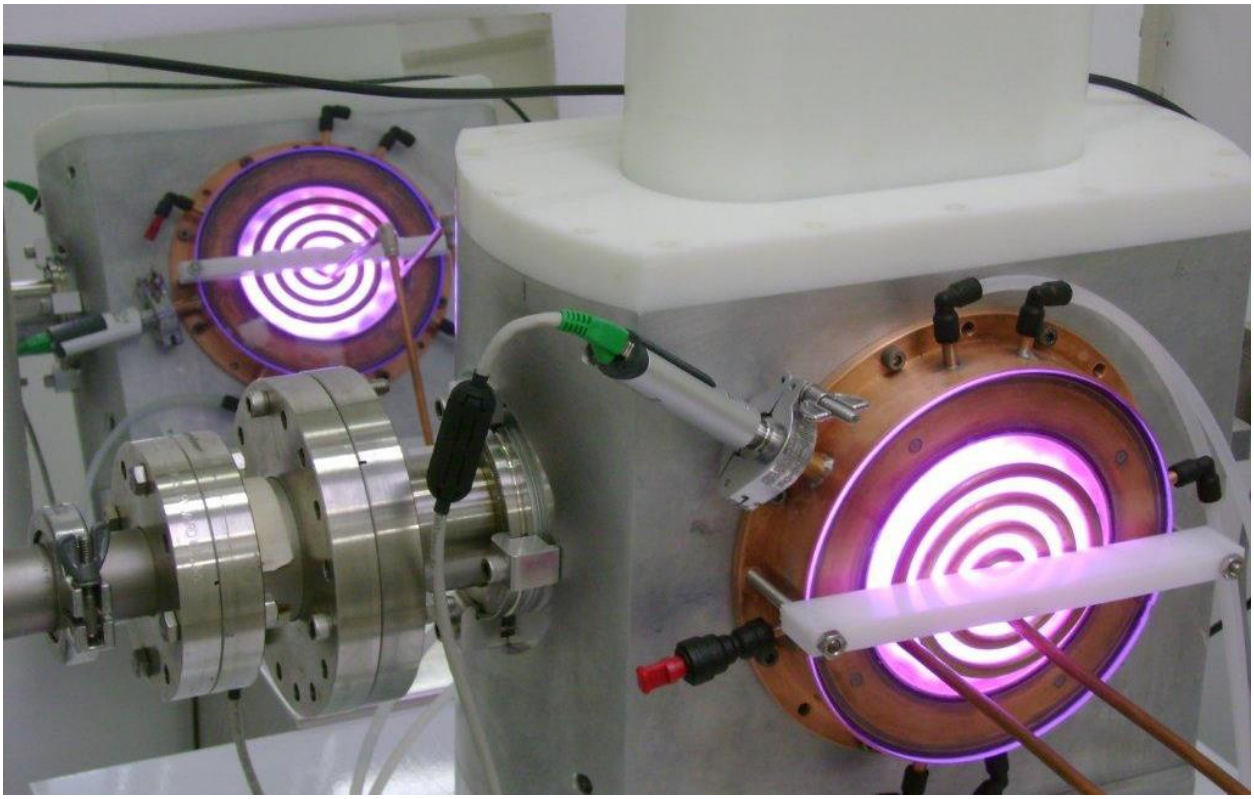

Figure 5.1: Inductive plasma discharge from the BGC-HFNG

I. Applications

a. 39Ar/40Ar Dating Technique

Until recently, geological dating techniques that employ neutron irradiation of the samples, such as the $^{40}Ar/^{39}Ar$ method, were thought to be possible only at a nuclear reactor due to the high

neutron fluence requirement. In the $^{40}Ar/^{39}Ar$ dating technique, fast (> 1 MeV energy) neutron fluence irradiation on the order of > 1E16 n/cm^2 are required to attain acceptable levels of ^{39}Ar from the $^{39}K(n,p)^{39}Ar$ reaction [4]. In a reactor operating at fluxes of order ~1E13 n cm^{-2} s^{-1}, this fluence can be obtained within one hour of reactor neutron irradiation. Commercial D-D neutron generators with typical output of 1E7 n/cm^2/s [54] will require about 31 years to reach the minimum fluence irradiation requirement, rendering the concept impractical.

b. **Boron Neutron Capture Therapy (BNCT)**

Boron neutron capture therapy (BNCT) is one of the most promising methods for non-invasive treatment of deep seated liver and brain tumors. In a typical BNCT treatment, the patient is injected with a drug containing a high boron content, which preferentially attaches to tumor cells. A high dose of epithermal neutrons (0.1eV – 20keV) is then delivered to the patient to induce boron capture reactions within the tumor cells according to

$$^{10}_{5}B + ^{1}_{0}n \longrightarrow ^{7}_{3}Li + ^{4}_{2}He + 2.31MeV \qquad (3.24)$$

The recoil range of the ^{7}Li and ^{4}He nucleus is approximately 3.5 and 7.5 μm respectively [55], thus the lethality of this method is limited to the cell containing the boron capture reaction. With recent advancement in tumor drug research, the boron concentration ratio between tumor and healthy cells can be as high as 11:1 [56]. Current BNCT treatments are being conducted only in nuclear reactors due to the high neutron flux (> 5E8 epithermal n cm^{-2}) requirement [12] [57]. However, it is advantageous to develop electronic neutrons sources that are more compact and suitable for in-hospital treatments.

I. Neutron Flux Profile

The designed maximum yield of the currently studied HFNGs are on the order of 10^{11} n/s (SNL-HFNG) and $3 \cdot 10^{11}$ n/s (BGC-HFNG) of D-D neutrons over a total cross-section area of ~40 cm^2. The goal is to achieve at least three orders of magnitude higher yield than current state-of-the-art commercial neutron generators. The current design is significantly different from traditional point source design in that neutrons are generated over a large area to maximize heat transfer away from the target. The axial $\phi(R)$ and lateral $\phi(t)$ neutron flux for a large area disk source is given by (Eq. 4.2), which must be solved by numerical integration. At the centerline of the disk source, the flux can be expressed simply by (Eq. 4.3) [58]

$$\phi(R,t) = \frac{Y}{2\pi} r_0 \int_{-1}^{1} \frac{dx}{\sqrt{R^2 + (t + r_0 x)^2}} tan^{-1} \frac{r_0\sqrt{1-x^2}}{\sqrt{R^2 + (t + r_0 x)^2}} \qquad (5.2)$$

$$\phi(R,0) = \frac{Y}{4\pi r_0^2} ln \frac{R^2 + r_0^2}{R^2} \qquad (5.3)$$

where ϕ is the flux of neutrons (n cm^{-2}), Y is the neutron yield in (n s^{-1}), r_0 is the equivalent radius of a disk source (cm), R is the distance along the centerline axis away from the disk (cm), and t is the transverse distance from the centerline (cm). In order to maximum the flux, the samples should be put as near the neutron source as possible (minimize R). Figure 5.2 shows a cross-section view of the BGC neutron target. The deuteron beams are extracted from two oppositely directed ion sources on the top and bottom and bombard the V-grooves of the target. The irradiation sample for the BGC application is placed in the middle of the target to receive the maximum amount of fast neutron flux. In order to generate a uniform "large-area" source, 558 beams are extracted from each ion source. MCNP5 [23] was used to model the neutron flux in the sample area. Result of the flux distribution is shown on Figure 5.3. As seen in the lineout plots, the uniformity is much better across the y-axis compared to the x-axis. Because the V-grooves are cut vertically, the water channels (which are good neutron scatterers) are also aligned vertically. This causes each outer column of beam away from the center column to contribute less to the center region. As a result, we see a greater fall off of the flux in the x-axis line out.

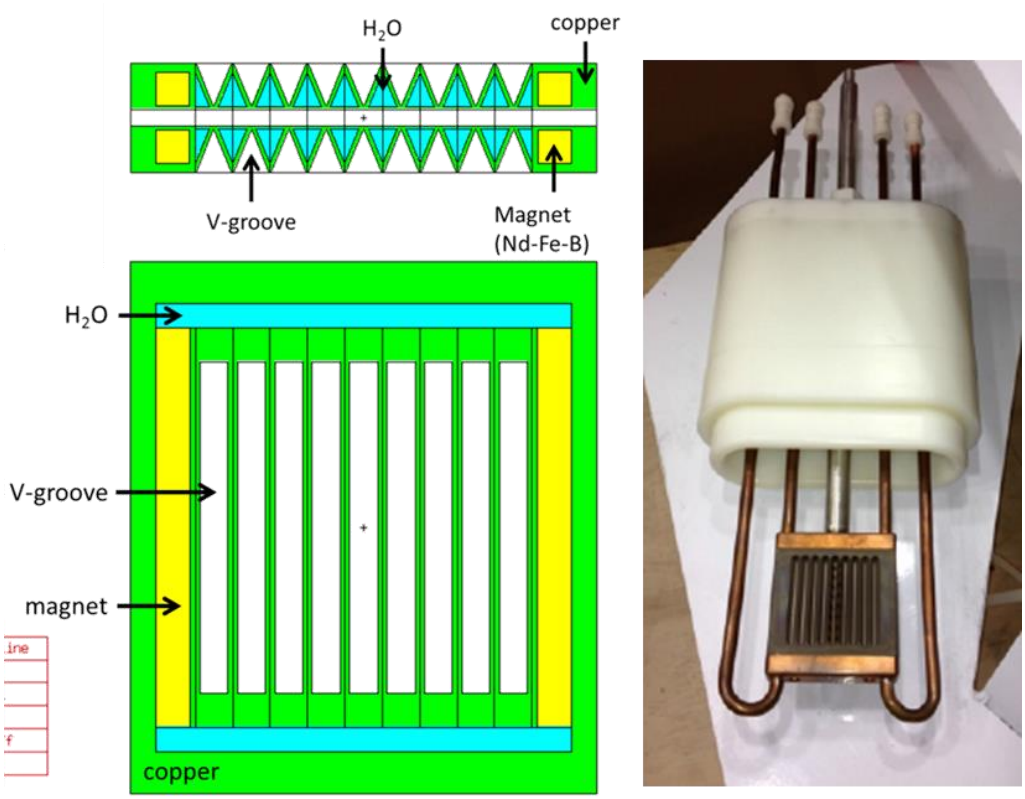

Figure 5.2: Section views of the BGC-HFNG target modeled with MCNP5 (left). Actual target (right).

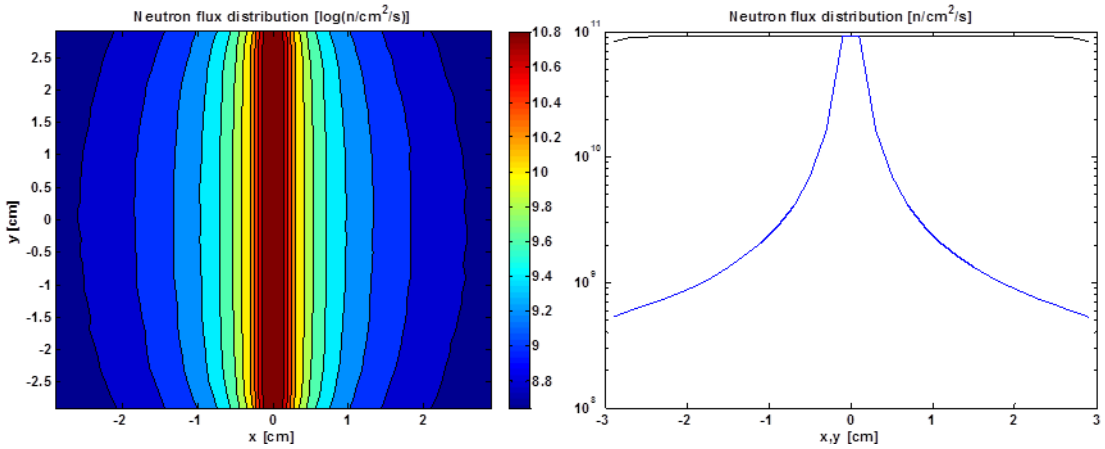

Figure 5.3: Neutron flux distribution of the BGC-HFNG in the sample slot area is shown on the left. Line out plots of the x-axis (blue) and y-axis (black) are shown on the right.

II. Thermal Analysis of the Beam Loaded Target

A specially designed copper target coated with titanium is used to facilitate the D-D beam loaded reactions while dissipating the heat load. For the BGC-HFNG, the deuteron beams hit the angled surfaces of a titanium coated target in order to reduce the incident heat flux on the surface. Assuming operation at 120kV of acceleration voltage, current of ~1A is required for 3E11 n/s yield. The average heat flux on the target is approximately given by

$$q''_{avg} = \frac{V \cdot I}{n_i \pi r_i^2} \sin\theta_g \qquad (5.4)$$

where V*I is the total ion beam power on the target, n_i is the number of ion beams (1116), r_i is the radius of each ion beam at the target (1 mm), and θ_g is the angle of the V-groove with respect to the vertical (22.5°). The average heat flux evaluated from equation 5.4 is approximately 1300 W/cm^2. There are a total of 18 triangular shaped water channels water cooling channels to provide cooling to the ion bombarded surfaces, which were prepared by electrical discharge machining (EDM). The thickness of copper between the heated surface and water is approximately 0.8 mm, which would produce a temperature differential of ~26°C between the wetted channel wall surface (T_w) and the outer heated surface (T_s). The most important criteria for the channel wall surface is to ensure that departure from nucleate boiling (DNB) does not occur, which requires the average heat flux, q''_{avg} to not exceed the critical heat flux, q''_{crit} . For sub-cooled flow ($x_{out} < 0$), the critical heat flux is given by [59]

$$q''_{crit} = \frac{CGh_{lv}}{\sqrt{Re}} \qquad x_{out} < 0 \qquad (5.5)$$

$$C = (0.216 + 0.0474P)\psi \tag{5.6}$$

$$\psi = \begin{cases} 1, & x_{out} \leq -0.1 \\ 0.825 + 0.986 \cdot x_{out}, & 0 > x_{out} > -0.1 \end{cases} \tag{5.7}$$

$$Re = \frac{GD_h}{\mu_l} \tag{5.8}$$

$$G = \rho V_l \tag{5.9}$$

$$x_{out} = \frac{c_{pl}\left(T_{l,out} - T_{l,out,sat}\right)}{h_{lv}} \tag{5.10}$$

$$T_{l,out} = T_{l,in} + \frac{sin\theta}{GA_c c_{pl}} \frac{V \cdot I}{18} \tag{5.11}$$

$$A_c = \frac{1}{4} b^2 tan\theta \tag{5.12}$$

where x_{out} is the outlet quality, P is the pressure (MPa), h_{lv} is the vaporization enthalpy (J kg^{-1}), Re is the Reynold's number, D_h is the hydraulic diameter (m), μ_l is the viscosity (Pa s), ρ is the fluid density (kg m^{-3}), V_l is the bulk liquid velocity (m s^{-1}), T_l is the bulk fluid temperature (^{o}C), T_{sat} is the saturated temperature at P, b is the base length of the triangular channel, and A_c is the channel cross-sectional area. Because the exit quality is negative, the bulk outlet fluid is still in the sub-cooled state. This will enable the use of regular heat exchangers and pumps designed for single phase operation without having to use costly condensers. It is crucial to maintain nucleate boiling throughout the channels in order to sustain a large heat transfer coefficient between Tw and $T_{l,sat}$, (wall superheat) which can be approximated by one of many heat nucleate pool boiling correlations. One of which is given by Borishansky [60]

$$q''_{avg} = (A^*)^{3.33}\left[T_w - T_{l,sat}\right]^{3.33}[F(P_r)]^{3.33} \tag{5.13}$$

$$A^* = 0.1011 P_c^{0.69} \tag{5.14}$$

$$F(P_r) = 1.8P_r^{0.17} + 4P_r^{1.2} + 10P_r^{10} \tag{5.15}$$

$$P_r = P_l/P_c \tag{5.16}$$

where P_l, P_r and P_c are the liquid pressure, reduced pressure and critical point pressure respectively measured in (bar). Equation 5.11 indicates that in the nucleate boiling regime, $q''_{avg} \propto \left(T_w - T_{l,sat}\right)^{3.33}$, which scales much better than the case of single phase convection, where $q''_{avg} \propto \left(T_w - T_{l,sat}\right)$. A contour plot of the wall superheat vs. fluid pressure and average heat flux is plotted in Figure 5.4. Note that in order for the analysis to be valid, both $x_{out} < 0$ and $q''_{avg} < q''_{crit}$ must be valid throughout the channel. In addition, the pressure along the channel also varies due to frictional and gravimetric losses, which in turn affects the state variables (μ_l, T_{sat}, etc.) Using z as the length parameter along the flow channel, the state variables can be written as a function of z. The pressure along the tube is given by

$$P(z) = P(0) - \rho(z)g\int_0^z \left(1 + \frac{f(z)\cdot V_l^2}{2D_H}\right)dz \tag{5.17}$$

where f is the Moody friction factor that depends on the pipe smoothness, ε, g is the gravitational constant and $P(0)$ is the initial pressure. f can be evaluated using the Swamee-Jain solution:

$$f(z) = \left[-2\,log_{10}\left(\frac{\varepsilon}{3.7D_h} + \frac{5.74}{\{Re(z)\}^{0.9}}\right)\right]^{-2} \tag{5.18}$$

Equations 5.5-5.11 can be written as

$$q''_{crit}(z) = \frac{C(z)G(z)h_{lv}(z)}{\sqrt{Re(z)}} \tag{5.19}$$

$$C(z) = (0.216 + 0.0474P(z))\psi(z) \tag{5.20}$$

$$\psi = \begin{cases} 1, & x(z) \le -0.1 \\ 0.825 + 0.986\cdot x(z), & 0 > x(z) > -0.1 \end{cases} \tag{5.21}$$

$$Re(z) = \frac{G(z)D_h}{\mu_l(z)} \tag{5.22}$$

$$G(z) = \rho(z)V_l \tag{5.23}$$

$$x(z) = \frac{c_{pl}(z) \cdot \left(T_l(z) - T_{l,sat}(z)\right)}{h_{lv}(z)} \tag{5.24}$$

$$dT_l(z) = \frac{sin\theta}{GA_c c_{pl}} \frac{V \cdot I}{18} dz \tag{5.25}$$

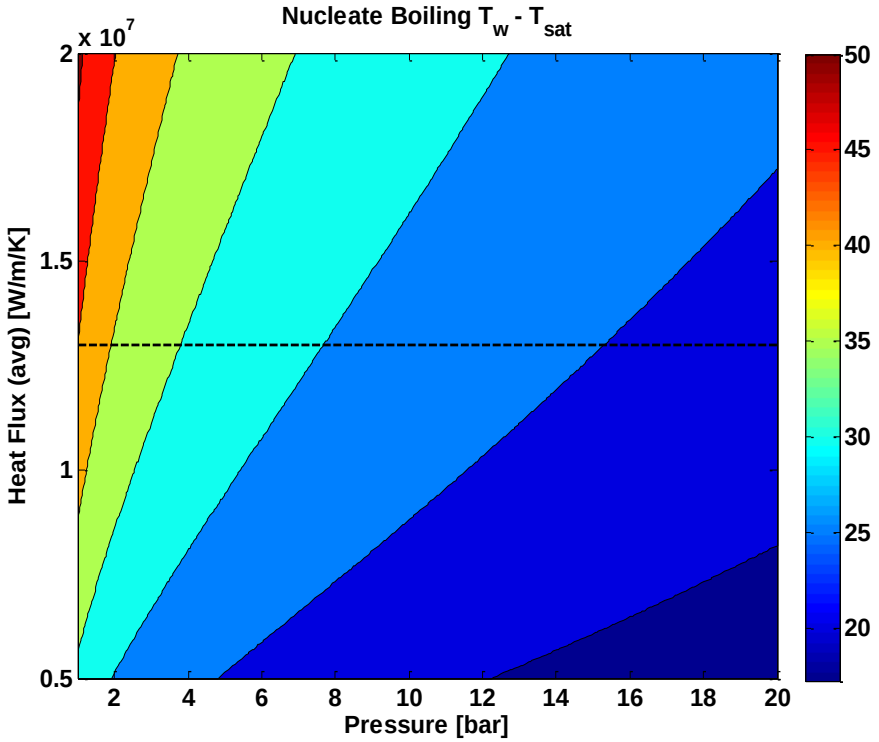

Figure 5.4: Nucleate Boiling superheat as a function of pressure and heat flux. Dashed line indicates heat flux of 1300 W/cm^2

For an inlet water temperature of 30^{o}C, results of the analysis are sown in Figure 5.5, where the locus of points (P,V_l) satisfying $q''_{avg} = q''_{crit}$ and $x_{out} < 0$ are plotted for different total power levels. For operating the HFNG, any point above and to the right of the locus of points (representing $q''_{avg} < q''_{crit}$) should satisfy the cooling requirement. Figure 5.6 shows the average target surface temperature as a function of pressure.

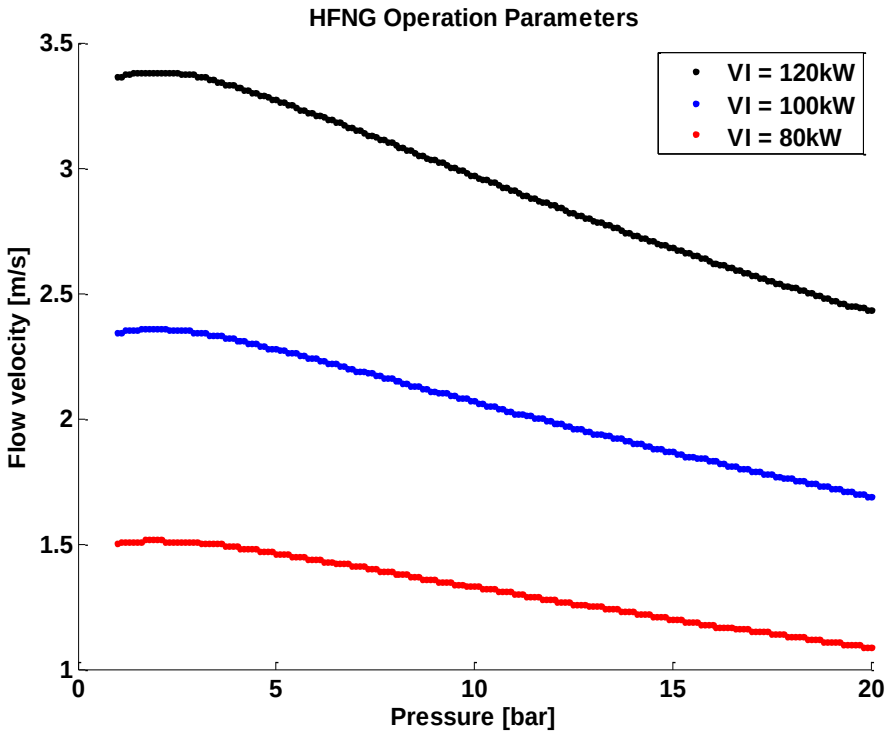

Figure 5.5: Minimum operating parameters for different power levels.

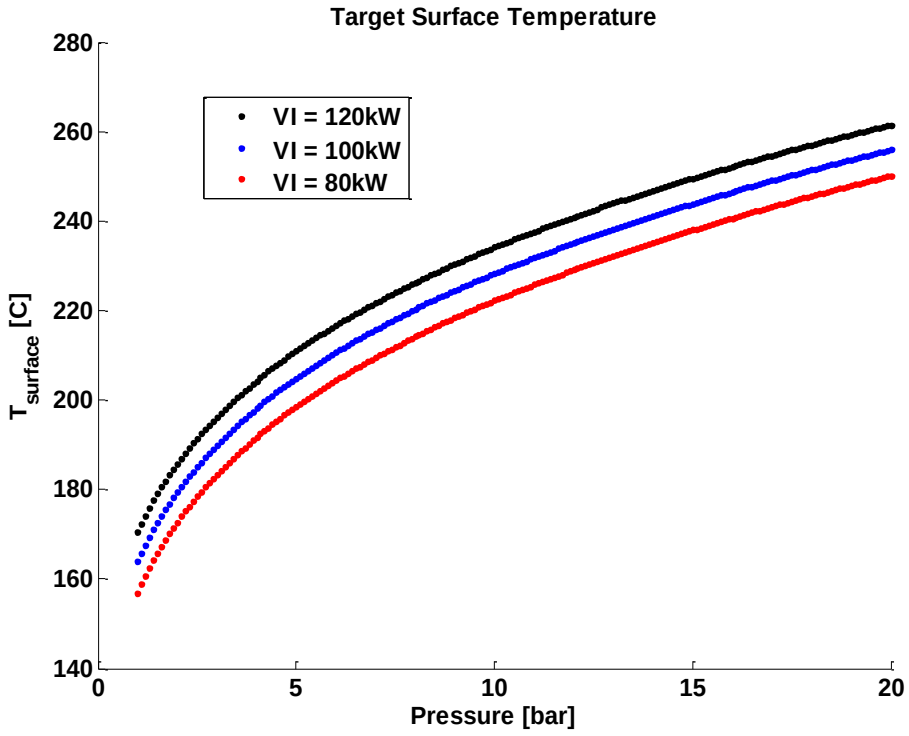

Figure 5.6: Target surface temperature as a function of pressure.

III. Neutron Moderator

Only mono-energetic fast neutrons at 2.45MeV are produced via the D-D reaction in the HFNG. Depending on the application, maximizing the neutrons flux at a different (lower) energy might be desired. For example, compensated-porosity well-logging (CNL) and neutron radiography both require thermal neutrons to maximize the detector count rate. On the other hand, BNCT requires moderation of neutrons to epithermal energies between 0.1eV – 20keV to maximize patient dose delivery. Furthermore, in certain gamma- or fast neutron-sensitive applications, an additional constraint might be to minimize the gamma or fast neutron dose on the detector or patient. Therefore, careful choice of the moderator material and geometrical configuration is crucial.

The primary mechanism fast for neutron moderation is through elastic scattering with the nucleus of the moderating materials. It can be shown through conservation of energy that the probability of the neutron to scatter isotropically from energy E_1 to E_2 is constant, and E_2 takes on values between αE_1 to E_1 such that [1]

$$\alpha = \left(\frac{A-1}{A+1}\right)^2 \tag{5.26}$$

where A is the mass of the scattering nucleus. This equation indicates that low atomic mass material are more efficient neutron moderators. In fact, it can be shown that the number of scatter events required to slow down a neutron from energy E1 to E2 is given by:

$$n = \frac{1}{\xi} ln\left(\frac{E_1}{E_2}\right) \tag{5.27}$$

$$\xi = 1 + \frac{\alpha}{1-\alpha} ln\, \alpha \tag{5.28}$$

where n is the average number of collisions needed to moderate neutrons from energy E_1 to E_2, and ξ is the log energy decrement. For a mixture involving different elements, the scattering cross-section must be taken into account, yielding an average log energy decrement defined by

$$\bar{\xi} \sum S_{s,i} = \sum \left(S_{s,i} \xi_i\right) \tag{5.29}$$

where $S_{s,i}$ is the average macroscopic scattering cross-section of isotope *i* in the energy range from E_1 to E_2. The quantity $\bar{\xi} \sum \left(S_{s,i}\right)$ is the moderating power of the material. The moderating ratio, ε, is a measure of the effectiveness of the moderator material to slow neutrons and depends inversely on the absorption cross-section, S_a, of the material:

$$\varepsilon = \frac{\bar{\xi} \sum S_{s,i}}{\sum (S_{a,i})} \tag{5.30}$$

Table 5.1 shows a list of common materials used for thermal and epithermal moderation [61].

Table 5.1: Moderating power and moderating ratio of common low-Z neutron moderator materials

Moderator	Moderating Power (1 eV to 100 keV)	Moderating Ratio (Approximate)
Water	1.28	58
Heavy Water	0.18	21 000
Helium at STP	0.00001	45
Beryllium	0.16	130
Graphite	0.064	200
Polyethylene (CH_2)	3.26	122

Because of the lower atomic mass of hydrogen in light water (H_2O), the moderating power of H_2O is about seven times higher than heavy water (D_2O). However, the absorption cross-section of deuterium is about three orders of magnitude lower than hydrogen, making D_2O the more effective moderating material.

a. **Thermal neutron moderator**

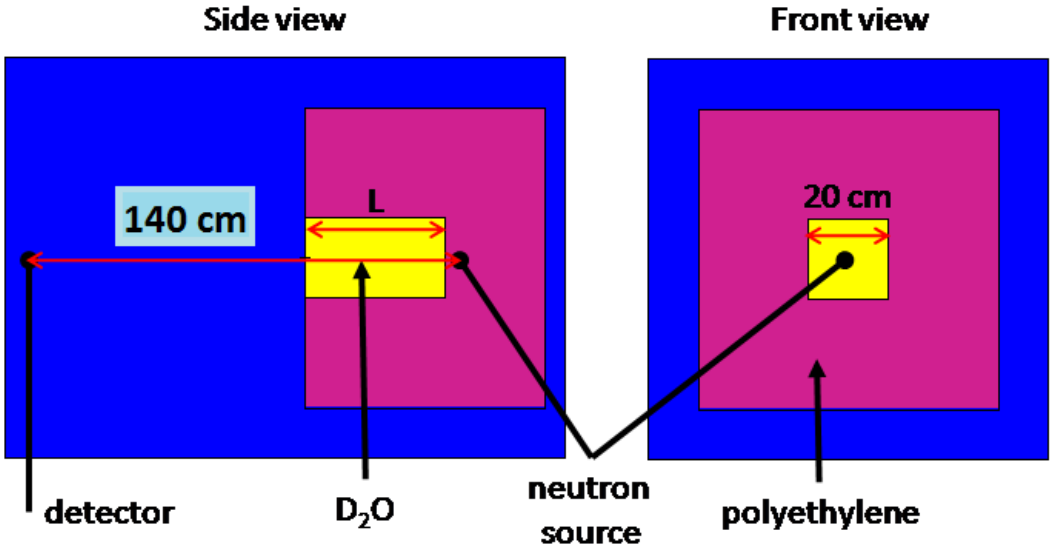

Figure 5.7: Thermal neutron moderator geometry used in MCNP model.

In the previous section, it was shown that D_2O was a more effective moderating material than H_2O. Maximizing the thermal neutron flux requires determining the optimal thickness of heavy water moderator to convert 2.45MeV D-D neutrons into thermal neutrons. Monte-Carlo

computations were performed to characterize the thermal and fast neutron flux for different length moderators in the existing geometry and configuration of the HFNG (Figure 5.7). Results of the computation are shown in Figure 5.8. The thermal neutron flux was found to reach a maximum of 3.10E-6 n/cm^2/s per source particle with the existing shielding and a heavy water moderator length of 6 cm. The thermal neutron to total neutron ratio was found to increase rapidly below 15 cm and reach an asymptotic value between ~0.85 to 0.9. If radiography requires a high thermal neutron to fast neutron flux fraction, then it is recommended to use a heavy water moderator thickness of approximately 15 cm; on the other hand, if the requirement is to have the highest thermal neutron flux, then a 6 cm thick heavy water moderator is a better choice.

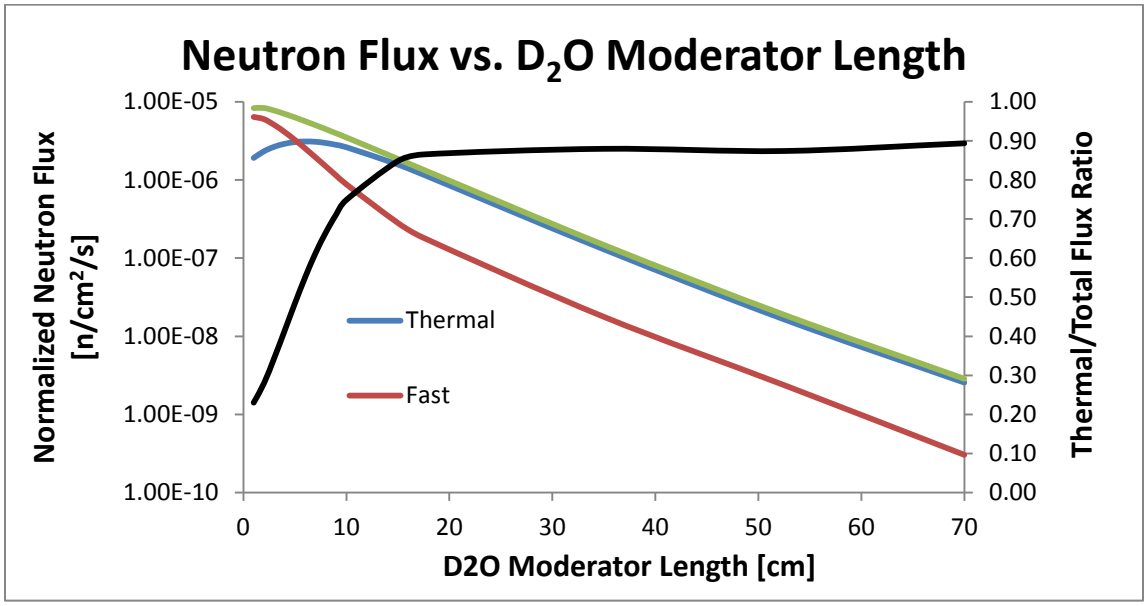

Figure 5.8: Neutron flux computational results from MCNP.

To verify the computational model, the signal from a He-3 detector located at 140 cm from the neutron source (32 mCi AmBe source) was measured. Different moderator lengths and materials were used, and the results are summarized in Table 5.2.

Table 5.2: Measured neutron count rates from light and heavy water moderators using a 32 mCi AmBe isotropic neutron source. Units are in counts per second measured by the MCA.

Moderator Thickness	H_2O	D_2O	Fast
0 cm	8.93	8.93	1.55
17.5 cm	4.14	5.48	0
35 cm	2.67	3.45	0

b. **Epithermal neutron moderator**

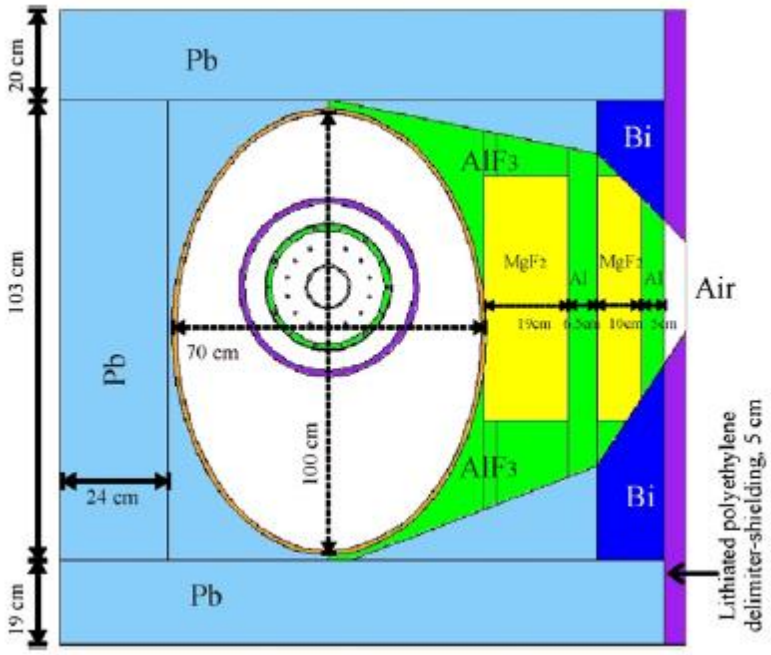

Figure 5.9: BNCT moderator design for a previous HFNG

For BNCT applications using a compact high flux neutron generator, the moderator design is critical to minimize the treatment time and unwanted radiation dose to the patient. Typically, neutrons with energy between 0.1eV and 20keV are used for treating deep seated brain and liver tumors. Durisi *et. Al.* [12] have previously designed a moderator for a co-axial type D-D neutron generator (Figure 5.9) The design used lead as a neutron reflector and gamma shield, bismuth for reflector and collimator, and a combination of AlF_3 and MgF_2 for the moderation. The exit plane is lined with a lithiated-polyethylene ($^7Li\text{-}CH_{2n}$) as an effective thermal neutron absorber. Fluental ($[Al]_{0.3}$-$[AlF_3]_{0.69}$-[LiF]0.01 mixture) was also analyzed in place of MgF_2 for the moderator which showed higher average neutron flux but at the expense of more high energy neutrons (> 20keV).

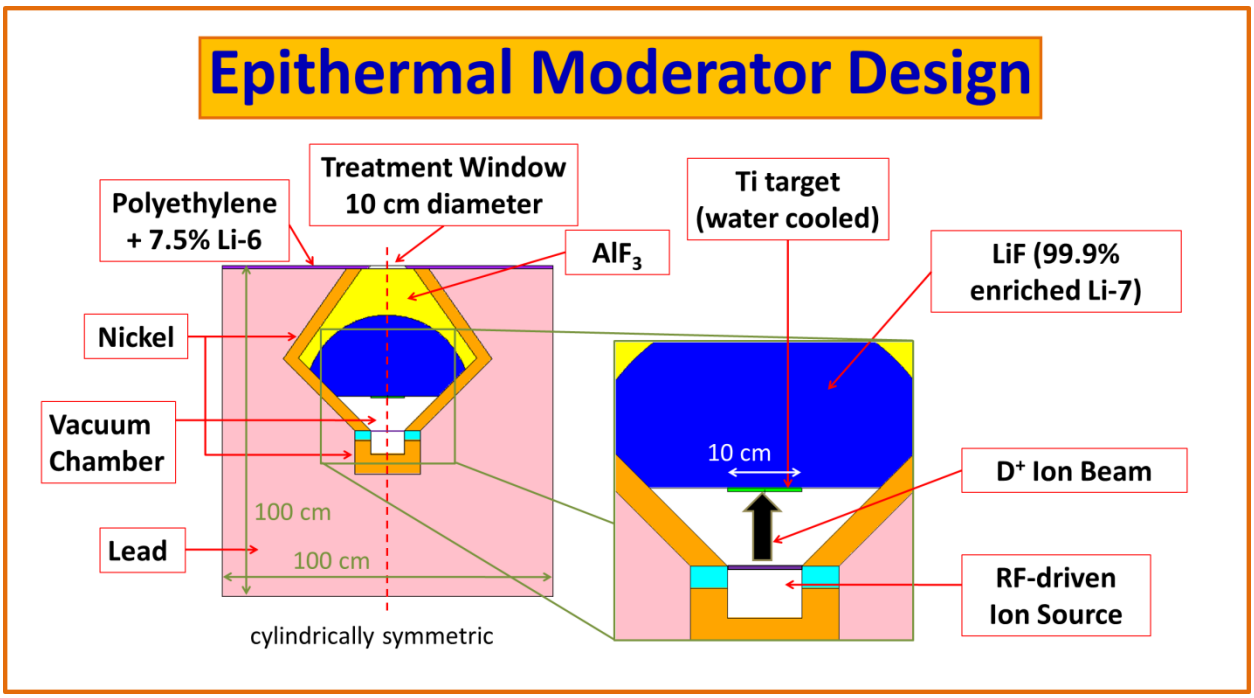

Figure 5.10: Epithermal neutron moderator design for an axial-type D-D HFNG.

It was found that the previous HFNG used for the modeling was not ideal for the BNCT application. The co-axial design generated neutrons in a sparse cylindrical surface that is about 35 cm in diameter. As a result, neutrons at the back-end contribute less flux compared to neutrons at the front end. A neutron moderator was designed [62] (Figure 5.10) for use with an axial type HFNG (SNL-HFNG), which is similar to the BGC-HFNG except only one ion source module is operated. The primary moderator material is enriched ^{7}LiF because ^{6}Li has a very high (n,^{3}H) cross-section which acts to poison the neutron flux. Several radii of ^{7}LiF were tested with the rest of the moderating chamber filled with AlF_3. Similar to Durisi's design, leaded blocks were used for gamma shielding. A layer of nickel was used as the neutron reflector to increase the epithermal flux at the patient's location (treatment window). Nickel was found to be a very effective neutron reflector, which is widely used as neutron guide tubes in reactors [63]. Using MCNP5, the calculated average epithermal neutron flux at the treatment window was >1E8 n/cm^2/s after accounting for the anisotropy of the D-D reaction. This value is almost one order of magnitude higher than previous results.

Table 5.3: MCNP5 results of the new epithermal moderator design.

Parameters[1]	previous result[1]	present result	Statistical Error (%)	Recommend Value[1]
$\Phi_{epithermal}$ (n/cm²s)	1.23E7	1.01E8	0.39	> 5E8
$J_{epithermal}$ (n/cm²s)	7.52E6	6.27E7	0.30	> 3.5E8
D_{fast}/Φ_{epi} (Gy*cm²)	1.82E-12	3.93E-13	2.67	< 2E-13
D_{gamma}/Φ_{epi} (Gy*cm²)	2.98E-13	8.29E-13	1.75	< 2E-13
J_{epi}/Φ_{epi}	0.61	0.60	---	> 0.70

[1] Parameters, previous result, and recommend value were taken from E. Durisi et. al.

The neutron energy spectrum at the treatment window is shown in Figure 5.11. Compared with Durisi's Fluental moderator results, the high energy peak between 1.1 - 1.3 MeV is significantly lower. In the present configuration, about 89% of the neutrons are within epithermal energies while 7.5% of the total are fast neutrons and 3.5% are thermal neutrons. The D_{fast}/Φ_{epi} ratio is lower than the previous result indicating lower unwanted fast neutron dose on the patient, the D_{gamma}/Φ_{epi} is higher, indicating higher gamma dose contribution. Further optimization of the geometry is needed to lower the total dose per epithermal neutron flux on the patient while maintaining the high epithermal flux needed for practical treatment time.

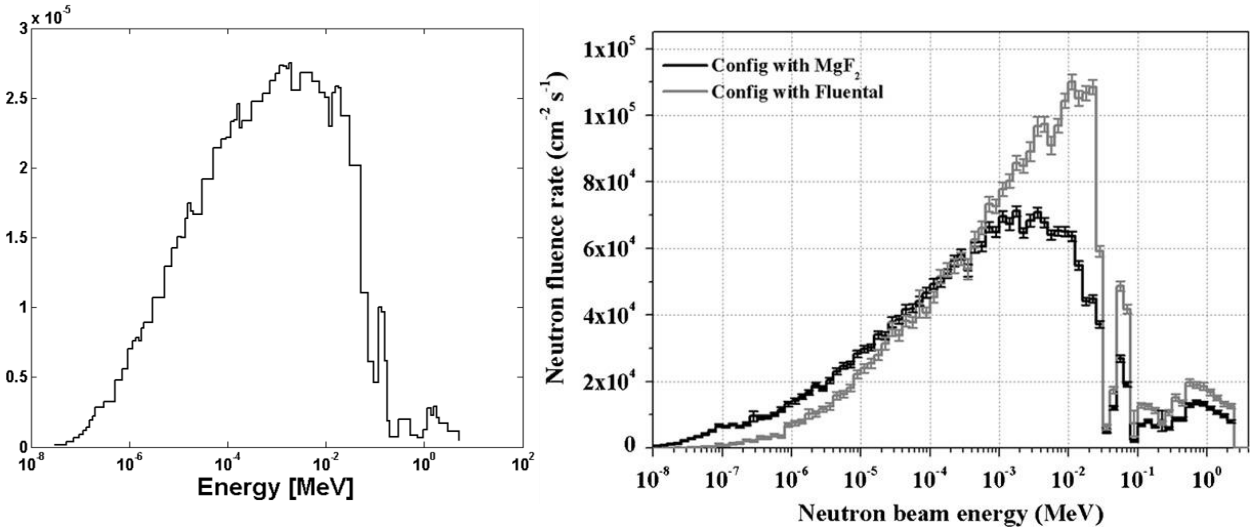

Figure 5.11: Neutron energy spectrum at the treatment window. (left) current results, (right) previous results.

IV. Radiological Material Activation

The high flux D-D neutron generators are unique compared with other high flux neutron sources that use D-T or spallation neutrons in that the maximum neutron energy from the D-D reaction is 2.5 MeV. This energy is often too low to induce significant production for some threshold (n,p) and (n,α) reactions. For example, the $^{63}Cu(n,\alpha)^{60}Co$ cross-section is ~1 μb at 2.5 MeV versus ~50 mb at 14 MeV. To assess the radiological concerns of the high flux neutron generator, a list of IAEA nuclides of concern were compiled and MCNP calculations performed to predict the steady state amounts that would be produced. The steady state activity is defined as the maximum activity of the radionuclide that can be produced assuming the neutron generator has been running for a long time ($t_{on} \rightarrow \infty$), which is simply equal to the production rate of the particular radionuclide

$$A_{steady} = R = \int_0^{E_{max}} N_0 \sigma(E) \phi_n(E) dE \tag{5.31}$$

where N_0 is the total amount of parent material, σ is the cross-section for the radiological nuclide production (cm^2), and ϕ_n is the average neutron flux in the material (n cm^{-2} s^{-1}). It's important to minimize A_{steady} of long lived (half-life ≥ 1 yr) radionuclides because these will be remain hazardous for a long time. For this reason, most components (especially vacuum components) were made with aluminum instead of stainless steel. For example, the (n,γ) capture on ^{27}Al creates ^{28}Al, (half-life of 2.24 minutes), while iron and stainless steels can produce radionuclides with half-lives as long as 312 days (^{54}Mn). Table x shows a list of accountable radionuclides produced in the steady-state.

Table 5.4: List of accountable radionuclides in accordance with the IAEA Basic Safety Standards

HFNG Component	Parent Isotope	Radioactive Isotope	Steady State Activity [Bq]	Exempt Level[Bq]
target	Cu-63	Cu-64	5.48E+08	1.00E+06
	Cu-63	Co-60	1.01E+04	1.00E+05
	Cu-63	Ni-63	2.96E+08	1.00E+08
	Cu-65	Ni-65	3.63E+03	1.00E+06
target magnets	Fe-54	Fe-55	1.28E+06	1.00E+06
	Fe-54	Mn-54	2.34E+06	1.00E+06
	Fe-58	Fe-59	3.36E+04	1.00E+06
	Nd-142	Ce-139	3.38E+02	1.00E+06
	Nd-143	Pr-143	1.02E-01	1.00E+06
	Nd-144	Ce-141	6.47E+02	1.00E+07
	Nd-146	Ce-143	2.68E+01	1.00E+06
ion source	Cu-63	Cu-64	6.98E+09	1.00E+06

	Cu-63	Co-60	9.68E+03	1.00E+05
	Cu-63	Ni-63	3.06E+08	1.00E+08
	Cu-66	Ni-65	3.27E+03	1.00E+06
extraction plate	Mo-98	Mo-99	5.59E+07	1.00E+06
	Mo-98	Zr-95	3.65E+01	1.00E+06
source magnets	Fe-54	Fe-55	7.26E+06	1.00E+06
	Fe-54	Mn-54	4.74E+06	1.00E+06
	Fe-58	Fe-59	2.32E+05	1.00E+06
	Nd-142	Ce-139	7.04E+02	1.00E+06
	Nd-143	Pr-143	2.03E-01	1.00E+06
	Nd-144	Ce-141	1.40E+03	1.00E+07
	Nd-146	Ce-143	5.55E+01	1.00E+06
Quartz Plate	Si-30	Si-31	4.65E+04	1.00E+06
Air	Ar-36	Ar-37	2.30E+05	1.00E+08
	Ar-36	Cl-36	1.29E+03	1.00E+06
	Ar-40	Ar-41	8.72E+06	1.00E+09

V. Neutron Source Calibration

The absolute neutron yield of the HFNG is calibrated using the well-established gold foil (Au-197) activation and Nickel (^{58}Ni) activation method. In the gold foil activation experiment, a gold foil sample was placed 50 cm away from the target inside a cadmium shielded paraffin cup (Figure 5.12). Neutrons emitted from the HFNG thermalize and activates ^{197}Au to produce ^{198}Au, which decays by β- emission with a half-life of 66 hours.

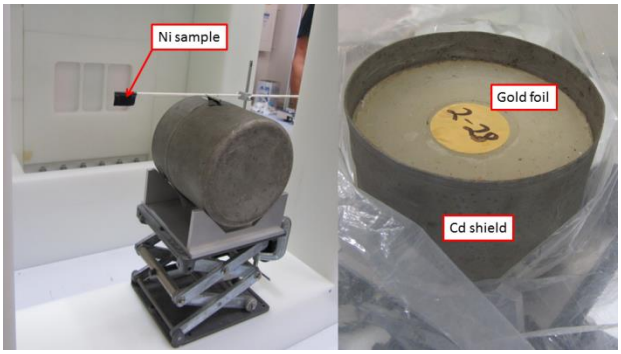

Figure 5.12: Calibration experiments using gold foil and nickel activation to determine absolute yield of the HFNG.

The HFNG was operated for ten minutes to obtain enough Au-198 for analysis. The 412 keV gamma ray associated with the decay were counted using a calibrated HPGe detector at

Lawrence Berkeley National Lab (LBNL) to infer the neutron yield of the HFNG. In conjunction with gold activation, we also studied nickel activation during the fast neutron calibration study. Similar to gold activation, a piece of bare nickel sample is placed 20 cm from the target during HFNG operation (10 minute duration). The 2.45 MeV neutrons interact with Ni-58 to produce Co-58 via the (n,p) reaction. Subsequently, the 811 keV gammas from β+ decay are counted to determine the neutron source strength.

Gold activation was also studied for thermal neutron characterization. In this case we simply attached a bare piece of gold foil on the back side of the D_2O moderator (Figure 5.13) and the gold activation by thermal neutrons.

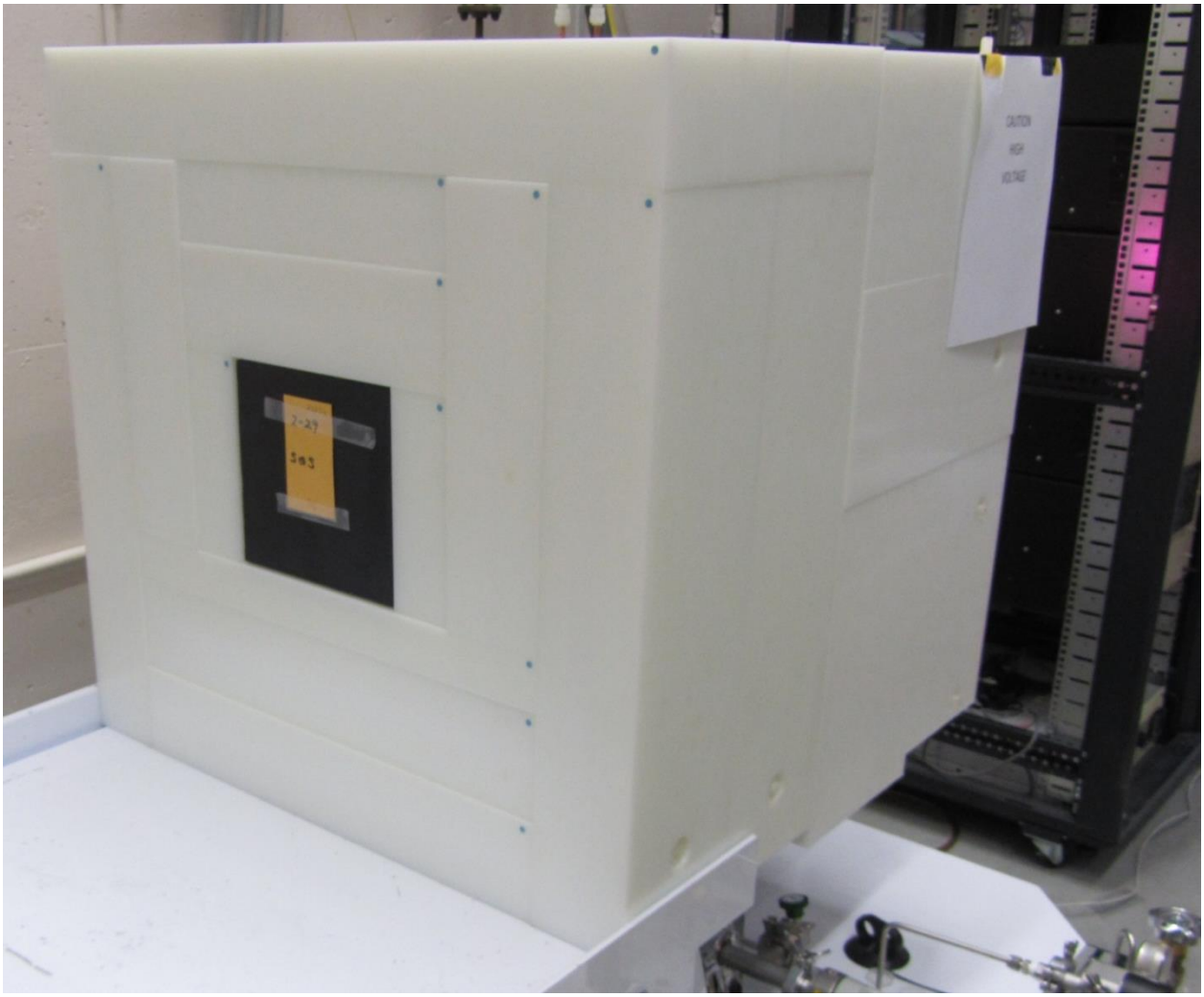

Figure 5.13: Gold activation calibration using D2O moderator. Gold foil is attached to the back of the moderator.

6. Applications of Electronic Neutron Sources for Oil Well-Logging

The viability of replacing Americium-Beryllium (Am-Be) radiological neutron sources in compensated porosity nuclear well logging tools with D-T, D-D, and T-T accelerator-driven neutron sources is explored . The analysis consisted of developing a model for a typical well-logging borehole configuration and computing the helium-3 detector response to varying formation porosities using three different neutron sources (Am-Be, D-D, and D-T). The results indicate that, when normalized to the same source intensity, the use of a D-D neutron source has greater sensitivity for measuring the formation porosity than either an Am-Be or D-T source. The results of the study provide operational requirements that enable compensated porosity well logging with a compact, low power D-D neutron generator, which the current state-of-the-art indicates is technically achievable.

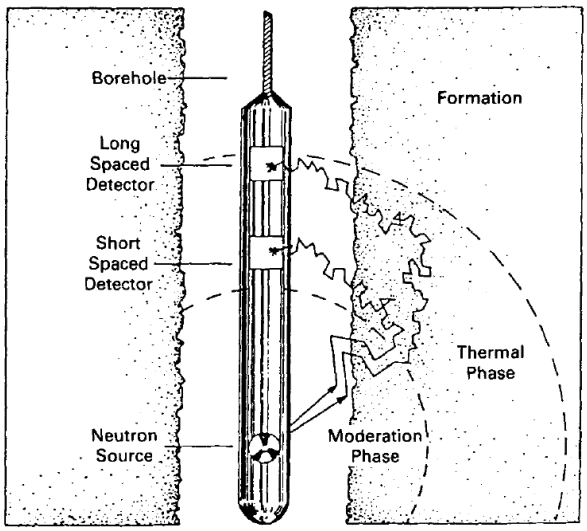

Figure 6.1: Compensated porosity neutron logging tool.

I. Compensated Neutron Porosity Well-Logging (CNL)

Historically, the oil exploration industry has depended heavily on the use of radiological sources such as Am-Be to evaluate valuable oil reserves using the so called compensated porosity neutron logging (CNL). Am-Be is the most commonly used neutron source in CNL because of its high neutron emission intensity, compact size, and long half-life (Am-241 has a half-life of 432 years). Typically, a neutron and a gamma logging tools are used simultaneously to infer useful information about the borehole. The neutron logging tool consists of an Am-Be source with an activity ~10^7 n/s and two thermal neutron detectors (usually He-3 gas-filled detectors) that are located upstream from the neutron source at different locations. The source emits fast neutrons into the rock formation where scattering and absorption processes occur to slow down

the neutrons to thermal energies. Eventually, some of the thermal neutrons diffuse into one of the He-3 detectors and register counts.

The presence of hydrogen in the formation increases the amount of neutron scattering and absorption, which affects the neutron diffusion length, L, and results in different count rates observed in each of the detectors. This difference in detector count rates implies that the porosity can be correlated to the neutron diffusion length in the formation. It can be shown that the ratio of neutron fluxes, ϕ_N/ϕ_F, tallied in the near and far He-3 detectors is given by [64]

$$\frac{\phi_N}{\phi_F} = \frac{r_F}{r_N} exp\left(\frac{r_F - r_N}{L_e}\right) \tag{6.1}$$

where r_N and r_F are the distances from the source to the near and far detectors respectively, and L_e is the epithermal neutron slowing down length. In practice, the exact values of r_N and r_F are approximate since the detectors have finite volume with characteristic lengths comparable to r_N and r_F. In most practical well logs, the parameters r_N and r_F are evaluated through fitting parameters, $C_1 - C_5$ to obtain

$$\frac{\phi_N}{\phi_F} = C_1 exp\left(\frac{C_2}{L}\right) \tag{6.2}$$

$$L(\Phi) = C_3 + C_4\Phi + C_5\Phi^2 \tag{6.3}$$

where L is the average track length traveled by a neutron in the formation, C_1, C_2 are positive constants C_3, C_4, C_5 are polynomial fitting parameters for describing L as a function of the porosity, Φ. Equation (6.2) provides the correlation between the hydrogen content in the formation and the porosity if the two detector flux tallies are measured at different porosities with all other parameters held constant. Since the neutron flux at a location is directly proportional to the measured count rate at that location, the ratio of the near detector count rate to that of the far detector is the parameter used by log analysts to assess the formation porosity.

The major drawback in using an Am-Be source for CNL is the radioactivity and toxicity. Both ^{241}Am and ^{9}Be are hazardous materials and, because of its high radioactivity, ^{241}Am presents additional environmental concerns if a source is lost down hole as well as national security concerns if it is stolen or cannot be accounted for [3]. Because of these issues, there has been strong interest in the well logging community to develop alternative accelerator-based technologies for replacing radiological sources such as Am-Be.

II. Computational Model

The Monte-Carlo computer code MCNP [23] was used to simulate the porosity log in a borehole. In the present simulations, three different neutron sources (D-D, D-T, and Am-Be) were

analyzed within two different formation matrices, limestone, $(CaCO_3)_{1-x}(H_2O)_x$, and sandstone, $(SiO_2)_{1-x}(H_2O)_x$. The formation used in the density was calculated according to

$$\rho_b = \rho_f \Phi + \rho_m (1 - \Phi) \tag{6.4}$$

where ρ_b is the overall formation density, ρ_f is the fluid density (in this case pure water), and ρ_m is the matrix density. The borehole and neutron tool geometries were based on those published by Peeples *et al.* [64] and correspond to an 8 inch borehole and 3 inch diameter tool (Figure 6.2). The three neutron sources were modeled as isotropic point sources with their respective neutron energy spectra shown in Figure 2.10. The energy spectrum of the Am-Be source was derived from the ISO-8529-1 reference spectrum [65] having its corresponding probability density function, while the two accelerator-driven sources produced mono-energetic neutrons at 2.45 MeV (D-D) and 14 MeV (D-T). The near and far detectors were modeled as cylinders containing He-3 at different densities based on their respective pressures of 1.5 and 4.0 atm at a temperature of 293^{o}K. As neutrons enter the cylindrical volume of the detectors, a tally of the $^3He(n,p)^3H$ neutron capture reaction was used to represent the detector count rate.

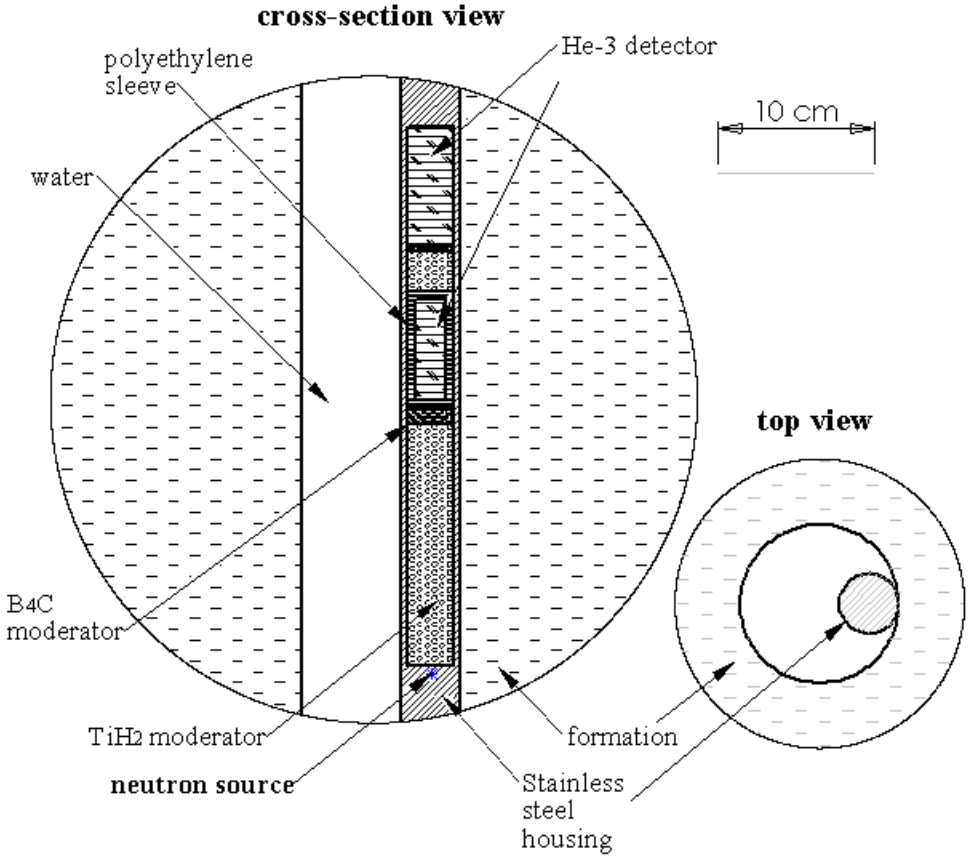

Figure 6.2: Magnified section of the CNL tool and borehole model used in MCNP. [66]

The neutron cross section data in MCNP were taken from the standard ENDF/BVII library [67]. In all cases, simulations were run with 10^8 particles to obtain the proper scaling for the relative error of the measurement. The relative error of an MCNP tally is defined as the ratio of the standard deviation to the expected value of the tally. For the well logging problem, both the expected value and the relative error of the near-to-far detector count ratio were computed. The expected values and relative errors obtained from MCNP correspond to a predefined and fixed borehole/tool configuration. In practice, the well-logging measurements obtained by the detectors will differ from the MCNP results due to perturbations and uncertainties in the composition and geometry. However, the above model using a fixed geometry is suitable for comparing relative neutron source performance for CNL.

III. Simulation Results [66]

The near-to-far detector count rate ratios for the three different neutron sources (D-D, D-T, and Am-Be) are shown in Figure 6.3 with error bars representing one standard deviation from the expected value. As seen in the graphs, the D-D neutron source has the highest sensitivity to the change in porosity fraction while the D-T source is the least sensitive. The D-D neutron source also has the highest relative error in the well log. The D-T source shows significantly lower relative errors compared to the other two suggesting that the D-T source can be operated at a lower output flux without compromising precision.

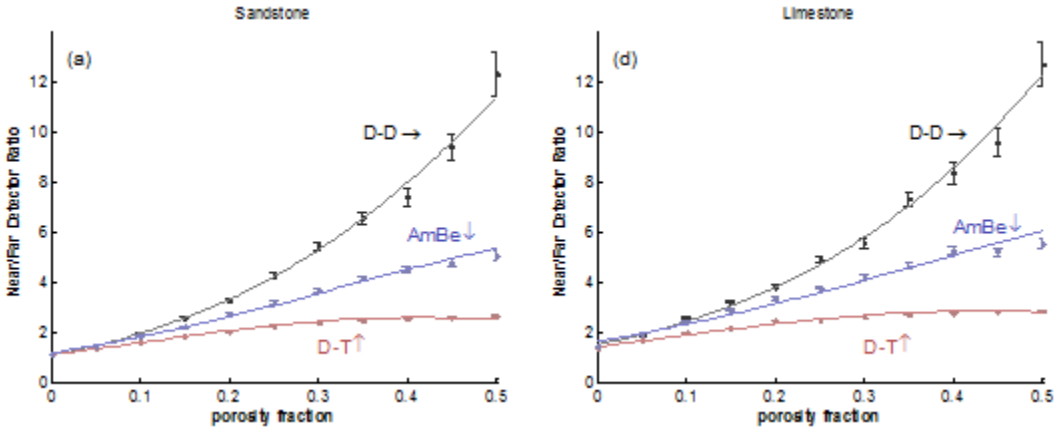

Figure 6.3: MCNP results of sandstone and limestone formations using different neutron sources with 108 particle histories used in all cases.

The dissimilarity in sensitivity between different neutron sources can be analyzed in terms of the average neutron interaction mean free path (T_{mfp}) of the formation defined as the average track length that a neutron particle travels before absorption or scattering occurs. It is equivalent to the neutron flux tally with the volume set to unity. A quadratic least-squares regression yields very good correlation between the inverse of T_{mfp} and the change in porosity fraction. An exponential least squares regression gives a good fit between the near-to-far ratio and the inverse of T_{mfp}. This correlation is more precise in the lower porosity range, likely as a result of lower uncertainty in the neutron flux. Because of its lower neutron energy (compared to D-T and Am-

Be), the D-D neutron source has shorter T_{mfp} at the same porosity since D-D neutrons are easier to thermalize in the formation. This implies that detectors can be positioned much closer to the source leading to a more compact CNL tool and a lower intensity source requirement.

IV. Neutron Detector Technologies for Nuclear Logging Tools

Compensated porosity well logging tools typically consist of an Am-Be neutron source, two He-3 neutron detectors located upstream from the source, and some shielding material between the neutron source and detectors to minimize interferences in the signal. The present study has shown that a D-D neutron source has higher sensitivity to the formation porosity than either a D-T or Am-Be neutron source. He-3 neutron detectors are commonly used in CNL tools because of their high sensitivity to thermal neutrons, but the supply of He-3 is rapidly decreasing so the cost of these detectors is becoming a critical factor. The following sections consider some neutron source and detector technologies that could potentially lead to the next generation of well logging tools for measuring formation porosity.

Neutron detection is a key component of applications in national and homeland security, industry, and science. For example, the federal government uses radiation portal monitors and other neutron detectors at the U.S. border to prevent smuggling of nuclear and radiological material, and the oil and gas industry uses neutron detectors for well logging. He-3 neutron detectors are commonly used in these applications because of its high thermal neutron capture cross section (~5000 barns) as well as its capability for gamma radiation discrimination [67]. Before about 2001, production of helium-3 exceeded consumption but, in the past decade consumption has risen rapidly, in part because of the deployment of neutron detectors at the U.S. borders to detect smuggled nuclear and radiological material. Since 2001, the stockpile of helium-3 has decreased significantly causing prices to skyrocket . For example, the price of He-3 has shot up almost 40 times from ~$80 /liter in 2008 to ~ $3000 /liter in 2011 [68].

One way to address the helium-3 shortage is to move to alternative technologies that are available and could satisfy detection sensitivity requirements for these applications. For example, some candidate technologies include ^{10}B-lined proportional detectors, BF_3 proportional detectors, ^{6}Li-ZnS(Ag) scintillators, and solid-state thermal neutron detectors. These technologies use either ^{10}B or ^{6}Li rather than ^{3}He to efficiently detect thermal neutrons and, further, provide gamma radiation discrimination. Typical boron-lined proportional detector tubes are about 10 to 15% as efficient at detecting neutrons as a ^{3}He tube but, by arraying them, boron-lined tubes can achieve detector efficiency comparable to a single tube ^{3}He neutron detector. In addition, these detectors are more expensive than ^{3}He and ^{10}B is an export controlled material. While BF_3 proportional detectors are relatively inexpensive, BF_3 is a hazardous material and also exhibits a somewhat higher sensitivity to low energy photons which would reduce the signal-to-noise ratio in neutron detection. Generally, BF_3 tubes are about 30 to 50% as efficient at detecting neutrons compared to ^{3}He, but multiple tubes can achieve the desired detector efficiency. Similar to boron-lined proportional counters, ^{6}Li scintillators are much more expensive than ^{3}He and ^{6}Li is also an export controlled material. There are also issues with ^{6}Li scintillators in that the gamma radiation discrimination may not be adequate for some applications, and the detector may not be able to count neutrons at high rates. On the other hand, there are novel solid-state detectors being developed, such as stoichiometric boron carbide, for high rate thermal neutron counting [69]. These detectors rely on quantifying the kinetic energy

imparted by the $^{10}B(n,\alpha)^{7}Li$ recoil to produce a voltage based on the Seebeck coefficient. Typical neutron fluxes of $10^{9} – 10^{11}$ n/(cm^{2}s) can be recorded. Theoretically, these detectors can achieve a maximum of 45% efficiency for thermal neutrons.

The suitability of a detector for an application depends both on the characteristics of the isotope and the detector design. Factors such as how a neutron absorbing isotope is integrated into the conversion material, the arrangement of the moderator relative to the conversion material, and the signal processing for the detector influence the detector's characteristics and response. While alternative detector technologies for He-3 are under development, further work and testing are also needed to fully assess the impact of replacing He-3 in nuclear well logging and other applications.

7. Conclusion

Development of compact electronic gamma sources and high flux neutron generators has been studied to replace existing radiological gamma/neutron sources as well as reactors producing neutrons. In this research the $^{6}Li(d,n)^{7}Be$ (d-^{6}Li) and $^{9}Be(d,n)^{10}B$ (d-^{9}Be) gamma production reactions have been studied and the results show that with higher yields, they are good candidates for replacing existing ^{60}Co, ^{137}Cs, and ^{192}Ir sources. Both d-^{6}Li and d-^{9}Be reactions produce mono-energetic gamma rays that are in the range of energies produced by existing radiological sources.

Pyroelectric crystals were also studied as an ultra-compact method to produce the high acceleration voltages needed for gamma and neutron production. While $LiTaO_3$ crystals have the significant potential for developing extremely high voltages over a few centimeter length scales, one of the remaining technical challenges is to increase the voltage holding ability so that the predicted maximum voltages can be attained for gamma production. Results show that the voltage is limited by sparking across the crystal and contamination of the dielectric fluid after spark initiation. In terms of electric field generation and achieving high duty cycle, thin crystals were found to be much more effective compared to thick crystals. For the single crystal case, the 50 x 30 mm crystals were demonstrated to generate up to 180 kV, which is an appropriate voltage for significant D-D neutron production at an ultra-compact scale. At 180 kV acceleration potential, the D-T neutron yield is approximately four orders of magnitude higher than the D-Be yield.

To achieve higher instantaneous gamma yields, two methods were proposed: (1) a fast mechanical shutter was developed and demonstrated millisecond pulsed ion beam operation and at the same time, provided excellent vacuum isolation between the ion source and acceleration chamber. (2) The stacked pyroelectric system demonstrated the principle of providing pulsed high voltage (up to 60 kV in the present setup) operation in an ultra-compact assembly.

The design and operation of a next generation high flux neutron generator was presented. Current developments at the Berkeley Geochronology Center and Sandia National Laboratories show that maximum neutron yields on the order of $\sim 10^{11}$ n/s and maximum neutron flux on the order of $\sim 10^{11}$ n/cm^2/s are possible. The compactness of the system makes these HFNGs very attractive and combined with an appropriate moderator; the HFNG has the potential of performing work currently done at nuclear reactors and large accelerator facilities. Thermal analysis of the neutron production target showed that the average operational heat flux could be kept below the critical heat flux that initiates departure from nucleate boiling. Furthermore, at sufficiently high pressure, flow rate, and inlet sub-cooling, simulation results suggested that the flow could remain well below the saturation state, allowing the use of single phase heat exchangers and pumps.

Results from Monte-Carlo simulations of the HFNG with different moderating materials showed great promise for use in BNCT. Neutrons generated by the HFNG could be tailored to the desired epithermal energy spectrum while still maintaining a high enough flux for practical treatment time.

Activation analysis of the HFNG system showed that very small quantities of long-lived radiological material are generated in the steady state of operation. Therefore, decommissioning of the HFNG can be done simply and inexpensively.

For the application of oil exploration (well-logging) using lower levels of neutron fluxes, use of existing D-D neutron generators is sufficient to meet and even exceed the performance requirement. In fact, in this research, it has been shown with Monte-Carlo simulations that using a D-D neutron source will yield higher signal sensitivity compared with existing Am-Be radiological sources for compensated porosity measurements. From an economical perspective, the most pressing problem for well logging is the continued availability of neutron detectors. With the price of ^{3}He increasing at an unprecedented pace, alternative technologies for neutron detection should be at a high priority for development.

8. Future Work

Achieving Curie-level activity of the radiological sources used in medical and industrial applications is very difficult for direct gamma producing reactions (d-^{6}Li and d-^{9}Be). Based on Figure 2.4, the ^{9}Be(d,γ)^{10}B reaction requires ~37A of beam current at 125 keV beam energy to replace a Curie-level ($3.7 \cdot 10^{10}$ γ/s) equivalent gammas source. This is a very demanding ion-current requirement for a compact accelerator system. However, the current required to produce $3.7 \cdot 10^{10}$ n/s using the D-D reaction is only ~100 mA and ~2 mA in the case of D-T (Figure 2.9). Future studies should place emphasis on improving the neutron to gamma converter as a practical means for achieving Curie-level gamma yields.

The pyroelectric crystal stacking concept can be explored further to test a variety of crystal lengths and number of stages to obtain the best configuration. Additional work in developing a fast mechanical shutter system for multi-aperture beamlet extraction will be beneficial to increase the ion current for pulsed ion source applications.

Further experiments must be done to characterize the neutron flux profile of the HFNG. Emphasis should be placed on developing a robust system to ensure stable operation over long periods of time with minimal operator interaction. For applications that require epithermal and thermal neutrons, further simulation work is needed in optimizing the moderator material and geometry to produce the maximum possible neutron flux with the desired energies.

9. References

[1] D. Ellis and J. Singer, Well Logging for Earth Scientists (2nd Edition), Springer, 2007.

[2] [Online]. Available: http://www.bestndt.net/sources.html.

[3] Nuclear and Radiation Studies Board Committee on Radiation Source Use and Replacement, "Radiation Source Use and Replacement," The National Academies Press, 2008.

[4] P. Renne, K. Knight, S. Nomade, L. K.-N. and T.-P. Lou, "Application of deuteron-deuteron (D-D) fusion neutrons to 40Ar/39Ar geochronology," *Applied Radiation and Isotopes*, vol. 62, pp. 25-32, 2005.

[5] Oregon State University, [Online]. Available: http://web.engr.oregonstate.edu/~mincleah/Archaeometry_index_files/OSU_TRIGA.htm.

[6] U.S.NRC, "Three Mile Island Accident," U.S.NRC, 2013.

[7] I. N. S. A. Group, "INSAG-7 The Chernbyl Accident: Updating of INSAG-1," Intenational Atomic Energy Agency, Vienna, 1992.

[8] [Online]. Available: http://www.world-nuclear.org/info/Safety-and-Security/Safety-of-Plants/Fukushima-Accident-2011/#.UY_ZaLUZx8E.

[9] J. Dempsey and J. Ewing, "Germany, in Reversal, Will Close Nuclear Plants by 2022," *The New York Times*, 30 May 2011.

[10] S. Leray, F. e. Borne, A. e. Boudard, F. e. Brochard, D. e. Durand, F. Hanappe, S. Menard, S. L. and J. Thun, "Spallation neutron production by 0.8, 1.2, and 1.6 GeV protons on various targets," *Physical Review C*, vol. 65, pp. 044621(1-17), 2002.

[11] [Online]. Available: neutrons.ornl.gov.

[12] E. Durisi, A. Zanini, C. Manfredotti, F. Palamara, M. Sarotto, L. Visca and U. Nastasi, "Design of an epithermal column for BNCT based on D-D fusion neutron facility," *Nuclear Instruments and Methods in Physics Research A,* vol. 574, pp. 363-369, 2007.

[13] N. Colonna, L. Beaulieu, L. Phair, G. Wozniak and L. Moretto, "Measurements of low-energy (d,n) reactions for BNCT," *Medical Physics,* vol. 26, pp. 793-798, 1999.

[14] Varian Medical Systems, [Online]. Available: http://www.varian.com/us/oncology/radiation_oncology/clinac/clinac_ix.html.

[15] F. Cecil, R. Fahlsing and R. Nelson, "Total cross-section measurements for the production of nuclear gamma rays from light nuclei by low energy deuterons," *Nuclear Physics A,* vol. 376, pp. 379-388, 1982.

[16] A. Elwyn, H. R.E., D. C.N., L. Meyer-Schutzmeister, J. Monahan and F. Mooring, "Absolute cross sections for deuteron-induced reactions on 6Li at energies below 1 MeV," *Physical Review C,* vol. 16, pp. 1744-1756, 1977.

[17] S. Szegedi, "Investigations on nuclear reactions induced by proton and deuterons in Be," *Acta Physica Academiae Scientiarum Hungaricae,* vol. 34, pp. 215-223, 1973.

[18] J. Ziegler, M. Ziegler and J. Biersack, "SRIM - The stopping and range of ions in matter (2010)," *Nuclear Instruments and Methods in Physics Research Section B,* vol. 268, no. 11-12, pp. 1818-1823, 2010.

[19] R. Coombe and J. Walker, "Neutrons Emitted in the 9Be(d,n)10B Reaction at a Deuteron Energy of 80 keV," in *Proc. Phys. Soc.*, 1962.

[20] C. Mandeville, C. Swann and S. Snowdon, "Neutrons from Deuteron on Lithium (6)*," *Physical Review,* vol. 76, p. 980, 1949.

[21] "DOE Handbook - Tritium Handling and Safe Storage," U.S. Department of Energy, Washington D.C. 20585, 1999.

[22] G. e. Dale, "Alternative Neutron Sources for Well Logging," in *CAARI,* 2012.

[23] J. Briesmeister, "MCNP -- A General Monte Carlo N-Particle Transport Code," Los

Alamos National Laboratories, 2000.

[24] K.-N. Leung, "The application and status of the radio frequency driven multi-cusp ion source," *Review of Scientific Instruments,* vol. 71, p. 1064, 2000.

[25] M. Kato and K. Tsuno, "Numerical analysis of trajectories and aberrations of a Wien filter including the effect of fringing fields," *Nuclear Instruments and Methods in Research A,* vol. 298, pp. 290-320, 1990.

[26] M. Lieberman and L. A.J., Principles of Plasma Discharges and Materials Processing, 2nd Edition, John Wiley & Sons, 2005.

[27] X. Jiang, Q. Ji, A. Chang and K. N. Leung, "Mini RF-driven ion sources for focused ion beam systems," *Review of Scientific Instruments,* vol. 74, no. 4, pp. 2288-2292, 2003.

[28] V. Vahedi, "Modeling and Simulation of RF Discharges," University of California at Berkeley - Ph.D. Thesis, 1993.

[29] K.-N. Leung, Interviewee, *Private Communication.* [Interview].

[30] Amptek Inc., [Online]. Available: http://amptek.com/coolx.html.

[31] J. Geuther and Y. Danon, "High-energy x-ray production with pyroelectric crystals," *Journal of Applied Physics,* Vols. 97, 104916, 2005.

[32] B. Naranjo, J. Gimzewski and S. Putterman, "Observation of nuclear fusion driven by a pyroelectric crystal," *Nature,* vol. 434, pp. 1115-1117, 2005.

[33] V. e. Tang, "Neutron production from feedback controlled thermal cycling of a pyroelectric crystal," *Review of Scientific Instruments,* vol. 78(123504), 2007.

[34] W. Tornow, S. Shafroth and J. Brownridge, "Evidence of neutron production in deuterium gas with a pyroelectric crystal without tip," *Journal of Applied Physics,* Vols. 104, 034905, no. 3, 2008.

[35] V. Tang, G. Meyer, S. Falabella, G. Guethlein, S. Sampayan, P. Kerr, B. Rusnak and J. Morse, "Intense pulsed neutron emission from a compact pyroelectric driven accelerator,"

Journal of Applied Physics, Vols. 105, 26103, 2009.

[36] A. Glass, "Dielectric, Thermal, and Pyroelectric Properties of Ferroelectric LiTaO3," *Physical Review*, vol. 172, pp. 564-571, 1968.

[37] S. Leng, "Bulk and Surface Resistivity of LiNbO3 and LiTaO3 Crystals versus Temperature," *Phys. Stat. Sol. (a)*, vol. 143, p. 431, 1994.

[38] D. Gillich, A. Kovanen, B. Herman, T. Fullem and D. Y., *Nuclear Instruments and Methods in Physics Research A*, vol. 602, pp. 306-310, 2009.

[39] Red Optronics, [Online]. Available: www.redoptronics.com/litao3-crystals.html.

[40] Almaz Optics Inc., [Online]. Available: www.almazoptics.com/LiTaO3.html.

[41] V. Tang, Interviewee, *Private Communication.* [Interview].

[42] [Online].Available: http://multimedia.3m.com/mws/mediawebserver?mwsId=66666UF6EVsSyXTtnxTE5Xz6EVtQEVs6EVs6EVs6E666666--&fn=prodinfo_FC70.pdf.

[43] National Instruments Labview, [Online]. Available: http://www.ni.com/labview.

[44] S. Kim and V. Gopalan, "Coercive fields in ferroelectrics: A case study in lithium niobate and lithium tantalate," *Applied Physics Letters*, vol. 80, pp. 2740-2742, 2002.

[45] A. Chen, A. Antolak, K.-N. Leung, D. Morse and T. Raber, "Pulsed Pyroelectric Crystal-Powered Gamma Source," *AIP Conf. Proc.: Application of Accelerators in Research and Industry*, vol. 1525, pp. 720-724, 2013.

[46] A. Antolak, A. Chen, K.-N. Leung, D. Morse and T. Raber, "Radiatively heated high voltage pyroelectric crystal pulser," *Nuclear Instruments and Methods in Physics Research A*, vol. 735, pp. 379-381, 2014.

[47] J. Reijonen, G. F., S. Hahto, M. King, T.-P. Lou and K.-N. Leung, "D-D neutron generator development at LBNL," *Applied Radiation and Isotopes*, vol. 63, pp. 757-763, 2005.

[48] L. Ahle, H. R.P., A. Molvik, J. Kwan and K.-N. Leung, "RF gas plasma source development for heavy ion fusion," *Review of Scientific Instruments,* vol. 73, 2002.

[49] A. Chen, A. Antolak, K.-N. Leung, T. Raber and D. Morse, "Compact Electronic Gamma Source for Radiotherapy," in *CAARI 2010*, 2011.

[50] M. Rickey and R. Smyth, "The acceleration and extraction of negative hydrogen ions in the C.U. Cyclotron," *Nuclear Instruments and Methods,* vol. 18, pp. 66-69, 1962.

[51] A. Chen, A. Antolak, K.-N. Leung, T. Raber and D. Morse, "Fast mechanical shutter for pulsed ion beam generation," *Nuclear Instruments and Methods in Physics Research A,* vol. 670, pp. 45-48, 2012.

[52] Huntington Mechanical Laboratories Inc., [Online]. Available: http://www.huntvac.com.

[53] Pfeiffer Vacuum Inc., [Online]. Available: http://www.pfeiffer-vacuum.com.

[54] Thermo Scientific Inc., [Online]. Available: http://www.thermoscientific.com/ecomm/servlet/productsdetail?productId=11962782&groupType=PRODUCT&searchType=0&storeId=11152&from=search.

[55] M. Davis, J. Little, A. K.M.M.S. and A. Reddy, "Relative Biological Effectiveness of the 10B(n,a)7Li Reaction in HeLa Cells," *Radiation Research Society,* vol. 43, pp. 534-553, 1970.

[56] M. Takagaki, Y. Oda, M. S., K. H., T. Kobayashi, S. Y., O. M., K. Mori and K. Ono, "Boron neutron capture therapy: preliminary study of BNCT with sodium borocaptate (Na2B1-2H1-1SH) on glioblastoma," *Journal of Neuro-oncology,* vol. 35, pp. 177-185, 1997.

[57] T.-P. Lou, "Compact D-D/D-T Neutron Generators and Their Applications," University of California at Berkeley - Ph.D. Thesis, 2003.

[58] J. De Beeck, "Neutron Flux Distribution Around the Disk-Shaped Source of Accelerator Type Neutron Generators," *Journal of Radioanalytical Chemistry,* vol. 1, pp. 313-323, 1968.

[59] G. Celata, M. Cumo and A. Mariani, "Assement of correlations and models for the prediction of CHF in subcooled flow boiling," *Int. J. Heat Mass Transfer,* vol. 37, pp. 237-255, 1994.

[60] V. Borishanky, "Correlation of the effect of pressure on the critical heat flux and heat transfer rates using the theory of thermodynamic similarity," *Problems of Heat Transfer and Hydraulics of Two-Phase Media,* pp. 16-37, 1969.

[61] P. Rinard, "Neutron Interaction with Matter," [Online]. Available: www.fas.org/sgp/othergov/doe/lanl/lib-www/la-pubs/00326407.pdf.

[62] A. Chen and L. K.-N., "An Improved Epithermal Neutron Source Design for BNCT," in *15th Internation Congress on Neutron Capture Therapy*, 2012.

[63] A. Steyerl, H. Nagel, F.-X. Schreiber, K.-A. Steinhauser, R. Gahler and G. W., "A new source of cold and ultracold neutrons," *Physics Letters A,* vol. 116, pp. 347-352, 1986.

[64] C. R. Peeples, M. Mickael and R. P. Gardner, "On replacing Am-Be neutron sources in compensated porosity logging tools," *Applied Radiation and Isotopes,* no. 68, pp. 926-931, 2010.

[65] Internation Standard, "ISO/DIS 8529-1," 2000. [Online]. Available: http://www.iso.org/iso/iso_catalogue/catalogue_tc/catalogue_detail.htm?csnumber=25667.

[66] A. X. Chen, A. J. Antolak and K.-N. Leung, "Electronic Neutron Sources for Compensated Porosity Well Logging," *Nuclear Instruments and Methods in Physics Research Section A,* vol. 684, pp. 52-56, 2012.

[67] NNDC, "ENDF," 2006. [Online]. Available: http://www.nndc.bnl.gov/exfor/endf00.jsp.

[68] D. Kramer, *Physics Today,* May 2011.

[69] D. Emin and T. Aselage, "A proposed boron-carbide-based solid-state neutron detector," *Appl. Phys.*, Vols. 97, 013529, 2005.

10. Appendix

I. Input Files for MCNP simulations

a. BGC HFNG Shielding simulation

```
Title - Etcheverry HFNG Room Shielding for BGC
C ------------------------------------------------------------------------------
C Created by Allan Chen with the help of Chris Pieronek and Dr. Tak-Pui Lou
C Updated 050213
C ------------------------------------------------------------------------------
C Cells
C ------------------------------------------------------------------------------
10 100 -2.7 -101 103 -104 (102:-105:106) 107 -108 109 110:
     (102:-105:106) -101 (102:117) -107 111        $ Aluminum Chamber w/Rest
11 910 -2.65 (-820 821:822 -823) -109               $ Quartz Window Chamber
15 100 -2.7 -250 251 272 -252                        $ Elbow
16 100 -2.7 -256 (-222:-255) (102:221) 254 -302 252 $ Reducer
17 100 -2.624 -270 -272 271                          $ Turbo Pump
20 200 -1.08 205 -206 207 -208 111 -212 (-201:202:-203:204:213) 150:
     (108 -101 103 -104 (-130:143 -144 (-141:145) (-142:-146)) -212)
     (-133:134:-135 131:136 132:210) #155        $ Poly Shielding
C 130 0 (-205:206:-207:208:211) (305 -306 307 -308 209 -311)   $ Lead
30 100 -2.7 -303 302 -111 102:316 -317 -314 315        $ Aluminum Table
41 300 -7.4 411 -421 431 -441 92 -93                $ Target Magnets
42 LIKE 41 BUT TRCL=42
43 LIKE 41 BUT TRCL=43
44 LIKE 41 BUT TRCL=44
51 0 512 -513 514 -515                        u=2 $ Sample Slot
52 400 -7.45 #51 #61 #71                       u=2 $ Copper Segment
61 0 (602:-601) 606:(601:-602) -605           u=2 $ Water Channel
71 0 (700 -701:-705 706) 514 -515               u=2 $ V groove
150 0 603 -604 504 -505 u=1 lat=1 fill=-4:4 0:0 0:0
     2 2 2 2 2 2 2 2 2                      $ Target component fill
151 0 90 -91 502 -503 92 -93 fill=1             $ Target
152 400 -7.45 ((502 -503 (500 -90:91 -501) 92 -93):
     ((-92 504:93 -505) 500 -501 502 -503))
     #41 #42 #43 #44 #153 #154 $ Target Wings      & Caps
153 0 512 -513 514 -515 (500 -90:-501 91)          $ Wing Slot
154 500 -1 420 -421 440 -441 (-92 94:93 -95)       $ Target Water Bath
155 100 -2.7 -921 -922 505
C Cell 100-115 Source Magnets
```

```
100 300 -7.4 (120 -122 -124 125 -126 128):          $ Ion Source Magnets
          (-121 123 -124 125 -126 128)
101 LIKE 100 BUT TRCL=101
102 LIKE 100 BUT TRCL=102
103 LIKE 100 BUT TRCL=103
104 LIKE 100 BUT TRCL=104
105 LIKE 100 BUT TRCL=105
106 LIKE 100 BUT TRCL=106
107 LIKE 100 BUT TRCL=107
108 LIKE 100 BUT TRCL=108
109 LIKE 100 BUT TRCL=109
110 LIKE 100 BUT TRCL=110
111 LIKE 100 BUT TRCL=111
112 LIKE 100 BUT TRCL=112
113 LIKE 100 BUT TRCL=113
114 LIKE 100 BUT TRCL=114
115 LIKE 100 BUT TRCL=115
C Cell 80 Copper Sources
80 400 -7.45 ((800 -802 -110 804):
      (-801 803 -110 804)) #100 #101 #102 #103
      #104 #105 #106 #107 #108 #109
      #110 #111 #112 #113 #114 #115              $ Ion Source
120 501 1E-6 (800 -802 -804):(-801 803 -804)       $ Plasma
220 900 -10.28 -110 (-105 801:106 -800)            $ Extraction Plate
230 910 -2.65 (802 -812:-803 813) -110             $ Quartz Plate
C Cell 90 91 Room Air
90 600 -1.23E-3 (201 -202 203 -204 107 -130 (101:-103:104) (110:812:-813):
    201 -202 203 -204 -107 101 111:
    -150 -212 130 (-143:144:-145 141:146 142):
    150 130 -213 201 -202 203 -204:
    ((-821 201:823 -202) -109):
    209 -909 -907 (932:-931:220) (-934:935) 905 901 -903
    (((-205:206:-207:208:212) 314:317 270:-271):
    -907 -315 209 250 272 (932:-931) 901 -903:
    271 -272 270 -315 209:
    205 -206 207 -208 (-111 (303:-302) (256:222) 255 252:
    315 (-316:314) 250 -252)):907 -908
    (-944:(-942:941 -943))) #155
91 600 -1.23e-3 909 -910 (-940 -949:-946 947 -948:-945 949)
C Concrete Walls
86 800 -2.4 -209 321 912 -914 916 -918 (-902:904:-906:908)
88 800 -2.4 (909:-901:903:-905:907:-209)
      902 -904 906 -908 -910 321
      (943:-941) (942:-907) (944:-907) #91
89 800 -2.4 209 -220 931 -907 -932 901
87 800 -2.4 220 -909 901 -907 -935 934
```

```
C Cell 99 - Vacuum Inside
99 0 ((-500:501:-502:503:-504:505) (105 -106:-117) (-221:-254) 252
    -108 (-102:-109 820 -822):-251 -252 272:
    108 133 -134 (135:-131) (-136:-132) -210 -212)  #155
C Outside boundary
199 0  (910:908:904:-902:-906) 209 -920 -918 -914 912 916
C Non-important Zone outside
999 0  920:918:-916:914:-912:-321

C ------------------------------------------------------------------------
C Surfaces
C ------------------------------------------------------------------------
C ---------------------------- Vacuum Vessel Surfaces -------------------------
101 CZ  18.503                $ Outer cylindrical surface
102 CZ  15.9                  $ Inner cylindrical surface
103 PY  -9.627                $ Outer planar surface 1
104 PY   9.627                $ Outer planar surface 2
105 PY  -7.087                $ Inner planar surface 1
106 PY   7.087                $ Inner planar surface 2
107 PZ  -14                   $ Bottom Bound
108 PZ   14                   $ Top Bound
109 CX   3.4925               $ Gauge/Equipment Holes
110 CY   9.5                  $ Ion Source Holes
111 PZ  -24                   $ Chamber Rest Bottom Bound
117 PZ  -16                   $ Bottom Chamber Lip bottom
130 PZ   16.5                 $ HV Insulator
131 C/Z -3.5 0 2
132 C/Z  3.5 0 2
133 PY  -2
134 PY   2
135 PX  -3.5
136 PX   3.5
141 C/Z -3.5 0 4.5
142 C/Z  3.5 0 4.5
143 PY  -4.5
144 PY   4.5
145 PX  -4.5
146 PX   4.5
150 CZ  10
201 PX -20
202 PX 20         $ Shielding Surfaces
203 PY -20
204 PY 20
205 PX -40.32
206 PX 40.32
207 PY -40.32
```

```
208 PY 40.32
209 PZ -90        $ Floor
210 PZ 44.5
211 PZ 70
212 PZ 47
213 PZ 27
220 PZ -30
221 KZ -64.225 0.2158 1
222 KZ -65 0.2158 1
250 TY -30 0 -46 30 10.3 10.3  $ Elbow
251 TY -30 0 -46 30 10 10
252 PZ -46
253 PZ -42.7
254 CZ 10
255 CZ 10.3
256 CZ 16.2
270 C/X 0 -76 12.1       $ Turbo Pump
271 PX -59
272 PX -30
C Table Surfaces
302 PZ -26.54           $ Bottom of Top Aluminum Frame Shelf
303 CZ 33
314 PZ -55.75
315 PZ -57              $ Bottom of Bottom Al Frame Shelf
316 CZ 28.3
317 CZ 58.2
C Lead Outer Surfaces
305 PX -75
306 PX 75
307 PY -75
308 PY 75
311 PZ 75
321 PZ -185      $ Concrete Floor Bottom
325 PX -100
326 PX 100
327 PY -100
328 PY 100
C Concrete Walls
901 PY -252
902 PY -400
903 PY  212
904 PY  460
905 10 PX -232
906 10 PX -373
907 10 PX  232
908 10 PX  387
```

```
909 PZ  336
910 PZ  595
931 10 PX  22
932 PY -60
934 10 PX 125
935 PY -145
940 C/Z 11 -36 7.62        $ Roof Penetration
941 10 PX 309
942 C/X -19 139 3.81       $ 3" to 6" penetration
943 C/X -19 139 7.62
944 900 CX 7.62            $ Angled Penetration
945 C/Z 11 20 7.62
946 C/Y 11 481 7.62
947 PY -44
948 PY 28
949 PZ 481
C Outside boundary
912 PY -420
914 PY 480
916 10 PX -393
918 10 PX 407
920 PZ 615
921 CZ 0.95
922 PZ 100
C ------------------------ Target Surfaces --------------------------------
C Target Magnets
411 PX 3.3225
420 PX -3.9575
421 PX 3.9575
431 PY 0.2285
440 PY -0.8635
441 PY 0.8635
C Target Box
500 PX -4.445
501 PX 4.445
502 PY -1.031
503 PY 1.031
504 PZ -5.08
505 PZ 5.08
C Sample Box
512 PY -0.159
513 PY 0.159
514 PZ -3.175
515 PZ 3.175
C Water Channels
601 P 1 0.414 0 0
```

```
602 P 1 -0.414 0 0
603 PX -0.357
604 PX 0.357
605 PY -0.21
606 PY 0.21
C V-grooves
700 P 1 0.414 0 0.09
701 P 1 -0.414 0 -0.09
702 PZ -3.105
703 PZ 3.105
705 P 1 0.414 0 -0.09
706 P 1 -0.414 0 0.09
90 PX -3.213 $ Non-universe target surfaces
91 PX 3.213
92 PZ -3.81
93 PZ 3.81
94 PZ -4.29
95 PZ 4.29
C Ion Sources Surfaces
800 PY 7.4
801 PY -7.4
802 PY 13.3
803 PY -13.3
804 CY 6.19
812 PY 14.1
813 PY -14.1
C Ion Source Magnet
120 PY 8.035          $ Ion Source Magnets
121 PY -8.035
122 PY 11.845
123 PY -11.845
124 PX 0.635
125 PX -0.635
126 PZ 8.447
127 PZ -8.447
128 PZ 7.177
129 PZ -7.177
C --------------------
820 PX -17.36         $ Quartz Window Chamber
821 PX -18
822 PX 17.36
823 PX 18

C ------------------------------------------------------------------------
C Data
C ------------------------------------------------------------------------
```

```
TR10 -170 0 0 $ Room transformation to accomodate generator
C Magnet Coordinate Transformations
TR4   0     -0.05    0
TR42  -7.28   0      0
TR43  0       -1.092  0
TR44  -7.28  -1.092  0
TR62  -0.714  0      0
TR63  -1.428  0      0
TR64  -2.142  0      0
TR65   0.714  0      0
TR66   1.428  0      0
TR67   2.142  0      0
TR68   2.856  0      0
TR72  -0.714  0      0
TR73  -1.428 0 0
TR74  -2.142 0 0
TR75  -2.856 0 0
TR76   0.714 0 0
TR77   1.428 0 0
TR78   2.142 0 0
TR79   2.856 0 0
TR101  0 0 0 0.9239 0 -0.3827 0 1 0 0.3827 0 0.9239
TR102  0 0 0 0.7071 0 -0.7071 0 1 0 0.7071 0 0.7071
TR103  0 0 0 0.3827 0 -0.9239 0 1 0 0.9239 0 0.3827
TR104  0 0 0 0 0 -1 0 1 0 1 0 1
TR105  0 0 0 -0.3827 0 -0.9239 0 1 0 0.9239 0 -0.3827
TR106  0 0 0 -0.7071 0 -0.7071 0 1 0 0.7071 0 -0.7071
TR107  0 0 0 -0.9239 0 -0.3827 0 1 0 0.3827 0 -0.9239
TR108  0 0 0 -1 0 0 0 1 0 0 0 -1
TR109  0 0 0 -0.9239 0 0.3827 0 1 0 -0.3827 0 -0.9239
TR110  0 0 0 -0.7071 0 0.7071 0 1 0 -0.7071 0 -0.7071
TR111  0 0 0 -0.3827 0 0.9239 0 1 0 -0.9239 0 -0.3827
TR112  0 0 0 0 0 1 0 1 0 -1 0 0
TR113  0 0 0 0.3827 0 0.9239 0 1 0 -0.9239 0 0.3827
TR114  0 0 0 0.7071 0 0.7071 0 1 0 -0.7071 0 0.7071
TR115  0 0 0 0.9239 0 0.3827 0 1 0 -0.3827 0 0.9239
TR900  62 -60 190 0.707 0.707 0 -0.707 0.707 0 0 0 1
TR901  -.357 0 0
TR902  -.714 0 0
TR903  -1.071 0 0
TR904  -1.428 0 0
TR905  -1.785 0 0
TR906  -2.142 0 0
TR907  -2.499 0 0
TR908  -2.856 0 0
TR909  .357 0 0
```

```
TR910  .714 0 0
TR911  1.071 0 0
TR912  1.428 0 0
TR913  1.785 0 0
TR914  2.142 0 0
TR915  2.499 0 0
TR916  2.856 0 0
TR917  3.213 0 0
C Materials for Geometry
M100   13027.70c 1 $ Aluminum
M200   6000.70c  0.3333 $ Polyethylene
       1001.70c  0.6667
M300   60142.70c 0.032 $ Nd-Fe-B Magnets
       60143.70c 0.014
       60144.70c 0.028
       60145.70c 0.010
       60146.70c 0.020
       60148.70c 0.007
       60150.70c 0.007
       26054.70c 0.047792
       26056.70c 0.755773
       26057.70c 0.018128
       26058.70c 0.002307
       5010.70c  0.0116
       5011.70c  0.0464
C M301 26054.70c 1
C M302 26058.70c 1
C M303 60142.70c 1
C M304 60143.70c 1
C M305 60144.70c 1
C M306 60146.70c 1
M400  29063.70c 0.6915 $ Copper-63
      29065.70c 0.3085 $ Copper-65
C M401  29063.70c 1
C M402  29065.70c 1
M500  1001.70c 0.667 $ Water
      8016.70c 0.333
M501  1002.70c 1
M600  8016.70c       -0.232       $ Dry Air
      7014.70c       -0.754
      18000.42c      -0.014
M601  18036.70c  1
M602  18040.70c  1
C M700  82000 1 $ Lead
M800  1001.70c  -0.0221   $ Concrete
      6000.70c  -0.002484
```

```
     8016.70c  -0.574930
     11023.70c -0.015208
     12000 -0.001266
     13027.70c -0.019953
     14000.21c -0.304627
     19000 -0.010045
     20000 -0.042951
     26000.21c -0.006435
M900 42000.66c 1   $ Moly Plate
C M900  42092.70c  0.1484    $ Moly plate
C      42094.70c  0.0925
C      42095.70c  0.1592
C      42096.70c  0.1668
C      42097.70c  0.0955
C      42098.70c  0.2413
C      42100.70c  0.0963
C M901  42098.70c  1
M910  14028.70c 0.3074      $ Quartz
     14029.70c 0.0156
     14030.70c 0.0103
      8016.70c 0.6667
M911  14030.70c 1
C Scattering Kernels
MT100 al27.12t $ Aluminum
MT200 poly.10t $ natural polyethylene
MT300 fe56.13t $ Iron
MT500 lwtr.11t $ Hydrogen in Light Water
C ---------- Tallies --------------------
C ---- Mesh Tallies -----
FMESH4:N ORIGIN=-3 -0.1 -3 IMESH=3 JMESH=0.1 KMESH=3
         IINTS=30 JINTS=1 KINTS=30 FACTOR=3E11
C Source - 2.5cm radius disk source that are located
C in the middle of the two V-groove arrays
C SDEF POS=0 0 0 AXS 0 1 0 RAD=D2 PAR=N ERG=2.45 TR=D1
C SI1 L 201 202
C SP1 0.5 0.5
C TR201 0 -0.3 0
C TR202 0 0.3 0
C SI2 0 2.5
C SP2 -21 1
C More accurate source (coming soon...)
SDEF POS=D3 RAD=D1 SUR=700 PAR=N ERG=2.45 TR=D5 VEC=D2
SI2 L 0 1 0 0 -1 0
SP2 1 1
SI5 L 200 201 202 203 204 205 206 207 208
     210 211 212 213 214 215 216 217 218
```

```
    220 221 222 223 224 225 226 227 228
    230 231 232 233 234 235 236 237 238
SP5   0.035714 35R
TR200  -0.1785  0.63 0
TR201  -0.8925  0.63 0
TR202  -1.6065  0.63 0
TR203  -2.3205  0.63 0
TR204  -3.0345  0.63 0
TR205   0.5355  0.63 0
TR206   1.2495  0.63 0
TR207   1.9635  0.63 0
TR208   2.6775  0.63 0
TR210   0.1785  0.63 0 -1 0 0 0   1 0 0 0 1
TR211   0.8925  0.63 0 -1 0 0 0   1 0 0 0 1
TR212   1.6065  0.63 0 -1 0 0 0   1 0 0 0 1
TR213   2.3205  0.63 0 -1 0 0 0   1 0 0 0 1
TR214   3.0345  0.63 0 -1 0 0 0   1 0 0 0 1
TR215  -0.5355  0.63 0 -1 0 0 0   1 0 0 0 1
TR216  -1.2495  0.63 0 -1 0 0 0   1 0 0 0 1
TR217  -1.9635  0.63 0 -1 0 0 0   1 0 0 0 1
TR218  -2.6775  0.63 0 -1 0 0 0   1 0 0 0 1
TR220  -0.1785 -0.63 0 -1 0 0 0   1 0 0 0 1
TR221  -0.8925 -0.63 0 -1 0 0 0   1 0 0 0 1
TR222  -1.6065 -0.63 0 -1 0 0 0   1 0 0 0 1
TR223  -2.3205 -0.63 0 -1 0 0 0   1 0 0 0 1
TR224  -3.0345 -0.63 0 -1 0 0 0   1 0 0 0 1
TR225   0.5355 -0.63 0 -1 0 0 0   1 0 0 0 1
TR226   1.2495 -0.63 0 -1 0 0 0   1 0 0 0 1
TR227   1.9635 -0.63 0 -1 0 0 0   1 0 0 0 1
TR228   2.6775 -0.63 0 -1 0 0 0   1 0 0 0 1
TR230   0.1785 -0.63 0
TR231   0.8925 -0.63 0
TR232   1.6065 -0.63 0
TR233   2.3205 -0.63 0
TR234   3.0345 -0.63 0
TR235  -0.5355 -0.63 0
TR236  -1.2495 -0.63 0
TR237  -1.9635 -0.63 0
TR238  -2.6775 -0.63 0
SI3 L 0 0 3
    0 0 2.8
    0 0 2.6
    0 0 2.4
    0 0 2.2
    0 0 2.0
    0 0 1.8
```

```
     0 0 1.6
     0 0 1.4
     0 0 1.2
     0 0 1.0
     0 0 0.8
     0 0 0.6
     0 0 0.4
     0 0 0.2
     0 0 0
     0 0 -3
     0 0 -2.8
     0 0 -2.6
     0 0 -2.4
     0 0 -2.2
     0 0 -2.0
     0 0 -1.8
     0 0 -1.6
     0 0 -1.4
     0 0 -1.2
     0 0 -1.0
     0 0 -0.8
     0 0 -0.6
     0 0 -0.4
     0 0 -0.2
SP3   0.032258 30R
SI1 0 0.2
SP1 -21 1
NPS 1E8
MODE N
C MODE N P
PHYS:P 100 1 0 0 0
imp:p 1 48R 0
imp:n 1 48R 0
PRINT 110
```

b. **Dose rate tallies**

```
C ---------- Tallies for neutron and photons --------------------
FMESH14:N origin=-308 -420 -2.5 imesh=407 jmesh=480 kmesh=2.5
      iints=143 jints=180 kints=1 factor 1.08E9
DE14   1.0E-9 1.0E-8 2.5E-8 1.0E-7 2.0E-7 5.0E-7 1.0E-6 2.0E-6 5.0E-6
     1.0E-5 2.0E-5 5.0E-5 1.0E-4 2.0E-4 5.0E-4 1.0E-3 2.0E-3 5.0E-3
     0.0100 0.0200 0.0300 0.0500 0.0700 0.1000 0.1500 0.2000 0.3000
     0.5000 0.7000 0.9000 1.0000 1.2000 1.5000 2.0000 3.0000
DF14   1.7    2.03   2.31   2.98   3.36   3.86   4.17   4.40   4.59
     4.68   4.72   4.73   4.72   4.67   4.60   4.58   4.61   4.86
     5.57   7.41   9.46   13.7   18.0   24.3   34.7   44.7   63.8
     99.1   131    160    174    193    219    254    301
FMESH24:P origin=-308 -420 -2.5 imesh=407 jmesh=480 kmesh=2.5
      iints=143 jints=180 kints=1 factor 1.08E9
DE24   0.010 0.015 0.020 0.030 0.040 0.050 0.060 0.070 0.080 0.100 0.150
     0.200 0.300 0.400 0.500 0.511 0.600 0.662 0.800 1.000 1.117 1.333
     1.500 2.000 3.000 4.000 5.000 6.000 6.129 8.000 10.00 15.00 20.00
DF24   .0337 .0664 .0986 0.158 0.199 0.226 0.248 0.273 0.297 0.355 0.528
     0.721 1.120 1.520 1.920 1.960 2.300 2.540 3.040 3.720 4.100 4.750
     5.240 6.550 8.840 10.80 12.70 14.40 14.60 17.60 20.60 27.70 34.40
FMESH34:N origin=-308 -420 187.5 imesh=407 jmesh=480 kmesh=192.5
      iints=143 jints=180 kints=1 factor 1.08E9
DE34   1.0E-9 1.0E-8 2.5E-8 1.0E-7 2.0E-7 5.0E-7 1.0E-6 2.0E-6 5.0E-6
     1.0E-5 2.0E-5 5.0E-5 1.0E-4 2.0E-4 5.0E-4 1.0E-3 2.0E-3 5.0E-3
     0.0100 0.0200 0.0300 0.0500 0.0700 0.1000 0.1500 0.2000 0.3000
     0.5000 0.7000 0.9000 1.0000 1.2000 1.5000 2.0000 3.0000
DF34   1.7    2.03   2.31   2.98   3.36   3.86   4.17   4.40   4.59
     4.68   4.72   4.73   4.72   4.67   4.60   4.58   4.61   4.86
     5.57   7.41   9.46   13.7   18.0   24.3   34.7   44.7   63.8
     99.1   131    160    174    193    219    254    301
FMESH44:P origin=-308 -420 187.5 imesh=407 jmesh=480 kmesh=192.5
      iints=143 jints=180 kints=1 factor 1.08E9
DE44   0.010 0.015 0.020 0.030 0.040 0.050 0.060 0.070 0.080 0.100 0.150
     0.200 0.300 0.400 0.500 0.511 0.600 0.662 0.800 1.000 1.117 1.333
     1.500 2.000 3.000 4.000 5.000 6.000 6.129 8.000 10.00 15.00 20.00
DF44   .0337 .0664 .0986 0.158 0.199 0.226 0.248 0.273 0.297 0.355 0.528
     0.721 1.120 1.520 1.920 1.960 2.300 2.540 3.040 3.720 4.100 4.750
     5.240 6.550 8.840 10.80 12.70 14.40 14.60 17.60 20.60 27.70 34.40
FMESH54:N origin=-308 -420 -136.5 imesh=407 jmesh=480 kmesh=141.5
      iints=143 jints=180 kints=1 factor 1.08E9
DE54   1.0E-9 1.0E-8 2.5E-8 1.0E-7 2.0E-7 5.0E-7 1.0E-6 2.0E-6 5.0E-6
     1.0E-5 2.0E-5 5.0E-5 1.0E-4 2.0E-4 5.0E-4 1.0E-3 2.0E-3 5.0E-3
     0.0100 0.0200 0.0300 0.0500 0.0700 0.1000 0.1500 0.2000 0.3000
     0.5000 0.7000 0.9000 1.0000 1.2000 1.5000 2.0000 3.0000
DF54   1.7    2.03   2.31   2.98   3.36   3.86   4.17   4.40   4.59
```

```
      4.68   4.72   4.73   4.72   4.67   4.60   4.58   4.61   4.86
      5.57   7.41   9.46   13.7   18.0   24.3   34.7   44.7   63.8
      99.1   131    160    174    193    219    254    301
FMESH64:P origin=-308 -420 136.5 imesh=407 jmesh=480 kmesh=141.5
        iints=143 jints=180 kints=1 factor 1.08E9
DE64   0.010 0.015 0.020 0.030 0.040 0.050 0.060 0.070 0.080 0.100 0.150
      0.200 0.300 0.400 0.500 0.511 0.600 0.662 0.800 1.000 1.117 1.333
      1.500 2.000 3.000 4.000 5.000 6.000 6.129 8.000 10.00 15.00 20.00
DF64   .0337 .0664 .0986 0.158 0.199 0.226 0.248 0.273 0.297 0.355 0.528
      0.721 1.120 1.520 1.920 1.960 2.300 2.540 3.040 3.720 4.100 4.750
      5.240 6.550 8.840 10.80 12.70 14.40 14.60 17.60 20.60 27.70 34.40
```

c. **Activity calculation tallies**

```
C ----- Activation Calculation ------
FC104 Target Activation
F104:N (52<150<151) 152 T
FM104 (-3E11 401 102) (-3E11 401 103) (-3E11 401 107)
     (-3E11 402 102) (-3E11 402 103)
SD104 1 1 1
C SD104 35.226 33.4388  68.6648
FC114 Target Magnet Activation
F114:N 41 42 43 44 T
FM114 (-3E11 301 102) (-3E11 301 103) (-3E11 302 102)       $ Fe-54,58
     (-3E11 303 107) (-3E11 304 103)                $ Nd-142,143
     (-3E11 305 107) (-3E11 306 107)                $ Nd-144,146
SD114 1 1 1 1 1
FC124 Ion Source
F124:N 80
FM124 (-3E11 401 102) (-3E11 401 103) (-3E11 401 107)
     (-3E11 402 102) (-3E11 402 103)
SD124 1
C SD124 66.7696
FC134 Ion Source Magnet
F134:N 100 101 102 103 104 105 106 107 108 109 110 111 112 113 114 115 T
FM134 (-3E11 301 102) (-3E11 301 103) (-3E11 302 102)       $ Fe-54,58
     (-3E11 303 107) (-3E11 304 103)                $ Nd-142,143
     (-3E11 305 107) (-3E11 306 107)                $ Nd-144,146
SD134 1 1 1 1 1 1 1 1 1 1 1 1 1 1 1 1
FC144 Moly Plate
F144:N 220
FM144 (-3E11 901 102) (-3E11 901 107)              $ Mo-98
SD144 1
FC154 Quartz Plate
F154:N 11
FM154 (-3E11 911 102)                      $ Si-30
SD154 1
FC164 Air Activation
F164:N 90 91 T
FM164 (-3E11 601 102) (-3E11 601 103) (-3E11 602 102)
SD164 1 1 1
```